KTH

A Measurement of the Antiproton and Proton Fluxes in Cosmic Rays using the CAPRICE Experiment

Niclas Weber

KUNGL TEKNISKA HÖGSKOLAN
Stockholm 1997

A Measurement of the Antiproton and Proton Fluxes in Cosmic Rays using the CAPRICE Experiment

Niclas Weber

AKADEMISK AVHANDLING

som med tillstånd av Kungl Tekniska Högskolan framlägges till
offentlig granskning för vinnande av teknologie doktorsexamen
fredagen den 21 februari 1996, kl. 10^{15}
i föreläsningssalen, Manne Siegbahnhuset, KTH Frescati
Frescativägen 24, Stockholm

Avhandlingen försvaras på engelska

Kungl Tekniska Högskolan
Stockholm 1997

Niclas Weber: A measurement of the Antiproton and Proton Fluxes in Cosmic Rays using the CAPRICE Experiment

ABSTRACT

New data on the antiproton flux and the antiproton to proton ratio in the energy range 0.62 to 3.19 GeV and the proton flux in the energy range 0.15 to 100 GeV at the top of the atmosphere are presented.

The measurement was performed using the balloon-borne experiment CAPRICE, which was flown from Lynn Lake, Manitoba, Canada, on August 8-9, 1994. The data were collected over 18 hours at a mean residual atmosphere of 3.9 g/cm^2. The experiment used the NMSU-WiZard/CAPRICE balloon-borne magnet spectrometer equipped with a solid radiator Ring Imaging CHerenkov (RICH) detector; a time-of-flight system; a tracking system, consisting of drift chamber and multiwire proportional chambers; and a silicon-tungsten calorimeter. This was the first time a RICH was used together with an imaging calorimeter in a balloon experiment, and the combination allowed antiprotons to be clearly identified in the rigidity range 1.2 to 4 GV/c. The resulting antiproton flux, derived from nine observed antiprotons, is consistent with a purely secondary production of antiprotons during the propagation of cosmic rays in the Galaxy.

More than 365 000 protons were identified in the rigidity range 0.4 to 100 GV/c. The proton flux is obtained with negligible contamination below 4 GeV. Above this energy there is a small (~1%) contamination from deuterons. The clean observation of the proton flux around 1 GeV gives a precise measurement of the effect of the solar modulation. In the energy region (above 10 GeV) where the solar modulation is negligible, good agreement with previous measurements is found.

Descriptors: balloons, cosmic rays, antiprotons, protons, abundances

ISBN 91-7170-780-9

Tryck Högskoletryckeriet KTH 1997

Contents

Chapter 1

Introduction

By the time you finish reading this sentence you will have been hit by several cosmic ray particles. It does not matter if you sit outside in the sun or down in the subway; you are still hit (at a different rate). The majority of these particles are muons, created in collisions between cosmic ray protons and atmospheric nuclei.

1.1 The Discovery of Cosmic Rays

The muons are part of the natural background radiation which was discovered early this century. It was assumed to come from the ground with the intensity therefore decreasing at higher altitudes. It was a great surprise when Victor Hess in his historical balloon flight (Figure 1.1) of 1912 discovered that the intensity increased with the altitude [1]. Hess used an electroscope to measure the ionization as a function of altitude. He concluded that the increase could best be explained by a penetrating radiation incident on the atmosphere from above. It took some years before this conclusion was generally accepted.

In the tradition of Hess, many more balloon flights have been dedicated to cosmic ray measurements. Studies have been made of the energy spectra and composition. The dominant part (90%) of the cosmic radiation reaching the Earth comprises of protons. Of the remaining part, 4% is helium, 2% carbon and oxygen, and rest are heavier elements with a large fraction of iron (if the fluxes are given as particles per GeV per nucleon) [2]. The proportions of these components are relatively constant with energy. Their spectra are well described by an inverse power law in energy and the differential flux (dN/dE) is given by:

$$\frac{\mathrm{dN}}{\mathrm{dE}} \propto \mathrm{E}^{-(\gamma+1)} \tag{1.1}$$

where $\gamma+1$ is the spectral index. The spectra span over many decades in energy and continue up to $E \sim 10^6$ GeV with $\gamma \approx 1.7$. The general shape of the spectra is given by the basic acceleration mechanism, derived by Fermi in 1949 [3].

NO FILE: [.THEORY]HESS.EPS

Figure 1.1: *Victor Hess preparing for his pioneering experiment leading to the discovery of cosmic rays. This photograph is taken 1912 in Aussig close to Prague.*

The relative abundances of elements in cosmic rays are similar to what is found in the solar system. One important difference is that two groups of elements (Li, Be, B and Sc, Ti, V, Cr, Mn) are many orders of magnitude more abundant in the cosmic radiation than in the solar system. These elements are almost absent as end products of stellar nucleosynthesis. Their presence in the cosmic rays is explained by spallation processes in the interstellar medium. The elements in the first group are produced by the abundant carbon and oxygen nuclei and the second group is produced by iron. Various cosmic ray propagation models were suggested in order to explain the observations of light nuclei. Given the cross sections for spallation and the measured abundances it is possible to calculate how much matter cosmic rays traverse between production and observation.

1.2 Antiprotons in Cosmic Rays

Observations of antiprotons ($\overline{\mathrm{p}}$) are important in studies of the production and propagation of cosmic rays in the galaxy. Antiprotons provide complementary information for tests of propagation models when compared to light nuclei. Although both antiprotons and light nuclei are generated by collisions of cosmic ray particles with interstellar matter, the production mechanisms are different. For example, due to kinematic constrains the production of antiprotons has a distinct threshold, while this is not the case in the spallation processes. Moreover, the antiprotons reflect the propagation history of the dominant proton component of the cosmic radiation. The light nuclei, on the other hand, depend on the heavier nuclei which might propagate by different means.

Antiprotons are also interesting from the standpoint of cosmology and elementary particle physics. Evidence of a primary (not produced in a p-p interaction in the interstellar matter) antiproton component from an extragalactic source would provide the first evidence for large quantities of antimatter in the Universe. Futhermore, a primary antiproton component could also arise from annihilation of dark matter [4] or evaporation of primordial black holes [5].

1.2.1 Discovery and Early Measurements

The existence of antiprotons in cosmic rays was speculated upon soon after the discovery of the $\overline{\mathrm{p}}$ in the laboratory [6] in 1955. The first estimation of the amount of antiprotons resulted in a $\overline{\mathrm{p}}/\mathrm{p}$ ratio

$\leq 0.2\%$ [7]. Later, when more accurate measurements of cross sections for antiproton production were avaliable from accelerators, the estimated $\overline{\mathrm{p}}/\mathrm{p}$ ratio became about an order of magnitude lower than the early estimations. Many attempts were made to search for antiprotons in the cosmic radiation using passive detectors, like nuclear emulsions, and active detectors, like magnet spectrometers.

It was not until 1979 that Golden et al. [8] reported the first successful measurements of 28 $\overline{\mathrm{p}}$ cosmic ray antiprotons. The measurement was done with a superconducting magnet spectrometer in the energy range 5 to 12 GeV. In the same year, Bogomolov et al. [9] also detected (2) antiprotons in the cosmic radiation. This measurement was done with a permanent magnet covering a lower energy range, 2 to 6 GeV. The observed fluxes pointed towards an excess of antiprotons. The antiproton to proton ratio was three times higher than expected, assuming that all antiprotons were produced as secondaries from p-p collisions. The estimation was based on the "leaky box model" [10] which successfully explained the flux of secondary nuclei, e.g. the boron to carbon ratio (see section 1.2.5). In an attempt to enhance the production of antiprotons, other propagation models were revised, e.g. the "nested leaky box model" [11] and the "closed galaxy model" [12]. Protheroe [13] calculated the expected $\overline{\mathrm{p}}/\mathrm{p}$ ratio in the closed galaxy model and was able to fit the observations better than with the leaky box model. However, the closed galaxy model could not explain the observed energy dependence of the ratio of secondary to primary nuclei in the cosmic rays. To overcome the shortcomings of the closed galaxy model, modifications were suggested, see for example [14].

Two years later (in 1981) Buffington et al. [15] measured a large flux of antiprotons with energies of a few hundred MeV. The antiprotons (14 $\overline{\mathrm{p}}$ reported) were identified from the topology of the annihilation products and not with a magnet spectrometer. The derived antiproton to proton ratio was so large that is was impossible to explain with any secondary production model and triggered a large number of theoretical speculations. In an attempt to clear up the picture, two more balloon-borne experiments (PBAR [16] and LEAP [17]) were deployed to measure the antiproton flux in the same energy range as the Buffington experiment, but both experiments failed to detect any antiprotons.

The experimental situation in 1990 is summarized in figure 1.2. The results are expressed as the antiproton to proton ratio. Dealing with ratios simplifies comparison between different flights. For energies greater than 3 GeV, the antiproton to proton ratio is rather insensitive to solar activity[1]. At lower energies, below 3 GeV, the ratio is much more uncertain due to variations in solar activity and

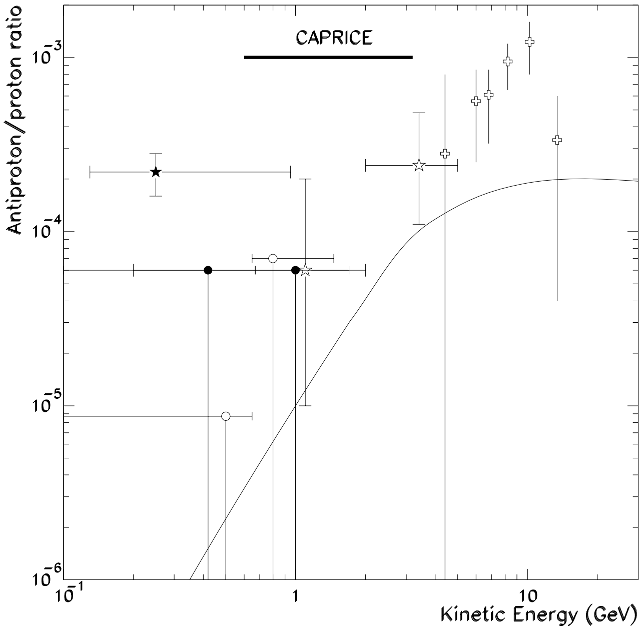

Figure 1.2: *The experimental situation in 1990. The measurements of the antiproton to proton ratio are: Golden et al. (open crosses) [18], Bogomolov (open stars) [19], Buffington (filled star) [15]. The upper limits are: PBAR (filled circles) [16] and LEAP (open circles) [17]. The solid line is a prediction of the expected antiproton to proton ratio from a pure secondary production model [20]. Note that the observed ratios are significantly higher than the prediction.*

---

[1] Cosmic rays entering the solar system are affected by the activity of the Sun (solar modulation), see section 11.2 for details.

uncertainties in the interstellar proton spectrum [21].

For certain type of predictions, it is essential to know the antiproton flux rather than the antiproton to proton ratio. To determine the flux correctly requires a good understanding of the detectors and the selection criteria and good understanding of systematic errors. The importance of the flux measurement is discussed in [22].

1.2.2 Sources of Primary Antiprotons

Possible sources of primary antiprotons are black holes or annihilation of super symmetric (SUSY) particles. Contributions from these sources, what existing observations and future experiments can provide, are discussed in [22].

Primordial black holes (PBHs) may exist as a result of initial density fluctuations, phase transitions or collapse of cosmic strings in the early Universe. The idea that black holes emit particles and therefore evaporate due to quantum effects was first suggested by Hawking [23]. Only black holes with a small mass (e.g. PBHs) can produce an observational flux of antiprotons. In [22], Mitsui et al. calculate the $\overline{\mathrm{p}}$ flux with the assumption that the PBHs are distributed proportionally to halo dark mass distribution. They show that only primordial black holes within a few kpc ($\sim$ a few thousand light years) of the solar system can contribute to the local interstellar antiproton flux.

Dark matter is thought to fill up the halo surrounding our Galaxy. One possible candidate for dark matter is the lightest supersymmetric particle, the neutralino. Mitsui et al. [22] use the minimal $N = 1$ supergravity model to calculate the possible source spectrum of antiprotons from neutralino annihilation. The resulting flux is of the same order as that from primordial black holes.

The flux of primary antiprotons would show a large enhancement below a few GeV during periods of low solar activity. Present experiments have not been sensitive enough to detect antiprotons coming from these primary sources. However, further observations during solar minima will be able to detect primary antiprotons if the estimations of Mitsui et al. [22] are correct.

1.2.3 Secondary Antiproton Production

The kinematics and shape of the primary proton spectrum defines the basic structure of the antiproton production curve. When antiprotons are produced in p-p interactions, there is a threshold for the production. The lowest energy a proton must have to produce an antiproton in a $p+p \rightarrow p+\overline{p}+p+p$ interaction is $6m_pc^2 \simeq 6$ GeV. At this energy the $\overline{p}$-p pair is produced at rest in the centre-of-mass system. In the laboratory system, the pair has a kinetic energy of about 1 GeV. To produce more energetic antiprotons, the incident protons must have an energy larger than 6 GeV. An antiproton can emerge forward or backward relative to the interaction point leading either to a higher or lower energy than 1 GeV. However, phase-space considerations make the production of low-energy (<1 GeV) antiprotons unlikely. Kinematics also dictate that only protons with energy greater than 10 GeV are important for the $\overline{p}$ production.

1.2.4 Interstellar Proton Spectrum

The flux of secondary antiprotons depends directly on the interstellar proton spectrum. Any uncertainty in the normalization and shape of the proton spectrum thus leads to a corresponding uncertainty in the calculated antiproton spectrum.

The spectral index of the proton spectrum is known with a high degree of accuracy. Combining proton spectrum measurements from a number of different experiments, Gaisser and Schaefer [24] find that the spectral index is in the range 2.65-2.75. However, they show that an error of ± 0.05 is significant and leads to a 20% spread in the antiproton flux at energies between 5 and 15 GeV. There is also a large disagreement in the reported absolute flux values, the spread is of the order ± 25%.

1.2.5 Propagation of Antiprotons in the Galaxy

The most complete descriptions of cosmic ray propagation in the galaxy are given by diffusion models. In a propagation model proposed by Ginzburg et al. [25], it is considered that cosmic-ray sources are distributed uniformly in the galactic disk and the escape of cosmic rays into the halo and finally into the intergalactic space is determined by diffusion. The validity of this model is supported both from radio astronomy observations and from theoretical concepts [26].

The problem with such a general model is the difficulty to make any testable predictions for cosmic-ray observations. Therefore, simplified models are more often used to calculate the expected ratio of various cosmic-ray species. One of these simplified models is the leaky box model [10]. In this model, the galaxy is in a steady state situation, uniformly filled with particles. The particles are trapped within the galaxy and the particles cross the galaxy many times before leaking out.

The main parameter of the leaky box model is the path length, i.e. how far the cosmic rays travel before escaping (λ_{esc}). This is normally expressed as the mean amount of matter the particles traverse during their lifetime. The path length is found by fitting the observed ratios of secondary to primary nuclei, for example the boron to carbon ratio. Most estimations agree that λ_{esc} has a peak around 4 GV/c and falls off for both higher and lower rigidities[2]. The value of λ_{esc} at the peak varies from 7-13 g/cm^2. The high-energy part of the B/C ratio is best fitted if λ_{esc} is described with a power law in rigidity. The exact shape of this parameter has been under discussion for a long time and various authors has come up with different shapes, see for example [26].

1.3 The CAPRICE Experiment

One of the experiment designed to clarify the experimental situation in 1990 was CAPRICE (Cosmic Antiproton Ring Imaging Cherenkov Experiment). The CAPRICE experiment is part of the WiZard [27] collaboration programme. WiZard is a collaboration between New Mexico State University (USA), Goddard Space Flight Centre (USA), INFN (Italy), University of Siegen (Germany), CRN Strasbourg (France) and KTH Stockholm (Sweden). WiZard was formed to bring together the experience of cosmic ray research conducted with balloons of the US groups, with the knowledge of particle

---

[2] Rigidity (R) = momentum/charge

detectors of the European groups. Together, the collaboration has been able to build the most advance detector systems ever used for cosmic ray research.

The WiZard collaboration conducted several balloon flights before CAPRICE. The first flight in 1989 (MASS89) was to repeat the 1979 measurement with the addition of an imaging calorimeter. The goal of MASS89 was also to perform detailed studies of electrons and positrons in the cosmic radiation. For the subsequent flight (MASS91), the tracking system was up-graded with two drift chambers. The goal of MASS91 was similar to MASS89 and several antiprotons were observed. For the flight in 1993, the focus was instead on positrons and particle identification was possible with a combination of a transition radiation detector (TRD) and a silicon-tungsten calorimeter. For CAPRICE, the TRD was replaced with a solid radiator RICH detector and the calorimeter was up-graded. The RICH detector was designed and build by the groups from KTH and Strasbourg.

The goal of CAPRICE is to make a detailed study of antiprotons in the cosmic radiation. Together with the calorimeter, the RICH detector is able to clearly separate antiprotons from the background of pions, muons and electrons between 0.6 and 3.2 GV/c. This region is indicated in figure 1.2. Positrons and light isotopes in the cosmic radiation have also been studied. However, this thesis focuses on antiprotons and protons.

1.4 Outline of the Thesis

Chapter 2 describes the detectors used in the experiment followed by a detailed chapter about the RICH. In chapter 4 the balloon flight is described. Chapter 5 to 8 deals with how information is extracted from the various detectors. The analysis of data from the flight is presented in chapter 9 to 12. First the selection of antiprotons is described in detail, then how the selection efficiencies are derived. When the efficiencies are known, the antiprotons flux is calculated and the antiproton to proton ratio is presented. Finally, in the last chapter, the proton flux is given.

1.5 The Author's Contribution

When I first joined the project as a diploma student in 1991, the construction of the RICH detector was well underway. The principle of the design was clear from the prototype studies made by Tom Francke and Martin Suffert [28]. My task as diploma student was to write the software for the data acquisition (DAQ) system used for the tests of the RICH detector. Later when I started my PhD on CAPRICE, I spent the first 1.5 years at CERN (1992-1993). At CERN I was involved in the tests of the RICH detector. It is worth pointing out that all work with the RICH detector was done by, in principle, only three people (Tom, Martin and myself). Therefore I got the experience of working with all the different parts of the RICH. My main responsibility was the DAQ program and the heating system. I designed and built the electronic module that controlled the temperature of the RICH. In total we took data in particle test beams for more than 50 days and the shifts were shared solely by the three of us. After the tests I took part in analyzing the data and the results are published in [29]. When the tests were finished at CERN, the RICH was transported to Las Cruces, New Mexico, USA, for integration into the payload. For long periods I was responsible for all activities with the RICH. Next step in the project was to prepare for the flight. The preparations took place at the launch site in Lynn Lake, Manitoba, Canada. As things turned out, I became responsible for the operation of the RICH during the flight.

After the flight, I have been involved in the analysis of the data. A lot of effort has been spent on the development of software for the RICH. For myself this has led to a deeper understanding of the RICH detector but also to better knowledge of all the detectors in the experiment. For example, I wrote the analysis program for the time-of-flight system. This work has resulted in a number of publications. The performance of the RICH detector during the flight is described in [30] and [31]. The first physics results, concerning electrons and positrons, are presented in [32]. However, the analysis work presented in this thesis concerns antiprotons and protons and is done by myself. It should be made clear that I would not have been able to reach these results without help from a number of people who are thanked in the acknowledgements.

Chapter 2

The CAPRICE Instrument

The CAPRICE balloon-borne instrument is equipped with a superconducting magnet and a tracking system, consisting of both drift chambers (DC) and multiwire proportional chambers (MWPC). Particle identification is possible with a time-of-flight (ToF) system, a Ring Imaging CHerenkov (RICH) detector and a silicon-tungsten imaging calorimeter.

2.1 The Gondola

The detector system (the payload) is mounted on a strong baseplate and kept inside an aluminium pressure vessel. The payload together with the associated support structure is hereafter called the gondola, shown in Figure 2.1.

The gondola is 4 m high, has a diameter of 1.5 m and weights approximately 2.1 tonne. Since air temperature at float altitude is approximately -20°C, the gondola must be thermally insulated. The thickness of the insulation is designed to balance the heat generated by the electronics in the payload and the irradiation from the Sun and the Earth, with the outside temperature. The insulation is painted white to reflect sun light. Power during the flight is supplied by lithium batteries mounted on the outside of the gondola. The power to weight ratio of the batteries is approximately 0.2 kWh/kg [33]. Hence, a 24 hour long flight with an average power consumption of 1.5 kW requires 180 kg of batteries. When the flight is terminated,

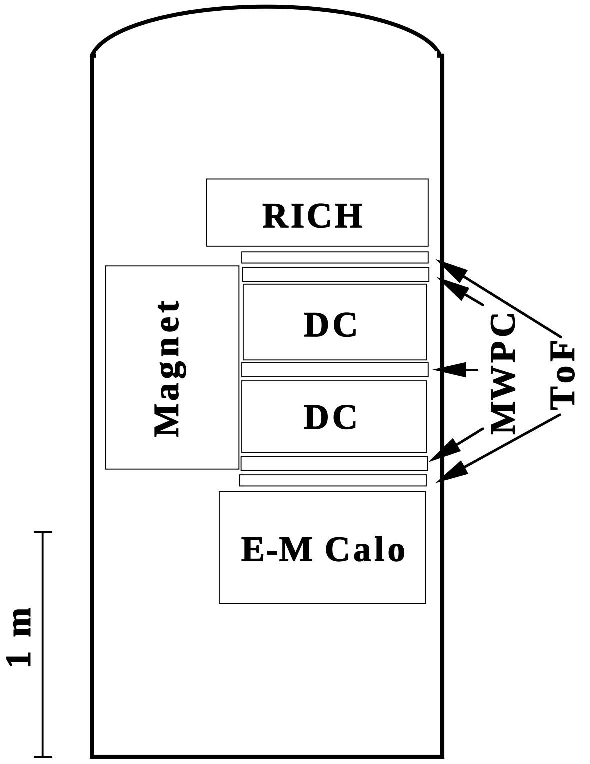

Figure 2.1: *A schematic view of the CAPRICE gondola.*

the gondola is detached from the balloon and lands with a parachute. To reduce the impact (a 5 g force) upon landing, a crash pad is mounted underneath the gondola. However, the largest force on the detectors is 10 g when the parachute opens and resistance to this force defines the design criteria for all detectors.

2.2 The Magnet

The superconducting magnet [34] comprises of a single coil of 11 161 turns of copper-clad NbTi wire. The outer diameter of the coil is 61 cm, the inner diameter is 36 cm and the axial thickness is 7.6 cm. The operating current is 120 A, producing a field of 4 T in the centre of the coil. The coil is placed in a dewar filled with liquid helium. The magnet is charged up before the flight and stays superconducting as long as the helium remains. The weight of the magnet is around 300 kg including the dewar and cryogenic equipment.

Figure 2.2 shows the magnetic field strength in the tracking volume. The position of the two drift chambers is indicated. The highest field in the drift chambers is 2.1 T dropping to 0.1 T further away from the magnet.

NO FILE: [.PAYLOAD]xxx.EPS

Figure 2.2: *The magnetic field strength in the tracking volume. The two boxes indicate the position of the drift chambers.*

2.3 The Tracking System

The tracking system is used to determine the rigidity and sign of charge of particles from their deflection in a magnetic field. The tracking system of CAPRICE consists of a combination of drift chambers [35] and multiwire proportional chambers [36]. Together they provide 19 measurements of the position of the particle in the bending (x) view and 12 measurements in the non-bending view (y).

2.3.1 The drift chambers

The drift chambers form the main part of the tracking system since they have better position resolution than the multiwire proportional chambers. The drift chamber boxes are made from 1 cm thick epoxy-composite plates with inner gas volumes of 47×47×35 cm^3. Each chamber contains six layers for x coordinate measurement and four layers for y. In each layer there are sixteen drift cells, as shown in Figure 2.3 a. A sense wire is runs axially through the centre of each drift cells and is surrounded by a hexagonal array of potential and cathode wires. The hexagonal cell structure, as shown in Figure 2.3 b, allows some wires to be shared between the cells in the same layer. The drift chambers are operated with CO_2 gas and during normal conditions the sense wires are kept at +4600 V, the cathode wires at +500 V and the potential wires are grounded. With this arrangement the electric field is uniform over most of the cell volume. The reason to operate the chamber with CO_2 is to have a low drift velocity of the ionization electrons so that the Lorentz forces in the magnetic field remain small. An additional advantage with CO_2 is that it is a non-flammable gas.

NO FILE: [.PAYLOAD]xxx.EPS

Figure 2.3: *Figure a) shows the box of the drift chambers. The drift cells are arranged in double layers which are shifted by half a cell to solve the left-right ambiguity. In figure b), a closer view of the cell structure is shown with the dimensions given in mm.*

A charged particle traversing a drift cell will ionize the gas within the cell. The spacial position of a particle is reconstructed from the time it takes for the ionization electrons to drift to the sense wire. The time measurement is started by a trigger signal generated by the time-of-flight scintillators. The time measurement does not indicate on which side of the sense wire the particle passed, the so-called "left-right" ambiguity. This ambiguity is solved by off-setting adjacent layers of drift cells by half a cell diameter, as shown in Figure 2.3 b.

In total there are 320 sense wires, read out by a LeCroy 4290 TDC system [37]. The timing technique is based on leading-edge discrimination with a fixed threshold, using the LeCroy 2735 DC amplifier/discriminator. The total weight of the two drift chambers is 80 kg and the power consumption is about 250 W. During the flight a constant gas flow of 3-4 litre/hour is maintained through the chambers.

2.3.2 The multiwire proportional chambers

The second component of the tracking system is the multiwire proportional chambers. The location of the MWPCs is shown in Figure 2.1. The position resolution of the MWPCs is not as good as the drift chambers but they still provide useful information. The multiwire proportional chambers can be used as an essentially independent measurement of the track and they increase the lever arm of the spectrometer. There are seven chambers for the x coordinate and four for the y coordinate. The position measurement is done with delay-line readout.

The active area of the MWPCs is 50×50 cm^2. Both the anode and cathode planes have a wire pitch of 2 mm and the anode-cathode distance is 6 mm. The cathode wires are mounted perpendicular to the anode wires. The entrance windows to the chambers are made of mylar film and one of the windows is metalized and doubles as a cathode plane. The chambers are operated with "Magic Gas"[1] at a high voltage of 4.7 kV.

---

[1] 70 % Ar, 29.5 % Isobutane and 0.5 % Freon 13B1 (CCl_3F)

2.4 The Time-of-flight System

The primary function of the time-of-flight (ToF) system during the flight is to provide a trigger for the data acquisition system. A trigger is generated when a particle traverses the two scintillator planes within a limited time. When the trigger signal is received by the on-board computer, the readout cycle is started and information from all detectors is stored on tape.

The signals from the scintillators are also used in the analysis. The scintillators provide information about dE/dx losses, which allows particle identification, as well as timing information. The timing information is used to measure the velocity of the particles and to discriminate up-going (albedo) from down-going particles.

The time-of-flight system consists of two layers of plastic scintillators, one layer placed on top of the tracking system and one underneath it, as shown in Figure 2.1. Each layer is divided into two "paddles" with a size of 25×50 cm^2 and a thickness of 1 cm. The scintillators are viewed at each end by 5 cm diameter photomultiplier tubes (PMTs). The signal from each PMT is split in two parts, one part is connected to an analog-to-digital converter (ADC) and the other to a time-to-digital converter (TDC) via the trigger logic.

2.5 The Calorimeter

The silicon tungsten calorimeter [38] is an upgraded version of a the calorimeter that was flown in 1993 during the TS93 experiment [39]. The calorimeter is designed to distinguish between minimum ionizing particles, hadronic and electromagnetic showers. Weight and power consumption were the most severe constraints considered during the design and construction of the calorimeter: As a consequence, its depth is insufficient to fully contain high energy (>5 GeV) showers. However, its high granularity and energy resolution allow measurement of the shape and energy losses of the showers, as well as shower starting point and direction of the primary particles.

The calorimeter is composed of eight 48×48 cm^2 silicon planes. Each silicon plane is interleaved with a layer of tungsten converter, one radiation length (X_0) thick. A single plane consists of an array of

8×8 pair of silicon detectors mounted on a G10 motherboard. Each detector has a total area of 60×60 mm^2 and is divided in 16 strips, 3.6 mm wide. The detectors are mounted back-to-back with perpendicular strips to give x and y readout. The strips of each detector are daisy-chained longitudinally to form one single strip 48 cm long. Taking into account all the material, the calorimeter has a total of 7.2 X_0 and 0.33 nuclear interaction lengths.

To reduce thermal noise the silicon detectors are kept below 30° C. The cooling system is based on evaporation of water from a cooling box placed in thermal contact with the bottom of the calorimeter. A CAMAC crate contains all the readout modules and two lithium battery power supply modules which provide the depletion voltage to the silicon planes. The voltage can vary from 60 to 110 V according to the different kind and thickness of the silicon detectors employed. For the calorimeter three different types of detectors are used.[2] Each plane is made from silicon detectors of same thickness and same manufacturer.

The front-end electronics is based on units consisting of 16 channel modules providing analog circuitry for the charge amplification and sample-and-hold for each channel. A post-amplifier is provided for each channel so that the signal may be read at two different amplification (×1 and ×16). Consequently, a plane has 256 channels (64 strips × two amplifications × two views), read out multiplexed by a CAMAC module. All together, the eight planes have 2048 channels.

In the CAMAC modules, the analog signals from the amplifiers are digitized by an 8-bit ADC. Zero suppression is achieved by comparing the digital value with a hardware threshold before storage. For each strip the threshold is defined during a preflight calibration run that samples the pedestal of all strips. The digitized data are combined with the strip address and formatted into a 16-bit word ready for readout by the on-board computer.

---

[2] Hamamatsu, 400 μm thick; Camberra, 380 μm thick and SGS 300 μm thick

2.6 The On-board Computer

The payload is equipped with a data acquisition system to control the operation of all detectors and communication with the ground. The system is based on a VAX 3200 CPU running VAX ELN, hosted in a DEC Q-bus back plane. The detectors are read out with Q-bus to CAMAC interface. Data are stored on-board on two 4 mm tape drives or on hard disk. Both the hard disk and tapes are recovered after the flight. A portion of the data is sent to the ground to monitor the performance of the detectors and the condition of the payload, this is discussed in Chapter 4. It is also possible to send up commands to the payload from the ground; to adjust the high voltage of a detector, for example.

Chapter 3

The RICH detector

In CAPRICE the RICH detector is used to identify particles through the direct measurement of the Cherenkov angle. This chapter starts with a short description of the history and theory of the Cherenkov effect and the concepts of Cherenkov detectors. The main part is about the RICH detector, including a description of both the mechanical and electrical features.

3.1 The Cherenkov Effect

The earliest reports of the Cherenkov effect date back to 1910 when Marie Curie found that bottles of concentrated radium solution glowed with a pale blue light. The phenomenon was not investigated in a systematic manner until 1934 when the Russian physicist P. A. Cherenkov (for a list of references, see [28]) found that samples of pure water gave simular bluish light when irradiated by gamma rays. The presence of luminescence from water was difficult to explain with any existing theory because water was not expected to fluoresce. S. I. Vavilov, Cherenkov's supervisor, suggested that this unknown effect did not originate from the gamma rays but was instead caused by Compton electrons. This was later confirmed by Cherenkov when he showed that the same effect arose when his sample was irradiated by fast electrons. In further studies, Cherenkov proved that the emitted light could not be due to fluorescence. The emission was not affected by heating or by substances which normally would have quenched the fluorescence. The studies also showed that the emission was not isotropic and that the light was emitted in a certain direction.

The theoretical explanation of the phenomenon was presented a few years later by the Russian theoreticians I. M. Frank and I. J. Tamm [40]. With their theory they also predicted at that time unknown properties such as the absolute intensity, the spectral distribution and the angle of emission, all of which Cherenkov later verified experimentally.

For a full description of the theory, see [28], what follows is a conceptual discussion. The first thing to be considered is that a particle can travel faster than the speed of light. This is not in contradiction of Einstein's special theory of relativity, which states that a particle cannot travel faster than the speed of light *in vacuum.* In a medium with index of refraction, n, the speed of light is, $v = c/n$, and hence the speed of the particle can be larger than v.

The second thing to consider is what happens when a charged particle traverses a dielectric medium. The particle polarizes the atoms in the medium along the track of the particle. The polarized atoms soon return to the ground state by emitting electromagnetic radiation. When the particle velocity is small, the polarization is symmetric around all points along the track and no net effect is observed. If however the particle velocity is large, then the polarization is no longer symmetric and the emitted radiation is coherent, due to constructive interference. This can be understood from the Huygen construction presented in Figure 3.1. In the figure, it is shown that radiation is only observed at a particular angle (θ) with respect to the direction of the particle. This is the angle at which the wavelets from arbitrary points on the track are coherent and combine to form a plane wave front. This coherence takes place when the particle traverses AB in the same time that the light travels from A to C. If the velocity of the particle is βc, where c is the speed of light in vacuum, in a time τ the particle will travel a distance AB=$\beta c\tau$, and the light a distance AC=$\tau c/n$, where n is the refractive index of the medium. This leads to the following relation:

$$cos\,\theta \;=\; \frac{1}{\beta n}\,, \tag{3.1}$$

known as the "Cherenkov relation".

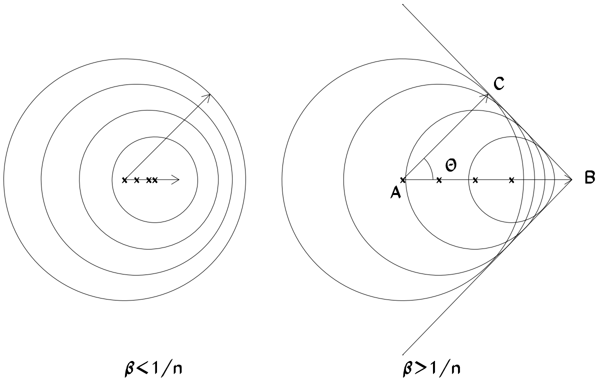

Figure 3.1: *A Huygen construction to illustrate the coherence of wavelets forming a plane wave when the β of a particle is larger than c/n.*

Furthermore:

1. For a medium of given index of refraction, n, there is a threshold velocity, below which no Cherenkov radiation is emitted. The threshold velocity is $\beta_{min} = 1/n$.
2. There is a maximum angle of emission for $\beta \sim 1$ particles, given by θ_{max}=arccos(1/n).
3. The radiation occurs mainly in the visible and near-visible (UV) part of the spectrum, as long as $n > 1$.

Figure 3.1 is drawn only in two dimensions. There is of course a symmetry around the velocity vector of the particle. The light emitted from each point along the track propagates along the surface of a cone, and the semi-top angle is the Cherenkov angle. This is shown in Figure 3.2.

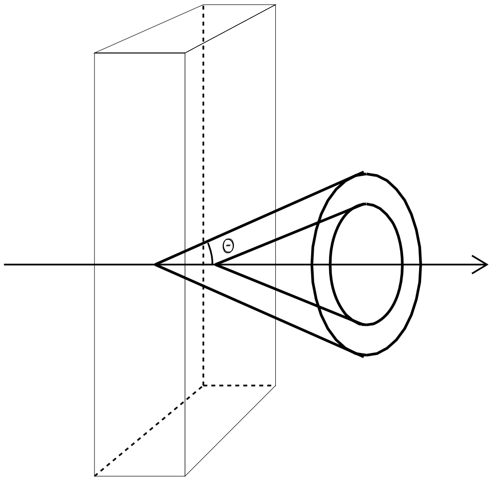

Figure 3.2: *The cone of Cherenkov light emitted along the track of the particle.*

3.2 Cherenkov Counters

The Cherenkov effect was originally observed by the bare eye or photographic emulsions. Electronic devices sensitive enough to detect the the weak and fast light-pulses from Cherenkov radiation did not exist. The development in the 1940s of the photomultiplier tube lead to a rapid development of new particle detectors and among them were Cherenkov counters.

One of the most famous application of the early Cherenkov detectors is in the discovery of the antiproton in 1955 by Chamberlain et al. [6]. A Cherenkov counter was also used for the discovery of antiprotons in the cosmic rays in 1979 by Golden et al. [8]. Cherenkov counters have since been used in other balloon-borne experiments, e.g the IMAX [41] experiment was equipped with an aerogel Cherenkov detector.

It was not until 1979 when the first Cherenkov counter was designed that could detect the ring of the Cherenkov light [42]. These kind of detectors soon became known by the acronym RICH, from Ring Imaging CHerenkov detectors. After this breakthrough, a rapid development took place and soon after the first RICH counter was used in a particle physics experiment. Subsequently, RICH detectors have been used with great success in, for example, the Delphi detector [43] at CERN.

The next step was to adopt the RICH technique for an astroparticle physics experiment. In 1991 the University of Chicago launched a RICH counter in a balloon-borne experiment, with the aim of measuring the flux of isotopes with $Z \geq 2$ [44]. However, it was not until the CAPRICE experiment that a balloon-borne RICH detector was able to identify charge one particles in the cosmic rays.

3.3 Principle of the CAPRICE RICH

The CAPRICE RICH [29] detector is designed to identify antiprotons in cosmic rays amongst a large background of electrons, muons and pions. Separation is possible in the rigidity range 1-4 GV/c for incidence angles between 0 and 20°.

In Figure 3.3 a schematic view of the detector is shown. The figure illustrates how Cherenkov light is emitted in the sodium fluoride (NaF) radiator when a charged particle traverses the detector. The Cherenkov light refracts out of the crystal and the cone of light expands in the nitrogen filled drift volume before it enters the photosensitive part of the detector through a quartz window. In the photosensitive volume, the Cherenkov photons are converted into photoelectrons through photoelectric effect in the organic compound tetrakis (dimeylamino)-ethylene, also known as TMAE. The

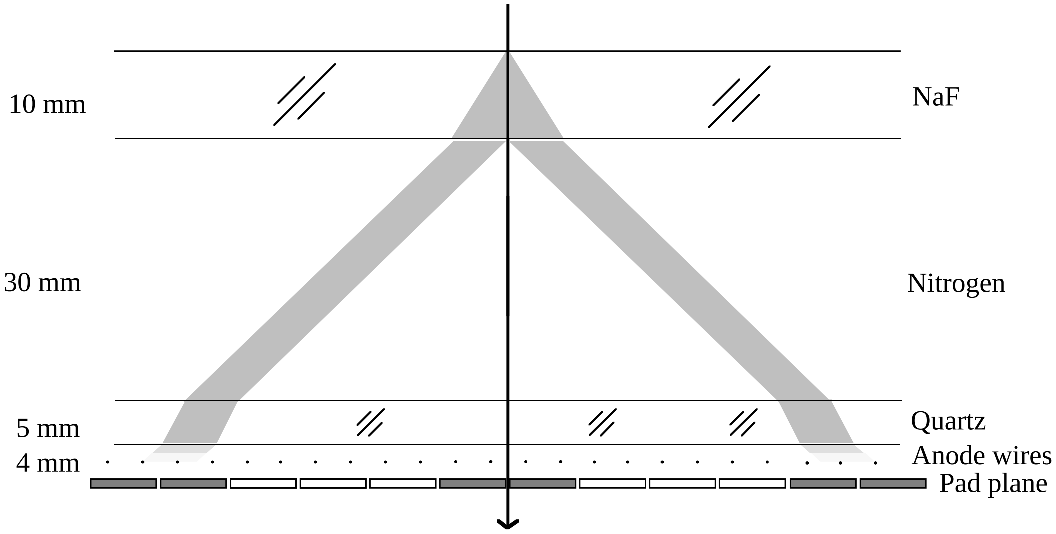

Figure 3.3: *A schematic view of the NaF-RICH detector.*

photoelectrons are attracted towards the anode wires of the multiwire proportional chamber (MWPC) by an electrostatic field. The photoelectrons are amplified by the anode wires and induce pulses on the wires as well as on the cathode planes. The lower cathode plane is divided into small squares, called pads, and the signals in both the pads and the anode wires are detected. In this way a two-dimensional image of the Cherenkov light is recorded in the pad plane, and anode wires give a projection of the same image. This enables the Cherenkov angle to be estimated on an event by event basis. The RICH detector is placed in a box made of a strong frame of aluminium, covered with two carbon fibre covers, which minimizes the amount of material along the trajectory of the particle. This is important to reduce the interactions of the antiprotons which traverses the detector. All material along the trajectory is listed in Table 11.4. The outside of the box is covered with thermal insulation.

The total weight of the RICH detector is 20 kg (80 kg including the pressure vessel and the gas system). The RICH consumes 60 W of power for readout electronics, 15 W for the fans and, 0-250 W for heating, depending on the outside temperature.

In the following sections, the different parts of the RICH are described in more detail. The analysis of the flight data and the algorithm for the calculation of the Cherenkov angle are described in Chapter 8.

3.3.1 The radiator

A solid radiator is chosen because of its compactness and simplicity: A liquid radiator (e.g. a flourocarbone) needs to be contained in a UV-transparent container which would emit Cherenkov light itself and thereby complicate the measurement. It would also be difficult to make the container strong enough to withstand the forces during take off and landing. The problem with a solid radiator is that if the index of refraction is too high, the Cherenkov light is trapped inside the radiator due to total internal reflection. Following Snell's law of refraction, the Cherenkov light from a $\beta = 1$ particle, at normal incidence angle, can only refract out if the index of refraction is less than $\sqrt{2}$.

The only known solid with a index of refraction of less than $\sqrt{2}$, in the wavelength interval where the RICH is sensitive (170-220 nm), is sodium fluoride (NaF). At a wavelength of 185 nm the refractive index is 1.39 [45], giving a threshold velocity for Cherenkov light of β=0.72. The index of refraction of NaF (n_{NaF}) has a strong dependence on wavelength and this affects the performance of the detector. The variation of n_{NaF} and how to compensate for it is described in more detail in Chapter 8.

The radiator consists of 36 crystals, each $84 \times 84 \times 10$ mm^3, optically connected together forming a 6×6 matrix. The optical contact between the crystals is maintained by a thin (50 μm) layer of grease applied to the sides of the crystals. The crystals are then mounted in a frame and pressed together from the sides. In addition, a piece (1.5 mm) of each corner is cut off to allow a fixation with a screw and the crystals hang in these screws from a carbon fibre plate.

3.3.2 The drift volume

The drift volume is the space between the NaF crystals and the quartz window. In the drift volume, the cone of light is expanding into ring. The thickness of the drift volume is chosen to be 30 mm to ensure a good separation between the Cherenkov light image and the ionization signal of the particle. This is especially important for particles with a large inclination. A larger thickness would give a too large ring radii and the Cherenkov light would not be contained inside the pad plane for particles with high β and small incidence angles.

The drift volume is filled with pure nitrogen gas to avoid absorption of the Cherenkov photons. A small constant flow (2 litre/hour) was maintained during the flight. The optical transmission coefficient of nitrogen in this wavelength region is higher than 99 %.

3.3.3 The quartz window

The drift volume is separated from the photosensitive chamber by a 5 mm thick quartz window. Quartz is transparent to wavelengths longer than 170 nm and this determines the shortest wavelength of Cherenkov light can enter the photosensitive chamber. The window is made of a single plate, 480×480 mm^2, glued into a frame of Invar [46]. Invar is a metal alloy made of steal and nickel (36 %) with the same thermal expansion coefficient as quartz, which is important because the detector is heated during operation. The frame is able to slide sideways on an O-ring, thereby allowing for movements due to thermal expansion.

Metallic strips are evaporated onto the bottom side of the quartz window to act as an upper cathode plane of the MWPC. The strips are 150 μm wide, 3 mm apart and only 100 nm thick. With such thin strips, a better optical transmission of the light is achieved compared to e.g. a metallic mesh. This is especially important when the light enters the quartz window at large angles (toward the normal). The transmission of the quartz window is 99 % at 185 nm, for all angles.

3.3.4 The photosensitive chamber

The heart of the photosensitive chamber is a multiwire proportional chamber (MWPC). It has 128 wires of diameter of 15 μm, separated by 4 mm distance. The wires are 520 mm long, made of gold-plated tungsten, and oriented perpendicular to the cathode strips (the strips on the quartz window). The distance between the anode wires and each cathode plane is 2 mm.

The chamber is filled with a mixture of pure ethane and TMAE. The TMAE converts the Cherenkov photons into photoelectrons and the quantum efficiency of TMAE is 30 % for wavelengths shorter than 200 nm. The chamber is 4 mm thick but the typical distance a photon travels inside the chamber is 6 mm due to the large Cherenkov angle. To get a 6 mm absorption length [47] ($\sim$63 % absorption probability), the TMAE must be heated to 40 °C. A higher temperature would result in a shorter absorption length, but in a too high power consumption during the flight (when the power is taken from batteries).

When a photoelectron is produced, it is attracted to the closest anode wire. Close to the wire, the electron has gained enough speed to ionize the ethane and liberate more electrons. This causes an avalanche of secondary electrons and at the wire, more than 2×10^4 electrons are collected. The avalanche induces a pulse, on the wire itself but also on the cathode planes. This creates an image of the ring of Cherenkov light on the cathode planes and the signals are detected in the lower cathode plane, the pad plane.

3.3.5 The pad plane

The pad plane has a size of 512×512 mm^2 and the surface is plated with copper and gold. The upper side is divided into 4096 pads, each with a size of 8×8 mm^2. A smaller pad size would give a smaller position error. However, if the pad size is decreased, then the detected signal becomes smaller. Since the noise does not decrease, the signal to noise ratio will decrease. In addition, a smaller pad size will also increase the total number of electronic channels and a too high power consumption. Taking this into account, a pad size of 8×8 mm^2 is found to be optimum for the RICH. In each pad, a hole is drilled in which a pin is glued, connecting the surface of the pad to the backside of the pad plane. Special connectors are placed onto the pins, connecting the pads to the front-end electronics.

3.3.6 Gas and heating system

The TMAE is kept outside the RICH in a separate container through which the ethane gas bubbles before it enters the detector. At room temperature TMAE is a liquid and the vapor pressure is only 0.4 mbar, giving a too long absorption length. As pointed out above, the TMAE must be heated to give a higher absorption probability. During the flight, the TMAE was heated to 37 °C [1]. To prevent condensation of the TMAE in any other part of the gas system (in the worst case the MWPC), the rest of the RICH is heated to a higher temperature. The tubes connecting the TMAE container to the detector were kept at 51 °C and the MWPC had a temperature of 46 °C during the flight, see Figure 4.3.

The heating of the RICH is done by circulating the air inside the box. The circulation is provided by two fans and in front of the fans, two heating elements are mounted. The tubes are heated by heat foil wrapped around them and the TMAE is heated by a heat jacket placed around the container.

The temperature of the detector is regulated by a specially developed electronic module. The module has four channels for temperature regulation, 12 channels for temperature measurements and four channels for pressure measurement. The sensors are placed at a number of different places around the RICH and at the outside, e.g. in the TMAE container.

Temperature regulation is done individually in the four channels. One channel controls the temperature of the TMAE container, one controls the temperature of tubes connecting the TMAE container to the detector and two channels control the temperature of the air inside the detector. Each channel has a temperature sensor connected to the control circuit and the preferred temperature (the set point) is set by a potentiometer on the front panel of the module. The control circuit compares the temperature measured by the sensor with the

---

[1] A higher temperature would result in a too high power consumption.

preferred value. Based on this information, the heating is switched on or off. With this system, the temperature of the different parts is kept constant to within less than ±1.0 °C. However, if the outside temperature increases above the set point, the system can only switch the heating off and not actively cool the RICH. This was the case during the flight when the payload temperature increased by more than 20 °C, see Chapter 4 for more details.

In addition, an alarm function is implemented for the heating of the TMAE. The maximum allowed TMAE temperature is 90 % of the chamber temperature (in °C) to avoid condensation. If the chamber temperature becomes too low, the TMAE heating is turned off by the alarm until the chamber temperature has increased above this limit. During normal operation, the TMAE temperature is always at least 5 °C lower than the chamber temperature.

The same kind of temperature sensor (Analog Devices AD590 [48]) is used for both the control circuit and for the measurement. It is chosen because of simplicity, The AD590 sensor provides a linear current output of 1 μA/K and thereby allowing both the control circuit and the measurement circuit to be construct with a few components. Each channel of the control circuit is build around two standard operational amplifiers (LM324) [49], and for measurement, a monolithic amplifier from (AD524) [48] is used. This gives a simple but reliable system, well suited for operation in a balloon-borne experiment.

3.3.7 Readout electronics

The front-end electronics are based on the AMPLEX chip. The AMPLEX is a very low noise amplifier, developed at CERN [50]. It has 16 channels per chip and each channel includes a charge sensitive preamplifier, a shaping amplifier and a track and hold system where the charge is stored before being read out. For the pad readout, the AMPLEX chips are daisy-chained and read out in series (multiplexed), 32 at the time. In this way, all 4096 pad channels are read out with only eight multiplexed signals.

The multiplexed signals are fed to the CAMAC based module DRAMS [51]. In the DRAMS module, the signals are first digitized by an 8 bit flash ADC, then compared with a threshold. If the signal is above the threshold, the pedestal is subtracted and the remaining value is stored in memory together with an address referring to the channel number. Both the pedestals and thresholds are adjusted individually for each channel. The values of the pedestals and thresholds are determined during the calibration runs with the RICH [52]. Typically, the thresholds are set to 3 channels above the pedestals, corresponding to more than three times the r.m.s. value of the noise. The maximum number of channels in the DRAMS module is 512, so the address is specified with 9 bits. The stored values are later read out by the data acquisition system. A description of the data acquisition system used for all tests in particle beams is found in [52].

The DRAMS cards were modified for the balloon flight. During the beam tests of the detector, a change in the behaviour of the DRAMS correlated to temperature, was noticed. When the temperature changes, the reference voltage to the ADC drifts and, as a consequence, a larger number of channels appear to have a signal above the threshold. This did not cause any severe problems during beam tests since the DRAMS could be recalibrated. For the flight, the situation was different and preferably only one calibration should be done at the beginning of the flight. To overcome this problem, the drift of the reference voltage is compensated by adding a thermistor with the opposite temperature behaviour.

A second modification to the DRAMS for the flight was done on the number of bits used. Normally, all eight bits from the ADC are read out (giving 255 as the highest ADC signal). Together with the nine bits specifying the address, 17 bit words are read out from the DRAMS cards. However, for the operation in the gondola, the data is limited to 16 bit words by the telemetry system which sends data to the ground. Therefore, only the lower 7 bits of the ADC are read from the DRAMS. In order not to lose any information, the signal from the AMPLEX is attenuated to be less than 127 (corresponding to 7 bits).

Last modification of the DRAMS is to change the characteristic of the ADC. The response curve of the ADC is divided into two parts with different gains. The modification is done so that low signals (from Cherenkov photons) have a higher gain whereas high signals (induced by the traversing particle) have a lower gain. In

Figure 3.4 the output of the DRAMS is shown as function of the induced charge. Note the two slopes with different gains. Above 200 fC the the AMPLEX becomes saturated. How this effect is used in the analysis is discussed in section 8.1.

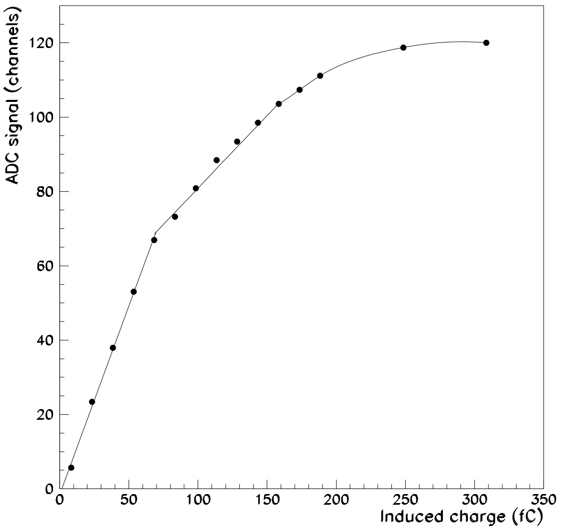

Figure 3.4: *The output signal of the DRAMS as a function of the charge injected into the AMPLEX. Note the two slopes with different gains and that above 200 fC, the AMPLEX becomes saturated.*

3.3.8 Tests in particle beams

The RICH detector has been extensively tested in particle beams at CERN (PS accelerator, Z=1) and at Saclay (Saturne, Z=1-8) for more than 50 days of beam. Measurements were done with different kind of particles, with beam momenta from 1 to 10 GeV/c, and at incidence angles from 0 to 30°. In addition, a number of detector parameters were varied, e.g. the high voltage of the anode wires and the temperature of the TMAE. From these tests, the optimal detector parameters were found. The results of the beam tests are given in [29].

Chapter 4

The CAPRICE Balloon Flight

The balloon lifting the gondola containing the CAPRICE apparatus took off early in the morning on August 8, 1994. The launch ended a 10 week period of preparations and waiting for good flight conditions at Lynn Lake. This chapter describes the 27 hour flight, including performance of the detectors.

4.1 Choice of Launch Site

The flight started at Lynn Lake in northern Manitoba, Canada. The main reason to fly from Lynn Lake is the low geomagnetic cut-off. It defines the lowest rigidity primary cosmic rays can have still penetrating the Earth's magnetic field. The cut-off shows a strong latitudinal dependence and has the strongest affect at the level of the magnetic equator where it is approximately 16 GV/c. In order to have a low cut-off the flight has to take place close to one of the magnetic poles. At Lynn Lake the cut-off is 0.3-0.4 GV/c. Note that the cut-off only affects primary cosmic rays, secondary particles produced in the atmosphere can have rigidities below the cut-off.

There are also practical reasons for launching balloons from Lynn Lake. The primary reason is the two large crossed runways which makes it possible to launch with ground winds coming from different directions.

Finally, balloon flights are preferably made in areas with low population density and in that respect northern Canada is a very good choice!

4.2 Preparations

The preparations for the flight started several months before the launch in Las Cruces, New Mexico, where the payload was assembled. During the preparations the payload was tested in many different ways. The first step of the assembly was to verify that each detector worked individually and that it was possible to control it with the on-board data acquisition system. Next step was to test the complete spectrometer and check the overall performance. The spectrometer was first tested with and without a magnetic field. The payload was also tested under conditions resembling the flight, e.g. large temperature variations. The performance at high temperature was tested by switching off all cooling of the payload, increasing the temperature to 35 °C. The low temperature test was done by cooling the gondola with dry ice and this test was terminated when the temperature fell below a few degrees centigrade.

Parts of the test schedule were repeated at Lynn Lake. Before the payload could be declared as flight ready, several long runs had to be made with the magnet charged and conditions as close as possible to a real flight situation. During these runs, detector performances and stability were checked. The data collected during these runs are also used in the final data analysis, for example to estimate the muon contamination in the RICH antiproton selection (section 9.5.5) and to calibrate the calorimeter (section 7.1.3). After these tests were completed successfully, the payload was ready for flight.

4.3 The Flight

The CAPRICE flight was part of NASA's scientific balloon program and the launch and payload control was overseen by the National Scientific Balloon Facility (NSBF). For several years the NSBF has successfully launched balloons from Lynn Lake. The flight distance is limited by the Rocky mountains and the planned landing place was Peace River in Alberta, a distance of 1100 km. The flight duration is given by the speed of the jet streams. During the summer season the jet streams blow in a westerly direction at Lynn Lake. The speed changes with the time of the year and slowly decreases during the summer, falling to zero at the end of August and then reversing its direction.

In order to fulfill the physics goal of the flight a minimum duration of 17 h was requested from the collaboration to the NSBF. The date of the launch is then determined by the speed of the jet streams. In 1994 the seasonal change was later than normal and the flight was delayed by several weeks.

To be able to lift the payload to the required height the NSBF used a balloon of volume 1.1×10^6 m^3. The main features of the balloon and flight are given in Table 4.1. Only 5 % of the total volume was filled with helium on the ground. During the ascent the

Flight data	
Mass	2.1 tons
Ballast	330 kg
Balloon volume	1.1×10^6 m^3
Maximum altitude	38.2 km
Minimum altitude	36.3 km
Duration	27 hours
Duration at float altitude	23 hours
Distance	1100 km
Latitude (start-stop)	56.9°-57.2° N
Longitude (start-stop)	101.1°-117.5° W
Average velocity	13 m/s
Trigger rate	400 Hz
Dead time per event	10 ms
Events collected	5.2×10^6
Average events length	420 bytes
Power consumption	1.5 kW

Table 4.1: *Important parameters of the flight and payload*

volume increases as the atmospheric pressure decreases.

The payload took off at 7.28 local time on the morning of August 8, 1994. It reached float altitude (36-38 km) after less than 4 hours (at 11.07 it reached 38.2 km). At float altitude it started to move in a westerly direction with a velocity of 10-18 m/s.

The position of the payload was monitored during the whole flight by the NSBF using the Global Positional System (GPS). The GPS instrument gave information on the altitude as well as of the latitudinal and longitudinal position. The GPS data was used both to track the payload and to predict possible landing places. In Figure 4.1 the flight altitude as a function of time is shown. The flight altitude dropped during the flight from 38.2 km to 36.3 km.

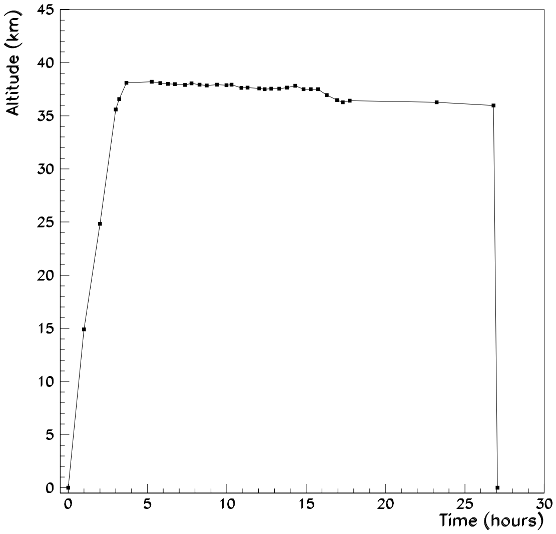

Figure 4.1: *The altitude of the payload during the flight. The values are given by the GPS instrument.*

As long as the payload was in range of the telemetry, commands could be sent directly to the payload and the payload could send data to the ground. When the payload after 18 hours flight got out of range, the control was taken over by a relay station at Ft.

Mc Murray, Saskatchewan. At this point, communication from the payload was limited to engineering data but commands could still be sent up to it.

Data taking was terminated and all detectors switched off the next morning at 8.00 when the payload was running out of battery power. Approximately one hour later the magnet was discharged and at 9.10 the payload was switched off. At this stage the NSBF had full control of the payload and landing preparations started. One hour later, the balloon was detached and the gondola landed by parachute at 11.15, 150 km north of Peace River.

4.4 Flight Performance

The performance of the payload was continuously monitored during the flight. This was done by analysing short data files collected several times per hour and by looking at engineering data sent from the payload to the ground. The short data files were sub-samples of the data written to the on-board storage media and contained all the information generated by the detectors. The engineering data contained the information gathered by more than 150 sensors distributed in the payload. With this data it was possible to monitor important parameters like temperature and pressure of the payload. The engineering data also contained information about, e.g., the number of words read out per event for each detector and the trigger rate. The number of words read per event was monitored on-line to immediately indicate any change in detector performance. An increase in the number of words could have indicated an increase in the detector noise whereas a decrease could have indicated lower efficiency. Other properties, like the gain of a detector were not possible to monitor with the engineering data. Instead the sample files were analysed giving a more detailed information of the detector performances.

4.4.1 Temperature and pressure of the payload

During flight the temperature of the payload varied as expected from day to night. The temperature and pressure of the payload during the flight is shown in Figure 4.2. The temperature shown in

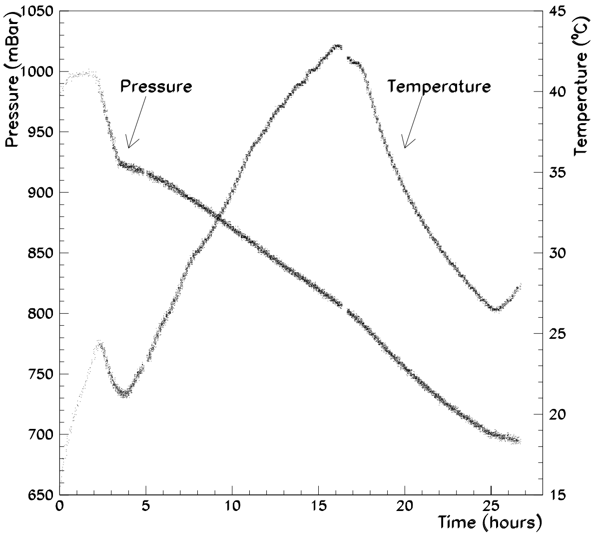

Figure 4.2: *The temperature and pressure of the payload during the flight. The gaps in the curves refer to short periods when the data taking was stopped.*

the figure is given by a sensor placed in the CAMAC crate containing the ADC and TDC for the time-of-flight scintillators. This sensor accurately reflects the general temperature trend during the flight and it is used for the temperature compensation of the time-of-flight system, see Chapter 6. At launch the payload had a temperature of 15 °C. During the ascent the payload was heated up by the power of the on-board equipment. The increase temporarily stopped at the flight altitude because the shadow-side of the payload the outside temperature was less than -20 °C, but started to increased again by the irradiation from the sun. When the sun set the temperature went down.

The pressure in Figure 4.2 is given by a sensor placed in the gas system of the RICH and shows the payload pressure. The pressure also changed significantly during the flight. A small increase was expected due to the gas flow through the detectors. The pressure increase was planned to be compensated for by a remote controlled valve to the outside. The sharp drop in the pressure after two hours occurred when the ventilation valve was opened. When the pressure had decreased to 920 mbar the valve was closed but the pressure continued to fall. This was caused by a leak in the gondola. After the flight, when the payload was dismounted, it was found that the leak was caused by a small crack in the tube connecting the helium dewar to the outside of the gondola (to let out the helium that boils off). The pressure continued falling with a constant rate and at the end of the flight it had decreased by 30 %.

4.4.2 The RICH

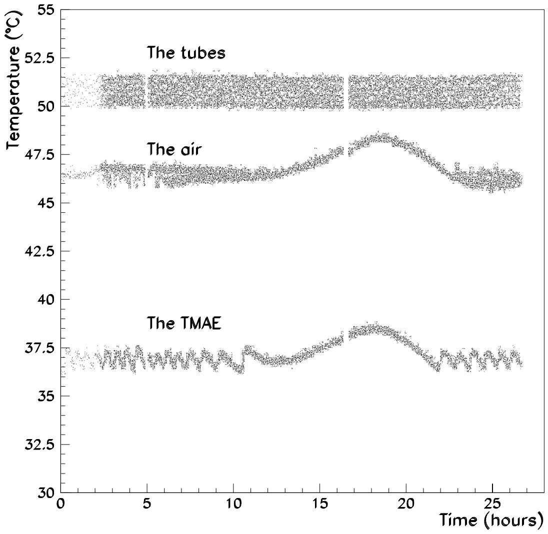

Figure 4.3: *The temperature of three different parts of the RICH versus time during the flight. The gaps in the curves refer to short periods when the data taking was stopped.*

The large changes in temperature during the flight did not have any impact on the performance of the RICH as it was temperature controlled. The action of the control system is illustrated in Figure 4.3 where the temperature in three different parts of the RICH is plotted versus time. The three parts are: the liquid TMAE; the air inside the box containing the RICH; and the tubes connecting the TMAE container with the RICH. As shown in the figure, the temperature of the tubes is kept at an average value of 51 °C with a maximum variation of ±0.7 °C. This should be compared with the 20 °C change of payload temperature. The temperature of the air inside the RICH varied within ±0.5 °C as long as the payload temperature was below the set point of the controller. When the payload was above the set point, the regulation did not have any effect and it could only leave the heating switched off. After 12 hours the air temperature started to follow the payload temperature instead of being regulated and increased by 2 °C above the set point. Later in the flight, regulation started again and a constant temperature was achieved once more. The temperature profile of the TMAE has a similar shape as the air temperature. Note that the set points for the three different sensors were adjusted to three individual values. The oscillation in the TMAE temperature is not seen for the air or tubes. The reason is the difference in time constant for the three different systems. For the TMAE, the time constant is much larger and the rise and fall during one on-off cycle is much slower and possible to resolve. The same effect would have been seen for the air and the tubes in a plot with a better time resolution.

Unlike temperature, pressure changes did affect the RICH. The gain of the MWPC of the RICH increased when the pressure went down and in order to maintain a constant behaviour, and to avoid sparks in the chamber, the high voltage (HV) was adjusted, accordingly. The adjustment was based on the analysis of the sample data files. In Figure 4.4 the RICH high voltage versus time is shown. At launch, the high voltage was set to 1830 V and at the end of the flight the high voltage had been adjusted to 1650 V. The adjustment was made in steps, normally 10 V per step. During the last part of the flight, when no direct communication with the payload was possible and only engineering data was avaliable, the HV was changed following a fixed schedule and not based on any on-line analysis.

The change in gain was noticed when properties like "sum of wire signals" and "sum of pad signals" were monitored. These variables were calculated using the sample data files by summing all signals generated in the anode wires and pads respectively. The sums were

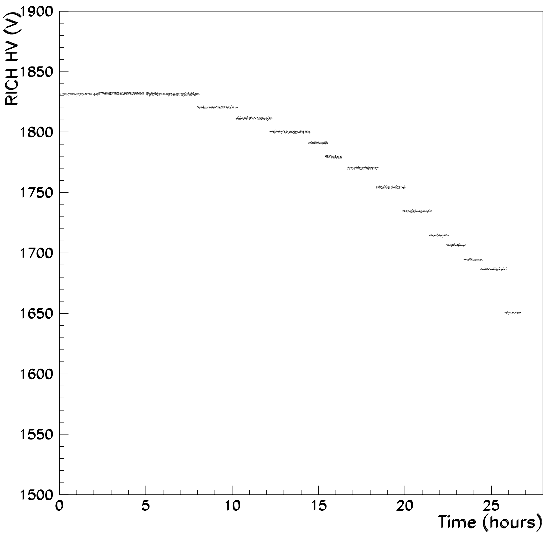

Figure 4.4: *The high voltage supply to the RICH versus time during the flight*

calculated using raw data. In Figure 4.5 the sum of pads are plotted versus time. Note that this plot is made with data recorded at float altitude with a minimum requirement on the tracking quality. As seen in the figure, the sum is increasing overall with a step-like structure. The increase is due to the falling pressure and hence increased gain, and the structure is related to the change of the high voltage. The figure shows that changes of high voltage were necessary to limit gain variations. A high gain was not only dangerous because of the risk of sparks, it also reduced the identification capabilities of the RICH.

4.4.3 The other detectors

The other detectors were affected by changes in pressure and temperature in varying degrees.

For the calorimeter cooling system to work properly it needed

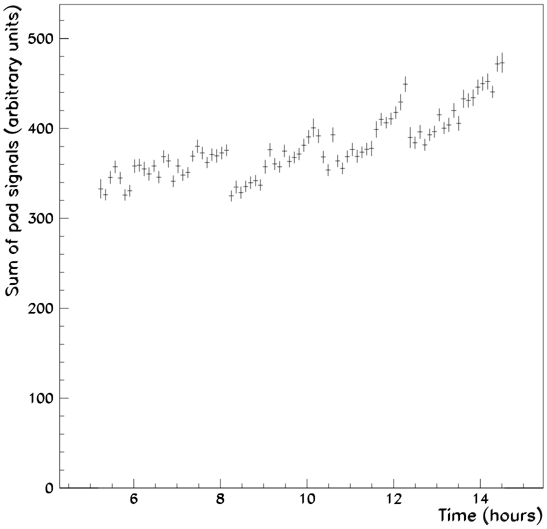

Figure 4.5: *The sum of pad signals versus time during the flight. The increase of the sum is due to the falling pressure and the step-like structure is related to the change of the high voltage.*

to be connected to the outside of the payload. The connection was via a tube and the outlet was controlled by a valve. During the flight the cooling system worked only for the first three hours. The valve was closed to see if the leak in the gondola was due to the calorimeter cooling system. When the valve was closed, the leakage did not stop, and the valve could not be reopened. The conclusion was that the combination of low pressure and magnetic field made the valve malfunction. When the valve was closed, the temperature of the silicon detectors increased. An increase of temperature implies an increase of the dark current in the silicon detectors and so an increase of global noise of the detector. This led to a larger number of words transmitted per event. However, the signal to noise ratio did not decrease significantly and the performance of the calorimeter was essentially constant during the whole flight.

The drift chamber and multiwire proportional chambers of the tracking system are gaseous detectors and hence sensitive to the pressure. As for the RICH, the high voltage was adjusted several times during the flight. For the drift chambers, both the shaping and drift voltages were adjusted. In post-flight analysis, the tracking system was calibrated for the changing conditions and the remaining variation is small.

The time-of-flight system was affected in two ways. The pedestals for the ADCs and TDCs drifted, and the gain of the photomultipliers changed, see Chapter 6 for details.

During the last hours of the flight two events occurred which limit the amount of data for analysis. After 22.5 hours one of the drift chambers was turned off due to an excessive current drawn by the shaping voltage. It was later recovered, but at that time the batteries giving -6 V to the payload had lost their power which affected the other detectors adversely.

4.5 Summary of the Flight Campaign

The flight can be considered as very successful. It was the first time a RICH detector capable of identifying Z=1 particles was used in a cosmic ray experiment. Together with the imaging calorimeter it formed the most advanced cosmic ray payload ever flown with a balloon.

The large variations of the conditions were compensated as far as possible during the flight and further improvements in detector performances has been possible during the post-flight data analysis.

Chapter 5

Tracking System Data

The tracking system provides a measurement of the rigidity of an incident particle. The rigidity is given by the deflection of the particle in the magnetic field. The trajectory of the particle is measured with a combination of drift chambers and multiwire proportional chambers. This chapter describes the calibration of the chambers, the fitting procedure and the performance of the combined system during the flight.

5.1 Calibration of the Tracking Chambers

When a particle passes through a drift cell, it ionizes the gas and the ionization electrons drift under influence of the electric (and magnetic) field to the nearest sense wire. The drift time is related to the distance between the incident particle and the sense wire. In order to transform the measured drift time into a distance, the-drift-time-to-position relation (DPR) must be known. The DPR depends upon the gas characteristics, the electric field, the pressure, and temperature and is deduced from flight data by applying an iterative least-squares fitting technique of the track (described below). The iteration stops when a stable DPR is obtained with a minimum χ^2 between the fitted and measured positions. The resulting spatial resolution within a drift cell is better than 100 μm for about 70 % of the possible drift distances [35].

During the CAPRICE flight the temperature and pressure of the payload changed with time. To compensate for the pressure changes, the high voltage of the drift chambers was adjusted several times. The changing conditions affected the drift-time-to-position relation and a time dependent calibration, obtained by splitting the flight data in several intervals, is used. After the calibrations, the remaining variations in the performance of the drift chambers are small.

When a particle traverses a multiwire proportional chamber, it ionizes the gas and an avalanche of electrons occurs close to an anode wire. The avalanche induces pulses in that wire as well as in the cathode wire plane and the pulses are read out via delay lines. The position of the induced pulses, and thereby the position of the particle, is measured from the arrival time in both ends of the delay line. To have a high resolution in the position measurement, the delay lines must be calibrated. For the x coordinate, the delay lines are carefully calibrated to compensate for position dependence in their propagation velocities. For the y coordinate, where the resolution is limited by the wire spacing, the calibration is less crucial. Like the drift chambers, the MWPCs are calibrated in an iterative process comparing the measured positions with the positions given by the track reconstruction [36].

5.2 Track Fitting

Figure 5.1 shows the fitted track of a 2.0 GV/c proton, selected with the RICH and scintillators. In the bending view, to the left in the figure, the deflection of the particle is visible. To the right, in the non-bending view, the track appears as a straight line. The measured positions in the MWPCs are indicated with crosses and in the DC with circles. The radius of a circle is proportional to the drift time in a drift cell.

The track fitting process is based on an iterative least squares procedure developed by Solmitz and Burkhardt, see [36] for references. In this procedure, a particle's "state" is described by five parameters: x and y coordinates, two directional angles ($\partial x/\partial z$ and $\partial y/\partial z$), and the particle's deflection (η). Before the first iteration,

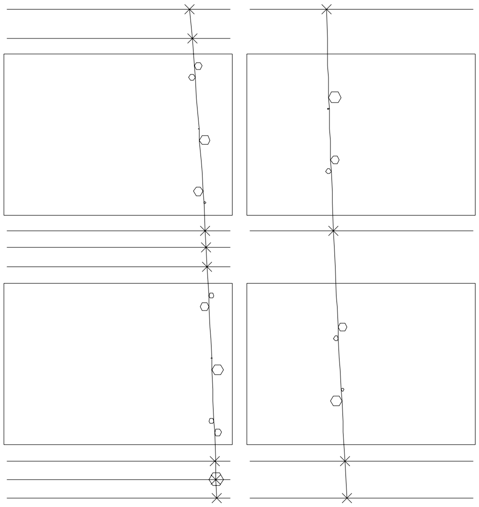

Figure 5.1: *The fitted track of a 2.0 GV/c proton. The crosses indicate hits in the MWPC and circles in the DC with the radius proportional to the drift time. (The MWPC with both a cross and a circle is broken and not included in the fit.) The bending view (x) is to the left and the non-bending view (y) to the right.*

an initial guess is done of the state, based on a straight line fit. In the first iteration, the track fit is done separately in the two drift chambers. When the track is found in the two chambers, an over all fit is done combining the information from the two chambers. In the next step of the fitting procedure, the information from the multiwire proportional chambers is added. Before including them in the fit, a check is done to exclude chambers with a measured position far away from the previously fitted track. Last an over all fit is done with both the drift chambers and multiwire proportional chambers. When the fit has converged, the number of points used in the fit is counted for both x and y, hereafter called x_{hit} and y_{hit}. The fitted trajectory is also compared to the measured coordinates and chi-squares are computed for both x and y:

$$\chi_{\mathrm{x}}^{\prime 2} = \sum_{i}^{\mathrm{x}_{hit}} (\frac{\mathrm{x}(i)_{fit} - \mathrm{x}(i)_{meas}}{\sigma_{\mathrm{x}(i)_{meas}}})^2 , \tag{5.1}$$

$$\chi_{\mathrm{y}}^{\prime 2} = \sum_{i}^{\mathrm{y}_{hit}} (\frac{\mathrm{y}(i)_{fit} - \mathrm{y}(i)_{meas}}{\sigma_{\mathrm{y}(i)_{meas}}})^2 \tag{5.2}$$

where $\sigma_{\mathrm{x}(i)_{meas}}$ and $\sigma_{\mathrm{y}(i)_{meas}}$ are the resolution of the measurement in drift cell (or chamber) i. The chi-squares are then normalized.

5.3 Performance

The distribution of the number of hits included in the fit is shown in Figure 5.2 for |Z|=1 particles from flight data. The charge selection is done with the scintillator dE/dx, no other cuts are imposed on the data. For the fit to converge, a minimum number of points is required, four in x three in y, respectively. This is not enough to assure a good track reconstruction. In the antiproton and proton analysis, at least 11 points are required in x and at least 7 points in y. In Figure 5.2 it is shown that for the negative particles there are relatively more events with a low number of points in the fit. This is due to "spill over", i.e. positive particles that have been reconstructed to have a negative curvature instead of positive. The effect is only noticed on the negative side since the largest fraction of the cosmic rays are positively charged. (The spill over of negative particles to the positive side is negligible.)

To describe the particle's path in the magnetic field in the two views, 5 parameters are needed, see section 5.2. Thus, for a fitted track with N (x_{hit}+y_{hit}) points, the number of degrees of freedom is N-5. The chi-square distributions presented in Figure 5.3 are normalized in the following way:

$$\chi_{\mathrm{x}}^{2} = \chi_{\mathrm{x}}^{\prime 2}/(\mathrm{x}_{hit} - 3) \tag{5.3}$$

$$\chi_{\mathrm{y}}^{2} = \chi_{\mathrm{y}}^{\prime 2}/(\mathrm{y}_{hit} - 2) \tag{5.4}$$

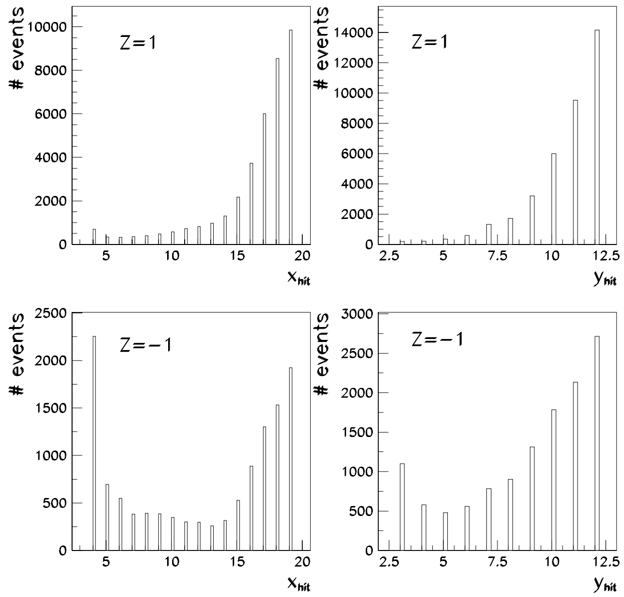

Figure 5.2: *The resulting number of points used for fit for positive and negative particles from flight data.*

The normalization is done with the assumption that the deflection only takes place in x. For the distributions in Figure 5.3, at least 11 points are required in x and at least 7 in y. The conclusions drawn from the chi-squares distributions are that positive and negative particles behave the same in the tracking system and that the normalization is correctly done (the distributions are peaked around 1). In the selection criteria for antiprotons and protons, restrictions are put on the normalized chi-squares to reject scattered events.

5.4 Rigidity Measurement

The most important parameter measured by the tracking system is the rigidity (R) of the incident particle. The rigidity is defined as

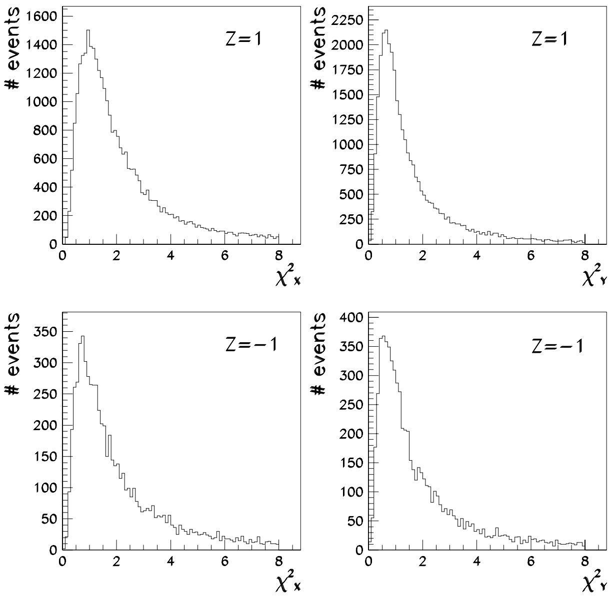

Figure 5.3: *The resulting chi-square distribution of the fit for positive and negative particles from flight data.*

the momentum per unit charge. It is calculated from the measured deflection (η) in the magnetic field as R=1/η. The performance of the tracking system is limited by the strength of the magnetic field, the number and resolution of the position measurements, and its lever arm. One standard deviation in the deflection distribution from straight tracks is called minimum detectable deflection (MDD). From MDD, the maximum detectable rigidity (MDR) is defined as MDR=1/MDD. The MDR is a good way of characterizing the performance of the tracking system by a single parameter. From the MDR the relative error (ΔR) in the rigidity measurement can be expressed as:

$$\frac{\Delta R}{R} = \frac{R}{MDR} \tag{5.5}$$

In other words, the MDR is the rigidity at which the relative error on the measurement is 100% (ΔR/R=1).

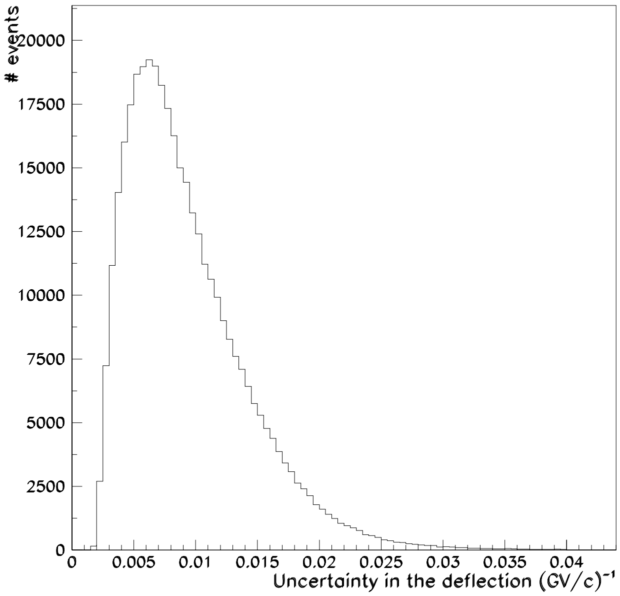

Figure 5.4: *Distribution of the deflection resolution for a sample of protons selected with scintillator dE/dx and basic tracking cuts in the rigidity range 1.2 to 4.0 GV/c.*

When the resolution of the tracking chambers is known (from the calibration), the deflection resolution can be calculated for each track through the magnetic field. Figure 5.4 shows the distribution of the deflection resolution for single charged positive particles in the rigidity range 1.2 to 4.0 GV/c, selected with the dE/dx information from the scintillators and with the basic cuts on the tracking system (see section 9.1.1). The peak of the distribution is at 0.0058 $(GV/c)^{-1}$, corresponding to an MDR of 172 GV/c. This MDR is the average of the whole spectrometer volume. The spatial resolution of the chambers is constant over the active area while the integral of the magnetic field the particle traverses ($\int B \times dl$) is position dependent.

For particles traversing the tracking volume close to the magnet, the $\int B \times \mathrm{d}l$ is larger and hence, the MDR is higher.

Chapter 6

Time-of-flight System Data

The time-of-flight (ToF) system consists of two planes of plastic scintillators, one layer located on top of the tracking system and one underneath it. It provides a measurement of the velocity (β) of the traversing particles as well as the energy loss (dE/dx) in the scintillators.

6.1 Time-of-flight measurement

The time-of-flight is the time it takes for a particle to travel the distance between the top and bottom scintillator planes. It is calculated from the measured arrival times of the light at the two ends of each scintillator paddle.

The principle of the measurement is shown in Figure 6.1. In the figure the trajectory of the particle is shown together with the two scintillator planes. In this simplified picture the time measurement starts when the particle crosses the top scintillator. The time when the light arrives at the end of the scintillators are denoted with $t'_1 \ldots t'_4$:

$$t'_1 = D_1 + \frac{s_1}{v} \tag{6.1}$$

$$t'_2 = D_2 + \frac{s_2}{v} \tag{6.2}$$

$$t'_3 = D_3 + \frac{s_3}{v} + \frac{d}{c\beta} \tag{6.3}$$

$$t'_4 = D_4 + \frac{s_4}{v} + \frac{d}{c\beta} \tag{6.4}$$

$D_1 \ldots D_4$ are constants representing the delay time in electronics and cables, $s_1 \ldots s_4$ are the distances the light has to travel before reaching the end of the scintillators, v is the speed of the light in the scintillators (assumed to be the same in all paddles) and d is the distance the particle travels between the two scintillator planes. This distance is given by the tracking algorithm taking the curved path into account. Finally, $c\beta$ is the speed of the particle.

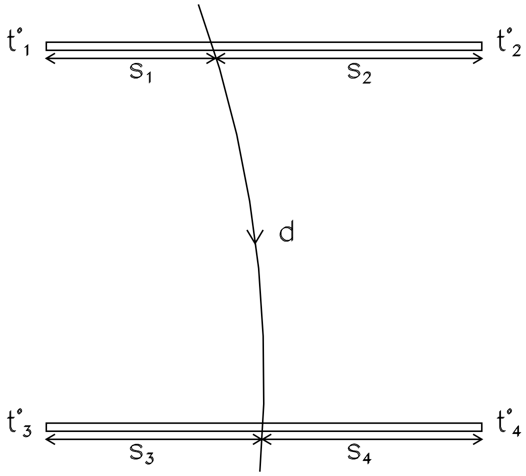

Figure 6.1: *The principle of the ToF measurement: A particle with the speed β traverses the two scintillator planes. $t'_1 \ldots t'_4$ are the arrival times for the light at the end of each scintillator, $s'_1 \ldots s'_4$ are the distances between the impact position and the end of the scintillators and d the distance the particle travelled.*

In practice, these four times are not possible to measure directly. Instead, the arrival times (t_1 to t_3) are measured in relation to a common start signal (t$_4$). In this case t_4 must always arrive before the others and therefore they are delayed before reaching the TDC. Equation 6.1 to 6.4 now becomes:

$$t_1 = D_1 + \frac{s_1}{v} - \frac{s_4}{v} - \frac{d}{c\beta} \tag{6.5}$$

$$t_2 = D_2 + \frac{s_2}{v} - \frac{s_4}{v} - \frac{d}{c\beta} \tag{6.6}$$

$$t_3 = D_3 + \frac{s_3}{v} - \frac{s_4}{v} \tag{6.7}$$

$$t_4 = D_4 \tag{6.8}$$

With this technique, the t_4 distribution is narrow, having a shape close to a delta pulse, with a broadening coming from various effects in the photomultipliers and electronics. The distribution of t_4 is shown in Figure 6.2 a. The data in the figure refers to a 10 minute interval during the flight. The full width at half maximum (FWHM) of t_4 is 4 TDC counts, corresponding to 200 ps. The broadening of t_4 affects the performance of ToF measurement and limits the resolution.

In addition of the broadening of t_4, there is a drift in t_4 with the temperature. This effect was especially pronounced during the flight when the payload temperature varied between 20 and 45 °C, as shown in Figure 4.2. However, this drift does not degrade the performance of the ToF measurement assuming the same drift in all channels. The drift of the start signal t_4 is shown in Figure 6.2 b. It follows very closely the temperature variations during the flight, increasing the first 15 hours and then dropping during the night when the temperature dropped. In the figure, it shown that the width of t_4 remains constant throughout the flight and therefore it will affect the resolution in the same way during the whole flight.

The difference of the sums (DS) of the arrival times in each paddle is given by:

$$DS = (t_3+t_4)-(t_1+t_2) = D_3+D_4-D_1-D_2+\frac{s_3+s_4}{v}-\frac{s_1+s_2}{v}+\frac{2d}{c\beta} \tag{6.9}$$

Grouping the constant terms $D_1 \ldots D_4$, $(s_3+s_4)/v$ and $(s_1+s_2)/v$ together to a single constant C_1 and introducing a scaling term C_2

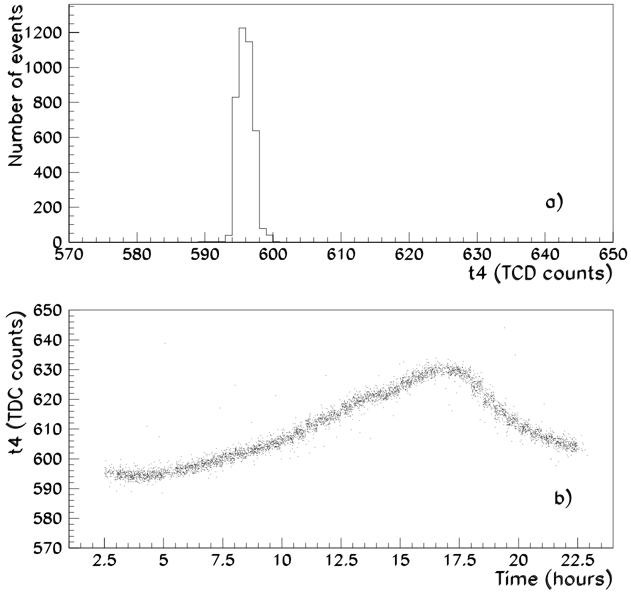

Figure 6.2: *In a) the distribution of the start signal t4 during a 10 minute interval is shown and in b) the start signal t4 is plotted versus time during the flight.*

this can be written as:

$$DS = C_1 + C_2 \times \frac{2d}{c\beta_{rig}} \tag{6.10}$$

In order to calculate the time-of-flight from DS the values of C_1 and C_2 must be determined. There are four possible hit combinations of the paddles with different delays, and hence there are four sets of values for C_1 and C_2. The values of C_1 and C_2 are determined using a large proton sample. The velocity (β_{rig}) of each proton is calculated from the measured rigidity. When plotting $(t_3+t_4)-(t_1+t_2)$ versus $2d/\beta_{rig}$ and fitting a straight line, the values for C_1 and C_2 are derived for each hit combination.

The time-of-flight in ns of a particle is now calculated as:

$$T = \frac{DS - C_1}{2 \times 30 \times C_2} \tag{6.11}$$

The constant 30 is the speed of light in units of cm/ns. The β is calculated from the time-of-flight, using the path length of the particle, as:

$$\beta = \frac{d}{30 \times T} \tag{6.12}$$

6.1.1 Performance

The performance of the time-of-flight system is carefully checked using a large sample of protons. The distribution of the difference between the time-of-flight measured with the scintillators and measured by the magnetic deflection is plotted in Figure 6.3 a. This is the distribution for one of the four paddle combinations. Fitting a Gaussian curve to this distribution the standard deviation is found to be 258 ps. There is however a difference in performance between the four paddle combinations and the combined resolution is slightly worse, around 285 ps.

Note that this is not the final resolution and there are ways to improve it.

6.2 Improvements of the ToF Resolution

Before the signals from the PMTs reach the TDC they pass a discriminator unit. This unit is a leading edge discriminator with a fixed threshold. The threshold is adjusted to a level which is high enough not giving any spurious triggers due to noise but low enough to accept all real signals.

The technique of using a fixed threshold does not give the best timing resolution if the amplitude of the signal varies. The resolution is degraded due to the so-called time-walk effect. This effect comes from that signals with different amplitudes reach the fixed threshold level at different times even though they have the same rise-time and starting point. The variation of amplitude is due to statistical

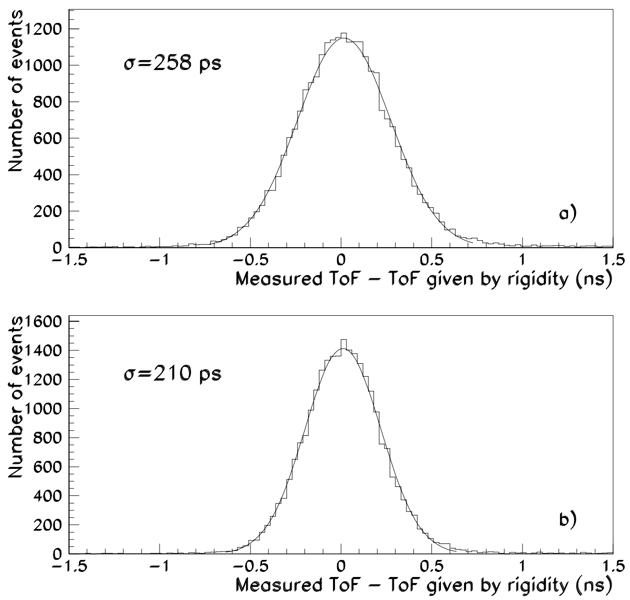

Figure 6.3: *Resolution of the time-of-flight measurement for protons selected with dE/dx in the scintillators. In a) the resolution before corrections and in b) the resolution after the time-walk corrections are applied.*

fluctuations in the scintillation process and the energy loss (dE/dx) of the particle, and attenuation of the light when it propagates in the scintillator to the PMT.

There are two ways to minimize the effect of time-walk. One is to use a constant fraction discriminator technique implemented in the hardware. The second is to use the pulse height information and do an off-line correction. Here the latter method is used.

6.2.1 Time-walk corrections

The effect of time-walk can be compensated by subtracting from the measured time a value depending of the pulse height like:

$$t_{icorr} = t_i - f(ph_{ADC_i}) \tag{6.13}$$

where ph_{ADC_i} is the pulse height measured by the ADC. The function f can be approximated to a good level [17] by:

$$f(ph_{ADC_i}) = \frac{K_i}{\sqrt{ph_{ADC_i}}} \tag{6.14}$$

With this correction, equations 6.5 to 6.8 can be rewritten as:

$$t_{1corr} = D_1 + \frac{s_1}{v} - \frac{s_4}{v} - \frac{d}{c\beta} - \frac{K_1}{\sqrt{ph_{ADC_1}}} + \frac{K_4}{\sqrt{ph_{ADC_4}}} \tag{6.15}$$

$$t_{2corr} = D_2 + \frac{s_2}{v} - \frac{s_4}{v} - \frac{d}{c\beta} - \frac{K_2}{\sqrt{ph_{ADC_2}}} + \frac{K_4}{\sqrt{ph_{ADC_4}}} \tag{6.16}$$

$$t_{3corr} = D_3 + \frac{s_3}{v} - \frac{s_4}{v} - \frac{K_3}{\sqrt{ph_{ADC_3}}} + \frac{K_4}{\sqrt{ph_{ADC_4}}} \tag{6.17}$$

$$t_{4corr} = D_4 \tag{6.18}$$

In the same way as in equation 6.9, the difference of sums is defined and from it the timewalk corrected time-of-flight is expressed as:

$$\begin{aligned} T_{corr} &= [DS - C_1 - (\frac{K_1}{\sqrt{ph_{ADC_1}}} + \frac{K_2}{\sqrt{ph_{ADC_2}}} - \frac{K_3}{\sqrt{ph_{ADC_3}}} - \frac{K_4}{\sqrt{ph_{ADC_4}}})] \\ &\quad \times \frac{1}{2 \times 30 \times C_2} \end{aligned} \tag{6.19}$$

The values of the constants K_i are determined by minimizing the difference between the resulting ToF and the ToF given by the rigidity. For each paddle combination there is an unique set of constants K_i.

6.2.2 Final resolution

When using the time-walk corrected expression for the time-of-flight the resolution is improved. Plotting the same proton sample as in Figure 6.3 a) the resolution is improved to 210 ps compared to 258 ps, as shown in Figure 6.3 b). The combined resolution of the four paddle combinations is 230 ps compared to 285 ps for the non corrected time-of-flight measurement.

The resolution is also checked for muons and alpha particles. The muons were gathered during test runs on the ground before the flight. Compared to protons the resolution is slightly worse, 230 ps, and that is due to a lower light yield for muons in the PMTs. Alpha particles, on the other hand, with their higher charge, are giving much better resolution than protons due to the higher light yield and it is as good as 140 ps. The sample of alpha particles, like the proton sample, is coming from flight data.

6.3 Pulse Height Measurements

The pulse height measurement provides information of the energy loss (dE/dx) of the traversing particle in the scintillator. The dE/dx measurement plays an important role in the analysis. It is used for particle identification and to reject multi-particle events.

Figure 6.4 shows the distribution of the ADC signal from one of the photo multipliers before any corrections are applied. Positive particles (rigidity $>$1.5 GV/c) are selected for this plot and the pedestal is seen as the narrow peak around channel 12 together with the broader signal. In order to have a good performance of the pulse height measurement the scintillator data must be calibrated. First step is to compensate for the pedestal variations during the flight. Second, the pulse height is corrected for the position and incidence angle of the traversing particle in the scintillator. Finally, the gain of the different PMTs are normalized.

6.3.1 Pedestals

There is an off-set in the output of the photomultipliers, noticed as a pedestal in the pulse height spectrum. The pedestal is unique for each tube and it varies with the temperature. The drift is mainly an effect in the PMTs, the ADCs (LeCroy 2249A [37]) are stable within ± 1 ADC channel. The pedestals are adjusted before the flight to be around channel 10 to 12 at 20 °C.

Figure 6.5 a) shows the variation of one pedestal value during the flight. The variation is due to the change in temperature and the shape is close to what is seen for t_4 in Figure 6.2 b). The maximum

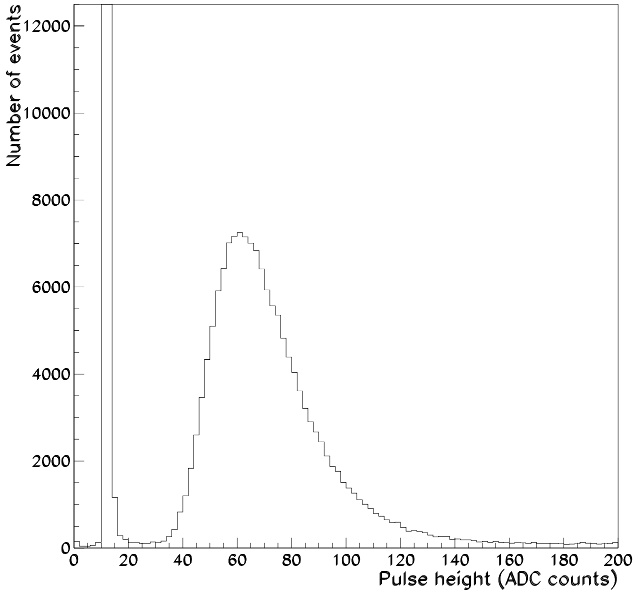

Figure 6.4: *The ADC signal from one of the photo multipliers. The peak at 12 channels is the pedestal.*

variation for this PMT is around 6 channels and is in the same order for the other PMTs. To be able to keep constant efficiency of cuts applied on the pulse height it is necessary to compensate for the pedestal changes. The compensations are done using the temperature given by a sensor placed on the crate containing the ADC module. With this temperature (T_{crate}) the pedestal changes can be described to a good approximation by a linear function:

$$ped(i) = A_0(i) + A_1(i) \times T_{crate} \tag{6.20}$$

The constants $A_0(i)$ and $A_1(i)$ are determined by a straight line fit to allow the pedestal of each tube to be calculated on an event by event basis. These values are subtracted from the measured signal and the resulting variations of the pedestals are within ± 1 ADC channel for all PMTs. Figure 6.5 b) shows the pedestal after the temperature compensation is applied.

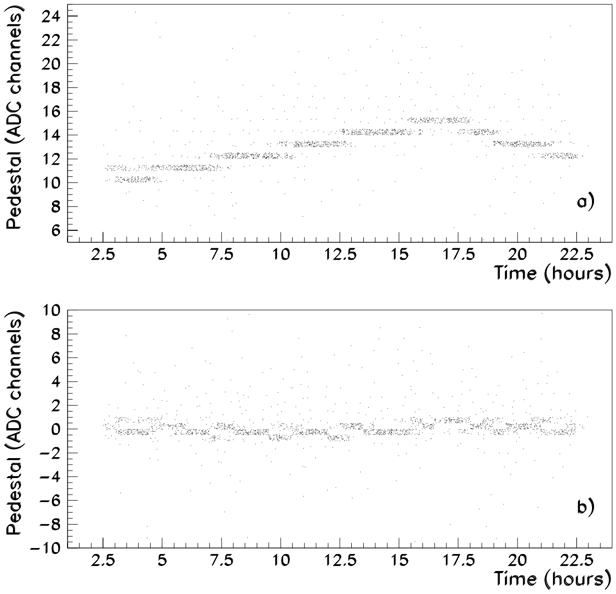

Figure 6.5: *The pedestal before a) and after b) the temperature compensation is applied. The remaining variation is within ± 1 ADC channel*

6.3.2 Corrections for position, incidence angle and gain variations

The pulse height for a single particle varies with the position in the scintillator. The longer the light has to travel in the scintillator the more it is attenuated. This variation is strongest along the paddle but can also be noticed across the paddle. The variation is not the same for all scintillators and the compensation is made individually for all photomultipliers. The response of each photomultiplier is mapped with respect of the impact point in the scintillator given by the tracking. This map is parameterized in both x and y, using a second order two-dimensional polynomial. With the parametrization, a correction is calculated on an event by event basis for a given position.

The pulse height is also corrected for the incidence angle of a particle to compensate for a longer path length in the scintillator. This correction has however only a minor effect on the performance of the pulse height analysis.

The last correction to introduce is a gain normalization. The normalization is done to have same response for all scintillator paddles. It is chosen so that for a minimum ionizing particle the signal is around 100 ADC channels.

6.3.3 β-dependence

To define a cut for the antiproton selection a parametrization is needed for the β-dependence of the energy loss in the scintillators. Plotting the pulse height versus β from rigidity (assuming the mass of a proton) the band of the protons is easy to distinguish, as shown in Figure 6.6 a) for the top and b) bottom scintillators. The protons have pulse height (dE/dx) around 100 for β close to one and for lower β, a rise in dE/dx can be noticed. The horizontal band below the protons are muons and positrons, minimum ionizing for all β in this plot. Above the proton band, alpha particles are seen with a steep rise, starting at 400 for β close to one. Between these two bands, the deuterons are barely seen.

The distribution of the pulse height for protons (similar to that in Figure 6.4) is plotted for several β intervals, from 0.35 to 1. In each interval, the peak position is found and from the peak positions, the β-dependence is derived. For the top scintillators it results in:

$$\frac{dE}{dX} \propto \beta^{-1.84 \pm 0.01} \tag{6.21}$$

and for the bottom scintillator in:

$$\frac{dE}{dX} \propto \beta^{-1.82 \pm 0.01} \tag{6.22}$$

The resolution of the dE/dx-measurement is also derived. It is defined as the width of the left side of the peak of the pulse height spectrum. For minimum ionizing protons, the relative resolution for is (12±1)% and (14±1)% for the top and bottom scintillators, respectively.

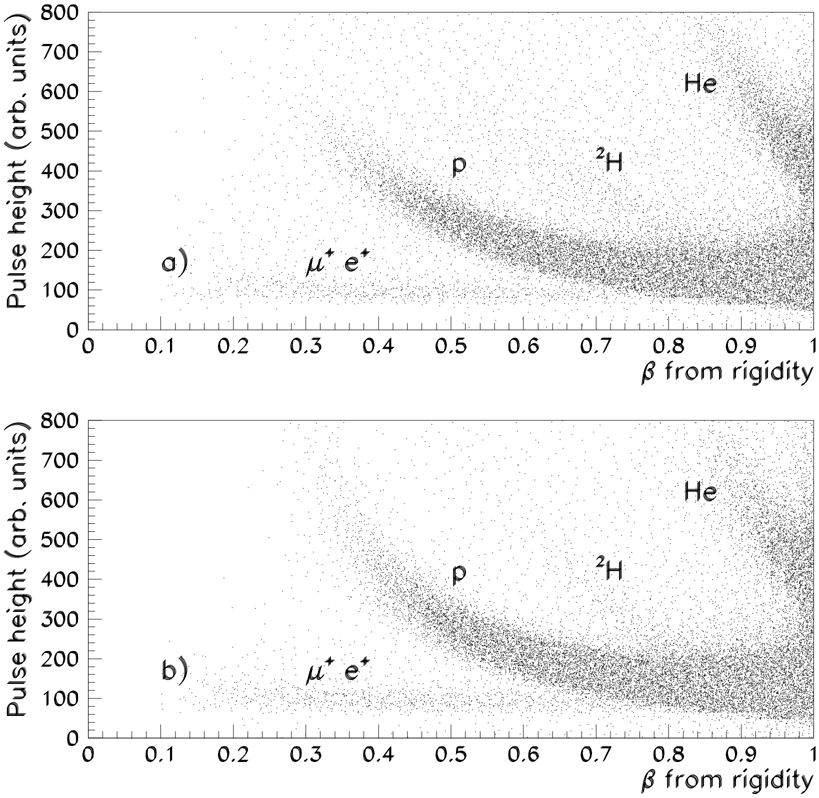

Figure 6.6: *Pulse height versus β from rigidity (assuming the mass of a proton) for the top a) and bottom b) scintillator. The band of protons are clearly visible together with muons and positrons, deuterons, and alpha particles.*

Chapter 7

Calorimeter Data

The silicon-tungsten calorimeter is designed to select particles through a fine sampling of the longitudinal and transversal energy distribution. In this chapter the calibration and performance of the calorimeter are presented.

7.1 Calorimeter Signals

When a charged particle traverses matter, it loses energy primarily through ionization. The average differential energy loss (dE/dx) due to this interaction is described by the Bethe-Bloch formula [53] and the energy loss depends only on the β of the incident particle and not on its mass. The energy loss decreases rapidly for increasing β, reaching a minimum value for $\beta \simeq 0.97$, and then slowly increasing for $\beta \rightarrow 1$. The region of minimum loss is called the minimum ionizing region and particles that lose energy close to the minimum are called minimum ionizing particles.

In a medium of thickness δx, the average energy loss is (dE/dx)δx. In a thin medium, like the silicon detectors, the energy loss is a result of a small number of collisions, each one with a wide range of possible energy transfers. The distribution of the energy loss in this case is described by the Landau theory, see [54].

A particle traversing the calorimeter produces a number of electron-hole pairs in the silicon detectors, proportional to the energy lost by the particle. The holes and electrons drift toward the anode and cathode respectively, where they are collected. The signals from the silicon strips are amplified with two different gains (to give a large dynamic range) and read by an 8-bit ADC. The ADC signals above a hardware threshold are recorded.

7.1.1 Amplification ×16

Figure 7.1 shows the energy loss distribution for a single silicon strip using several thousands events from the flight data. The data in the figure is a combination of minimum ionizing particles, slow protons, alpha particles and heavier nuclei, and interacting particles. The first peak is the (by hardware) truncated tail of the pedestal. The second peak is the most probable energy lost by a minimum ionizing

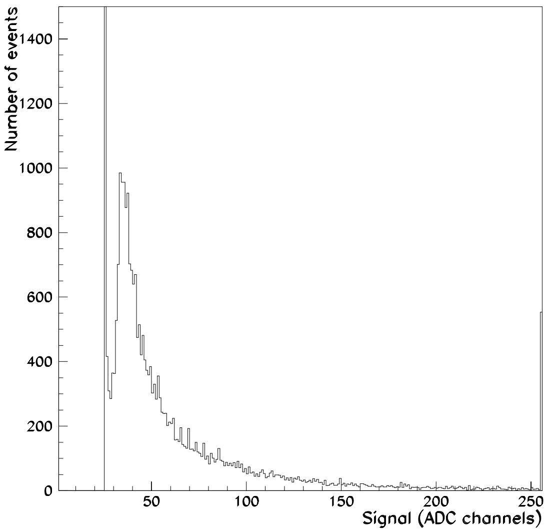

Figure 7.1: *Distribution of the energy loss in one calorimeter strip in ADC channels for the amplification ×16 from flight data. The first peak is the truncated tail of the pedestal, the second peak is the most probable energy lost by a minimum ionizing particle. The saturation on the last (256th) ADC channel is also shown.*

particle defined as one "mip". The tail of the distribution is due to interaction in the calorimeter, non-minimum ionizing and Z>1 particles. A good separation between the two peaks can be noticed and the resulting signal to noise ratio is 10 or better for most of the strips. For a limited number of strips, no separation between signal and pedestal is found in amplification ×16.

7.1.2 Amplification ×1

Amplification ×1 is only used for high energy losses. With this amplification, the dynamic range is extended and the maximum detected energy is over 300 mip. During the flight the hardware threshold was put to $\sim$ 8 mip. If strips that are too noisy in amplification ×16, present a resonable signal in amplification ×1, then only this signal is used.

7.1.3 Calorimeter calibration

The normalization coefficients for each channel are obtained by fitting the distributions of the ADC signals after the pedestals are subtracted. The pedestals were calculated before the flight. It is the second peak in Figure 7.1 that is used for the calibration of amplification ×16. For the fit of the distribution, a semi-gaussian function (to take care of the electronic noise) plus a Landau tail (for minimum ionizing particles) and plus a constant factor (for interacting particles etc) is used.

The calibration of the amplification ×1 is obtained from the ratio between the ADC signals obtained with the two gains and the normalization coefficients of the amplification ×16. The ratio is calculated in the region where the signal from the two gains are overlapping.

After the calibration, the data are converted to units of mip and a software threshold of 0.7 mip is applied, i.e. all data from single strips with a signal lower than this value are put to zero. This threshold is the best compromise between minimization of the noise and efficiency in detecting the signal.

7.1.4 Results

The calibration of the flight data results in that about 95% of the strips are working in both amplifications, 3% gives no useful signal due to detector or electronic failure, and the remaining strips can be used only for high energy losses. The resulting energy resolution for detected energies below 20 mip is around 0.15 mip. Above 20 mip, the amplification ×16 saturates and the other gain is used. The absolute energy resolution becomes about 16 times worse but, still, the relative resolution is better than 20 %.

When comparing the calibration coefficients obtained before and during the flight, no statistically significant difference is found implying that pedestals and gains had no significant variations.

7.2 Non-interacting Particles

Figure 7.2 shows a 0.9 GV/c negative muon from ground data in the two views of the calorimeter. The numbers in the figure indicate the energy loss in mip. A minimum ionizing particle loses a small amount of its kinetic energy, 54 MeV, traversing the calorimeter. Normally, a single particle deposits its energy in one single strip per plane unless the particle crosses a detector between two strips. The resulting distributions of number of hits and detected energy in the calorimeter of minimum ionizing particles are peaked at 16 (8 planes × 2 views). Figure 7.3 a) shows the number of hits and b) the energy loss distribution obtained using negatively charged events from ground data with rigidity greater than 1 GV/c. These events are mainly muons with a small number of electrons (less than 1%) and the resulting distributions are typical for minimum ionizing particles. A low number of strips hits corresponds to particles passing through broken strips or in the dead areas between the silicon detectors.[1]

The distribution of the energy loss is much broader than the distribution of number of hits. This is due to the large fluctuations in the energy lost by the particles crossing the silicon strips. Thus, the number of strips hit is a better parameter to define non interacting

---

[1] The non sensitive gap is about 3.7 mm wide, corresponding to about 10 % of the total area.

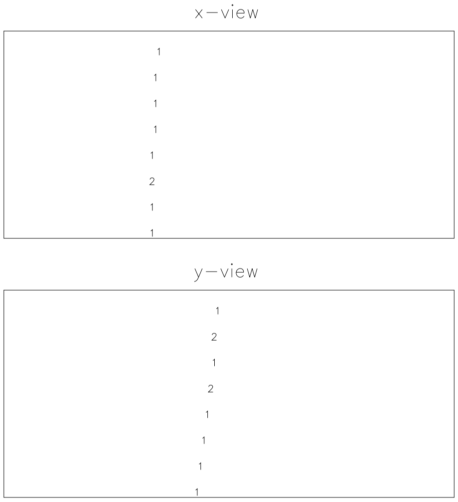

Figure 7.2: *Hits and energy losses distribution in the x and y views of the calorimeter for a 0.9 GV/c negative muon from ground data. The numbers indicate the energy loss in mip.*

particles than the energy loss. This is true also for non relativistic particles if they do not interact in the calorimeter. In this case, the energy loss will be higher than 1 mip per strip with an average given by the the Bethe-Bloch formula, while the number of strips hit will still be around 16 or lower. Hence, requiring that the number of strips hit less than 22 is an efficient selection criterion for non interacting particles with, at least above 1 GV/c, a low contamination from showers (see Figure 7.3 and Figure 7.5).

7.3 Showers in the Calorimeter

Figure 7.4 shows an electromagnetic shower induced by a 2.1 GV/c electron (Top) and a hadronic shower produced by a 2 GV/c interacting proton (Bottom). The difference in topology and energy loss of the two showers are evident as well as the difference from

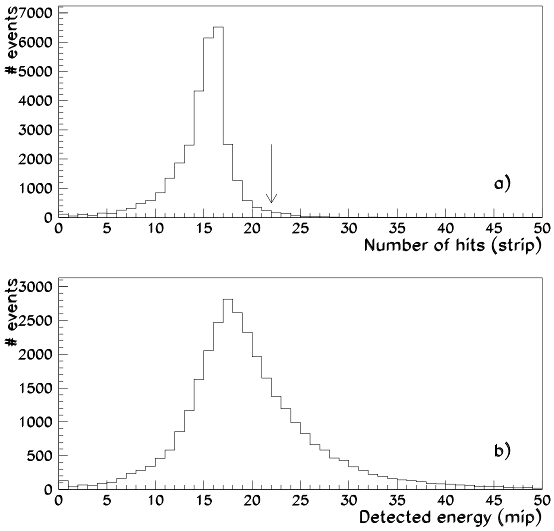

Figure 7.3: *Distribution of: a) number of strips hit and b) energy loss inside the calorimeter for negatively charged particles with a rigidity greater than 1 GV/c for ground data. The arrow in a) indicates the value below which more than 95% of the non interacting particles are found.*

the muon in Figure 7.2. The different features of the electromagnetic shower enable a clear separation between electrons/positrons and other particles. These features are used for identification of antiprotons against a background of electrons, see section 9.4.

Figure 7.5 shows the distribution of the number of strips hit for negatively charged particles from the flight data with a rigidity greater than 1 GV/c. The first narrow peak corresponds to non-interacting particles (mainly negative muons and pions). The second broader peak is due to showering particles (mainly electrons and interacting pions). A cut at 22 strips allows a good separation between these two types of particles.

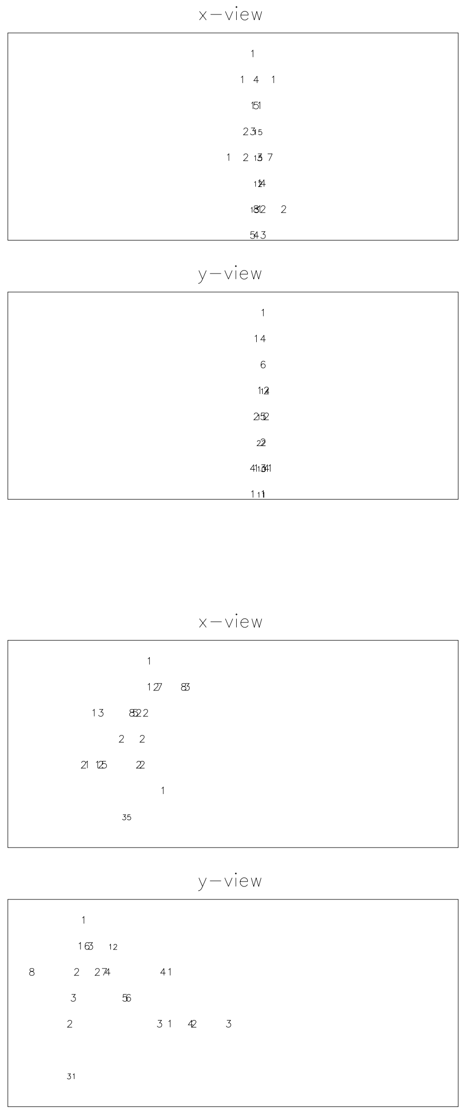

Figure 7.4: *Hits and energy losses in the x and y views of the calorimeter. Top: 2.1 GV/c electron; bottom: 2.0 GV/c proton from the flight data. The numbers indicate the energy loss in mip.*

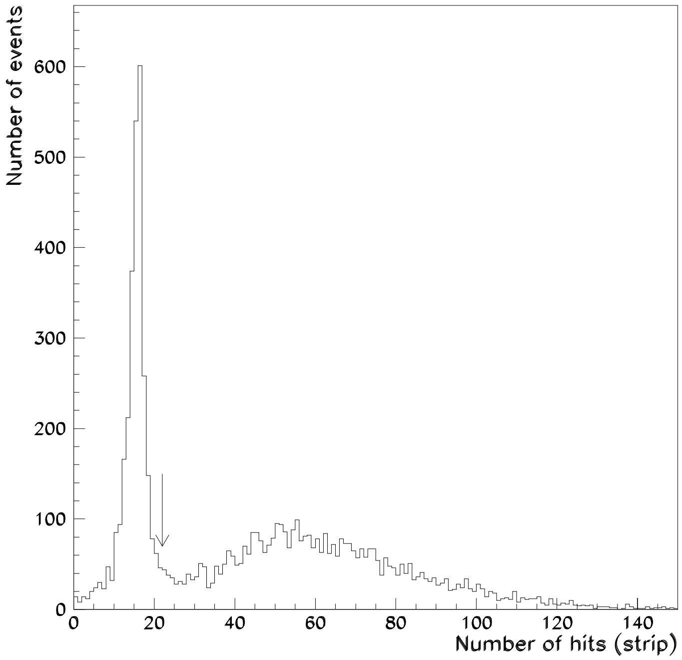

Figure 7.5: *Distribution of the number of strips hit inside the calorimeter using negatively charged particles from the flight data with rigidity greater than 1 GV/c. The distribution due to showering particles is clearly separated from the distribution due to non interacting particles. The arrow indicates the value below which less than 1% of the showering particles are found.*

Chapter 8

RICH detector data

This chapter describes the analysis of data from the RICH detector, from raw data to the Cherenkov angle.

8.1 Single Events

When a charged particle traverses the RICH, Cherenkov light is emitted in the radiator and detected in both the anode wires and the pad plane. Figure 8.1 shows a single event detected in the pad plane (size 512×512 mm^2). The event is a proton (β=0.93), at perpendicular incidence angle (0.3°), selected from flight data with the RICH and scintillator dE/dx. The β is measured by the RICH and the incidence angle is determined by the tracking system. The small squares in the figure indicate pads that are hit: filled squares for pads with signal due to Cherenkov photons and open squares for the pads with the induced signal from ionization of the amplification gas by the particle itself. The size of a square is proportional to the amplitude of the signal and a pad with a high signal corresponds to a large square. The ring of Cherenkov light is clearly visible and there is a good separation between the Cherenkov light and the primary ionization.

Normally, each photoelectron induces a signal in more than one pad. It is found that on average, 2.3 pads are hit per photoelectron [29]. In this event, 27 pads are hit due to Cherenkov light, corresponding to 12 photoelectrons. The number of photoelectrons

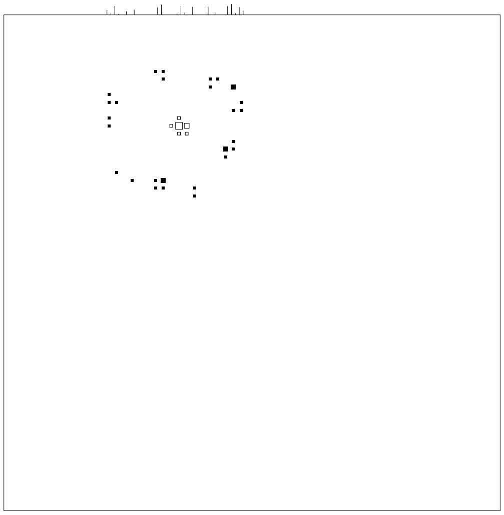

Figure 8.1: *A single event in the RICH. The ring of Cherenkov light is clearly visible from proton (β=0.93) at perpendicular incidence. The radius of the ring is 7 cm. The vertical lines on top of the figure indicate anode wires that are hit and the length of a line corresponds to the amplitude of the signal.*

detected is proportional to the amount of Cherenkov light that enters the photosensitive volume. The amount of Cherenkov light emitted is depending on both the incidence angle and the velocity of the particle, as described later in this chapter.

Futhermore, the signal from the ionization of the amplification gas by the particle is also distributed over several pads. In this particular event, 6 pads are hit due to the ionization. The pad with the highest signal, i.e. the largest square, coincides with the position of where the particle traversed the pad plane. This signal is so high that the pre-amplifier (the AMPLEX chip) becomes saturated. (The saturation effect is illustrated in Figure 3.4.) The signal from the pre-amplifier is digitized, the maximal signal is 127 ADC channels and all pads with a signal larger than 100 are classified as saturated. This is a unique feature of the pads hit due to the ionization. A photoelectron is not able to give such high signal in a pad.

The vertical lines on top of the figure indicate anode wires that are hit and the length of a line corresponds to the amplitude of the signal. These signals are not used for the reconstruction of the Cherenkov angle, but still provide useful information. For example, the detection efficiency of the wires are close to 100% while the pads have an efficiency of 60% for a single photoelectron. Each pad hit should therefore have a corresponding wire hit. If not, the pad signal is probably due to noise and can be rejected from the Cherenkov angle reconstruction.

In the case of inclined incidence angles, the image of the Cherenkov light is no longer a ring. Due to the high index of refraction of NaF, part of the photons will be trapped inside the radiator and this distorts the image. Instead of having the expected elliptical shape, the image in the pad plane becomes U-shaped, as shown in Figure 8.2. The figure shows an electron ($\beta \sim 1$) at 10° incidence angle, selected by the calorimeter from flight data. The main part of the photoelectrons are accumulated in the central part of the U-shape with a decreasing amount of light further out in the arms. This effect is most clearly noticed for particles with charge Z>1. What is important is that the good separation between the Cherenkov light and the ionization signals remains for inclined events (up to 20°).

The information from the ionization pads is used to calculate the impact position of the particle in the pad plane. The position is derived with a centre of gravity method, taking the signal amplitude into account. The resolution of this method is limited by the size of the pads and by the number of pads used for the calculation. The obtained resolution (Figure 9.8) of $\sim$ 0.15 cm is comparable to the expected value since 8 pads on average give a signal and that the pad size is .80 cm. In Figure 8.2, the centre of the small ring ($\bigcirc$) indicates the resulting position by the centre of gravity calculation. This position is compared with the position of where the particle traversed the pad plane, given by an extrapolation of the tracking system information. The tracking position is indicated in the figure

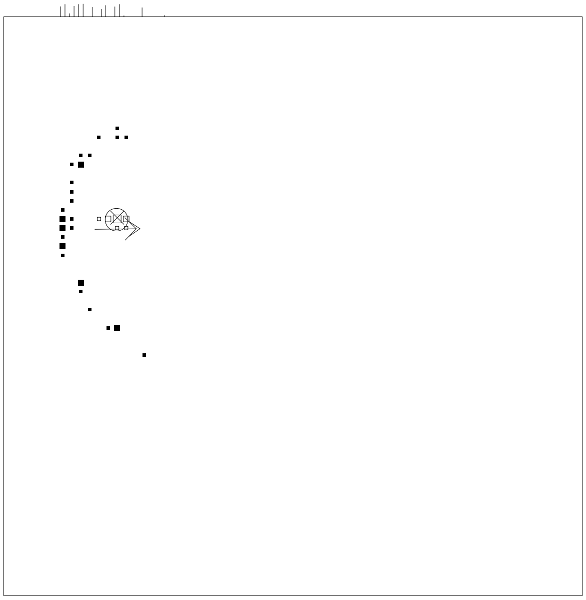

Figure 8.2: *The detected light from an electron at 10° incidence angle. The arrow in the figure is indicating the direction of the particle.*

with an ×. As shown in the figure, the position of the × and the ring agrees very well. In this particular event, the difference is 0.06 cm for the x coordinate and 0.18 cm for the y coordinate. A large difference in x or y indicates that the particle has scattered and the track extrapolation is not valid. For these events, the Cherenkov angle might not be correct, (the algorithm for the Cherenkov angle calculation depends on the tracking information) and they should be rejected. This is used in the selection criteria for antiproton and protons, see Chapter 9.

In the data from the flight, there is noise present in some events even though the noise is very low in the electronics. The number of noisy pads is of the order of one per event (2.5×10^{-4}). In other events, there are more than one particle traversing the RICH at the same time and in some cases, the extra particle is not detected anywhere else in the spectrometer. These events are still possible to reject with the RICH using the location of the saturated pads. In normal events, when one charged particle traverses the RICH, all saturated pads are located in the ionization area. The ionization area is defined by a 5×5 pads matrix surrounding the pad where the particle crossed the pad plane according to the tracking. A pad with a signal above the saturation limit, separated by a distance of more than 3 pads from the ionization area, is defined as a pile-up pad. Hence, the presence of pile-up pads indicate that an additional charged particle went through the RICH.

Figure 8.3 shows an event with two particles detected in the RICH, but only one particle detected in the scintillators and tracking (not shown here). This event is selected with the condition of having a pile-up pad. In this event, some of the pads clearly belonging to the second particle (the lower one in the figure) are used for the calculation of the Cherenkov angle (filled squares) of the first particle identified by the tracking system. Obviously, this leads to a wrongly estimated Cherenkov angle and these events should be rejected in the analysis.

8.2 The Cherenkov Angle

The steps in the reconstruction of the Cherenkov angle are in short the following:

1. decode and process the raw data;
2. calculate the Cherenkov angle for all individual pads;
3. determine the mean Cherenkov angle for the event using a Gaussian potential method.

8.2.1 Processing of data

After decoding, the raw data is processed to derive a number of different parameters. For example, it is important to determine which pads belong to the ionization since they will not be used for the Cherenkov angle determination. The pad with the largest signal is

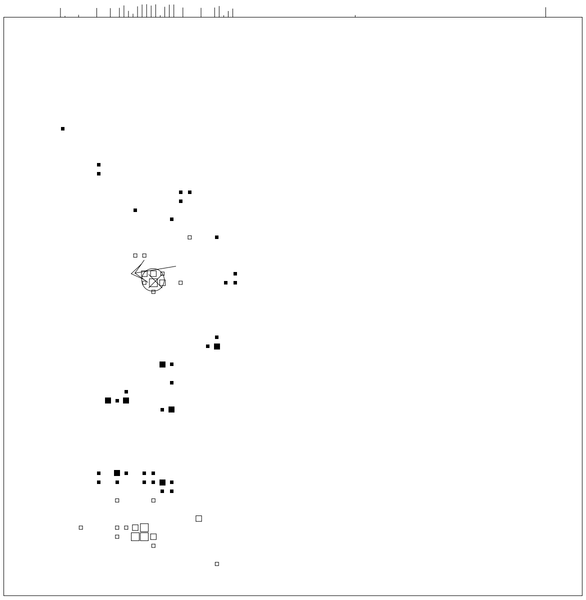

Figure 8.3: *Two particles traversing the RICH at the same time.*

also identified, and the surrounding pads are used for the centre of gravity calculation. The number of saturated pads are counted, and, if located outside the ionization area, they are classified as pile-up pads. In addition, the number of pads hit without a signal in corresponding wires are counted.

The distribution of the number of ionization pads is presented in Figure 8.4 a). The figure is made with a proton sample selected with a combination of scintillator and RICH data. It is found that the number of ionization pads is rather independent of rigidity and incidence angle. An increase is however seen for low β and higher charged particles due to a larger energy loss in the amplification gas.

After the first processing, the Cherenkov angle algorithm calculates the Cherenkov angle for each pad located outside the ionization area. From the Cherenkov relation it appears straight forward to derive the β of the particle from the measured Cherenkov angle and

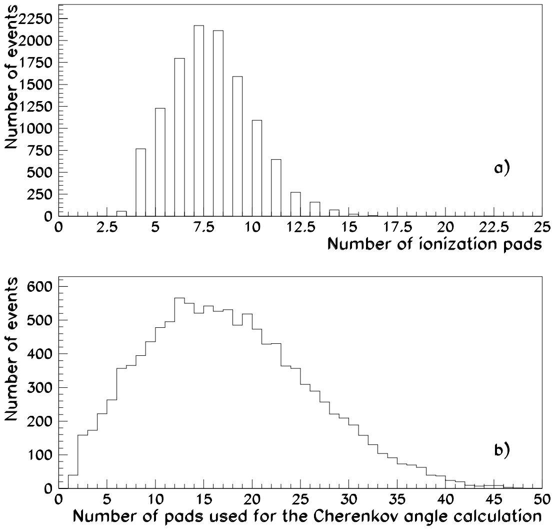

Figure 8.4: *a) The distribution of the number of ionization pads and b) the effective number of pads used for the Cherenkov angle calculation for a proton sample selected in the rigidity range 1.8-2.3 GV/c.*

the index of refraction. In practice, it is more complicated because of the properties of NaF.

8.2.2 Index of refraction

One problem with using a solid radiator is to find a material with an index of refraction less than $\sqrt{2}$. As described in Chapter 3, NaF is the only known solid fulfilling this criterion. However, the index of refraction of NaF varies strongly with the wavelength of the light [45] and photons emitted at different wavelengths will refract differently. For particles at perpendicular incidence and low β, all Cherenkov light will escape the radiator. This is shown in Figure 3.3 where the emitted light refracts at the surface of the crystal into the drift volume. When β increases, the Cherenkov angle becomes larger and part of the light, emitted at short wavelengths and thus higher index

Figure 8.5: *A schematic view of the RICH when a particle with incidence angle* θ *traverses the detector. The Cherenkov light is emitted at an angle* θ_c *and is partly trapped inside the radiator due to total reflection. The particle traverses the pad plane at A, the Cherenkov photon is emitted at C and is converted to a photoelectron at B.*

In summary: The wavelength of the Cherenkov photons that can escape the radiator depends on both the incidence angle and β of the particle. This causes a problem for the calculation of the Cherenkov angle (θ_c). The β of a particle is calculated from the Cherenkov relation using n_{NaF}, but if n_{NaF} depends on the β, how is then n_{NaF}

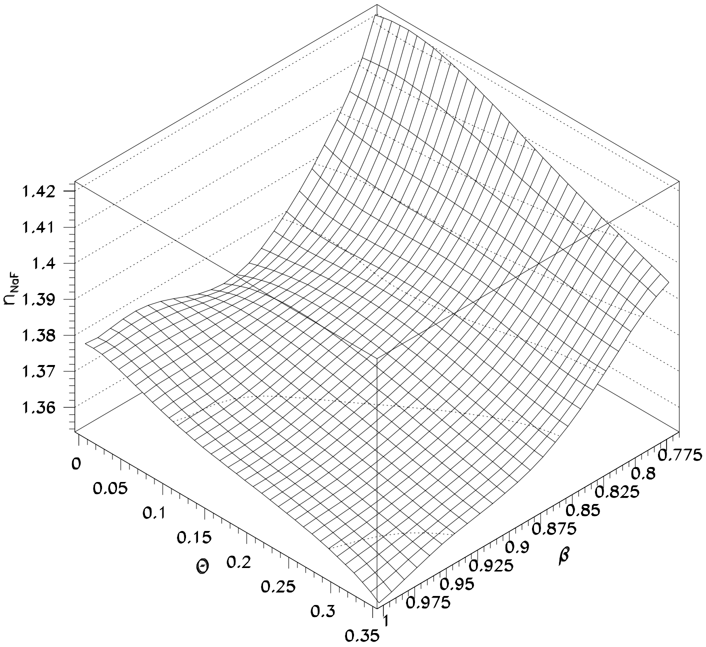

Figure 8.6: *The compensated index of refraction as function of β and θ.*

determined?

To solve this problem, a fit of n_{NaF} as function of β and incidence angle is used. This is called the *compensated* index of refraction. The *compensated* n_{NaF} is not the physical n_{NaF}, which is a property of the crystal itself. The *compensated* n_{NaF} is instead found using the detected Cherenkov photons. The detection of the photons depends on the properties of the RICH and if the properties would change (like change from a quartz window to a CaF window), then the *compensated* n_{NaF} would look different.

The *compensated* n_{NaF} is derived from a proton sample selected with the scintillator dE/dx information, with β calculated from the rigidity and the incidence angle given by the tracking system. For a proton with known β, θ and θ_c, a n_{NaF} value is obtained via the

Cherenkov relation. This is done for a large sample to cover the whole range in β and θ.

Figure 8.6 shows the *compensated* n_{NaF} derived from the proton sample as function of β and θ. The large increase for small β is due to an overlap between the Cherenkov light and the ionization. For these events, the light inside the ionization area is not included in the calculation of the Cherenkov angle. As a consequence, a larger Cherenkov angle is calculated and hence a larger n_{NaF} value is found for these events.

8.2.3 Reconstruction of the Cherenkov angle

As previously mentioned, on average 2.3 pads are hit per photoelectron. In principle this would allow a centre of gravity calculation of the position of the photoelectrons. In practice this is not possible since there is an overlap of pads hit by different photoelectrons. Instead, each pad is treated independently and a Cherenkov angle (θ_i) is calculated geometrically for each pad using an iterative method [56]. In this method, the Cherenkov angle is found as the angle which gives a hit in a specific pad with the given direction of the particle. This is illustrated in Figure 8.5 where the Cherenkov light from one photon is emitted with an angle θ_c in the NaF crystal. After traversing the drift volume, the light enters the photosensitive chamber through the quartz window. In the chamber the photon is converted by the TMAE, amplified by the anode wire and detected in the pad B. The information of the tracking is used to find both the position A of where the particle traversed the pad plane and the incidence angle θ. The extrapolated track is also used to define the point of emission C of the Cherenkov photons in the NaF crystal.

The velocity β of a the particle is determined using a bisection method. Cherenkov light is emitted in NaF for β between 0.76 and 1, defining the limit for the bisection algorithm.

The β is found in the following way:

0. Use β=0.88 as start value;

1. Get the *compensated* n_{NaF} from the fit for the given β and θ;

2. For each pad hit, find the θ_i of a photon emitted in C that is detected in B using the *compensated* n_{NaF} found in 1.;
3. Derive the mean Cherenkov angle θ_c of the event, using a Gaussian potential method, described below;
4. Use θ_c and *compensated* n_{NaF} to calculated a new β via the Cherenkov relation;
5. Compare if the new β is larger or smaller than the β used in 1. to find the β for the next iteration with the bisection method;
6. Repeat step 1. to 5. ten times to find the correct β and thereby the *compensated* n_{NaF} and most important, the Cherenkov angle .

In step 3., the mean Cherenkov angle of the event is determined from the individual Cherenkov angles of each pad hit. If the mean is calculated in a method without weighting the information, all pads will have the same influence on the result. If a Cherenkov angle is determined for all pads without filtering, pads due to noise might be included. Noisy pads located at a large distance from the real image will affect the mean value significantly. The method that determines the mean value must therefore be able to suppress the noise.

8.2.4 Gaussian potential method

In the gaussian potential method [57], pads with Cherenkov angles far from the mean value are suppressed. The suppression is achieved by assigning a weight w_i following a Gaussian distribution around the Cherenkov angle of the event:

$$w_i = e^{\frac{-(\theta_i - \theta_c)^2}{2\sigma_i^2}} \tag{8.1}$$

where σ_i is the error of the Cherenkov angle of that pad. The error of an individual pad is rather independent of β and θ of the particle. For the calculation, a fixed value of 50 mrad is used for all σ_i.

The Cherenkov angle of the event is found by minimizing the function $f(\theta_c)$:

$$f(\theta_c) = -\sum_{i=1}^{n_{pads}} w_i \tag{8.2}$$

The minimization is done by varying θ_c, starting at zero and increasing it in 25 mrad steps. When a minimum of $f(\theta_c)$ is found, the step length is decreased to 5 mrad for the next iterations around the first minimum. When a new minimum is found with a better precision, the step length is decreased once more, and in the last iterations, the minimum is found with 0.5 mrad steps.

The gaussian potential method is illustrated in Figure 8.7. In the figure, the individual Cherenkov angles θ_i are shown together with a Gaussian curve. The method can be pictured like the curve is moved from left to right and the resulting mean value is the value that maximize the weight of all θ_i.

The effective number of pads (n_{eff}) used in the calculation is given by:

$$n_{eff} = \frac{(\sum_i^{n_{pads}} w_i)^2}{\sum_i^{n_{pads}} w_i^2} \tag{8.3}$$

n_{eff} is related to (but not the same as) the number pads hit. For the proton event in Figure 8.1, the number of pads hit is 27 and n_{eff} is 26.2.

The distribution of n_{eff} is presented in Figure 8.4 b. The plot is made with a proton sample selected with a combination of the scintillator and RICH data in the rigidity range 1.8 to 2.3 GV/c. The number of pads hit due to Cherenkov light depends on the incidence angle and Figure 8.4 b shows the average for all angles (0 to 20°). n_{eff} also depends on where the light is detected on the pad plane, see Chapter 9.

8.2.5 Error analysis

There are several sources contributing to the total error on the Cherenkov angle. The two largest single sources of error are:

a. scattering of the particle giving a wrong incidence angle from the track extrapolation;

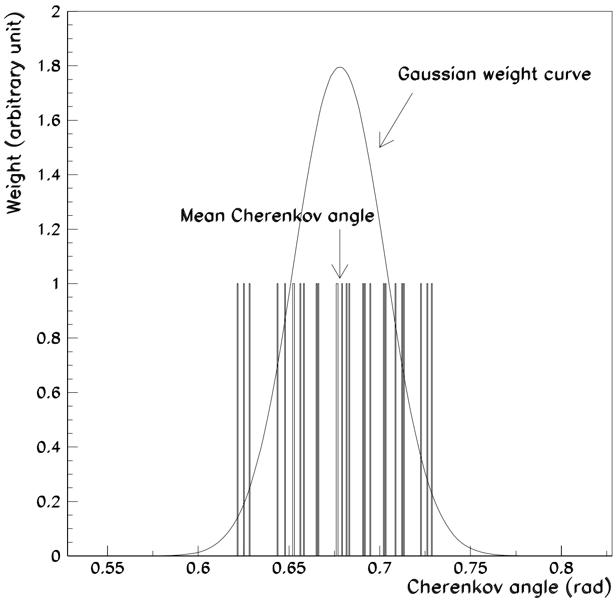

Figure 8.7: *The Gaussian potential method applied on proton event presented in Fig. 8.1*

b. wavelength dependence of the index of refraction of NaF (chromaticity).

Since the Cherenkov angle determination depends on the information given by the tracking system, a scattering and consequent change of direction will propagate directly into the Cherenkov angle. If the scattering of the particle takes place below the NaF, e.g. in the quartz window, electronics, cover of the RICH, or the scintillator, then the Cherenkov photons will be emitted in a different angle with respect of the particle than what is given by the track extrapolation. Not only the angle is affected, the prediction of the impact position in the pad plane can also be wrong. Most of these events are possible to reject by comparing the predicted position from the tracking with the position given by the centre of gravity calculation. Still, if the scattering takes place close to the pad plane, the difference will be small and hence difficult to reject with this cut. The scattering is rigidity dependent and this error becomes significant for low rigidities. For example, a 3 GV/c proton is estimated to scatter on average 1.8 mrad whereas at 1.0 GV/c the average scattering angle increases to 7 mrad.

The chromaticity of NaF broadens the Cherenkov angle distribution since photons emitted with different wavelength will hit the pad plane in different positions. This is most important for a slow particle where the Cherenkov angle is small (giving small ring radius). For these events, a smearing in position in the pad plane will affect the Cherenkov angle more compared to events with larger radius. However, a good separations between antiprotons and the background of pions, muons and electrons is still possible to achieve for slow particles due to the large difference in the expected Cherenkov angle.

The following sources contribute less to the error:

c. uncertainty of the emission point of the photons in the NaF;

d. the finite pad size;

e. multiple scattering in the NaF.

When a particle traverses the NaF radiator, light is emitted at all points along the track but since the emission point of each single photon is unknown, it is assumed to be emitted in the centre of the crystal. Hence, when the photon is traced backwards from the pad to the assumed position in centre of the NaF crystal, the angle can be wrongly reconstructed. This will broaden the Cherenkov angle distribution.

From the detection of the avalanche induced by a photoelectron, it is not possible to locate exactly where above the pad the photoconversion occurred. This introduces an error. For the Cherenkov angle determination, the centre of the pad is assumed to be the position of the avalanche. This error increases for slower particles due to smaller ring radii.

When a particle traverses the radiator, it undergoes multiple scattering. The scattering in the radiator implies that the emission points for the photons are not along a straight line. The different emission points will broaden the Cherenkov angle distribution, comparable to the uncertainty in the emission point. The scattering in the NaF is rigidity dependent and the error increases for lower rigidities.

Example of other sources, with a small or negligible contribution to the error are:

f. uncertainty in the conversion point in the TMAE;
the anode wire pitch;
energy losses of the particle during its passage;
uncertainties in the geometrical dimension.

The estimated error for 3 GV/c protons at perpendicular incidence angle is summarized in Table 8.1. The behaviour of the RICH is well understood. The expected resolution of the Cherenkov angle, taking all the errors into account, agrees with the measured resolution. For a 3 GV/c proton at perpendicular incidence, the total error is estimated to be 5.6 mrad compared to 6.4 mrad found for the flight data.

Source	Error (mrad)
Scattering	1.8
Chromaticity	4.7
Scattering in NaF	1.2
Emission point+ Pad size+ Small errors	2.0

Table 8.1: *The estimated errors in the Cherenkov angle for a 3 GV/c proton at perpendicular incidence. The total error, assuming no correlations, is 5.6 mrad. For flight data, the resolution is found to be 6.4 mrad.*

The measured resolution for protons as function of rigidity for four ranges of the incidence angle is presented in Figure 9.9 and the resolution of the Cherenkov angle for electrons and muons is presented in Figure 9.10.

Chapter 9

Selection of Antiprotons

For the selection of antiprotons, the combined information from the tracking system, time-of-flight system, calorimeter and RICH is used. This chapter describes how the selection criteria are implemented on the data given by the different detectors, the contamination left over by the selection, and the number of identified antiprotons.

9.1 Tracking System Selection Criteria

The primary purpose of the tracking system is to provide a measurement of the rigidity of the particles. However, a good rigidity measurement is not enough for an experiment aiming to determine the antiproton to proton ratio in the cosmic rays. In fact, when a proton traverses the tracking system there is a non negligible probability that it scatters in such way that it appears as having a negative curvature instead of a positive and can be mistaken for an antiproton. The probability is not negligible because the protons are by far the most common particles in the cosmic rays. There are at least a factor of 10^4 to 10^5 more protons than antiprotons. The cuts on the tracking system must therefore be chosen to reject scattered events and provide a reliable rigidity measurement.

9.1.1 Basic cuts on the tracking system data

The basic cuts on the tracking data are:

- the fit routine must converge;
- the number of points in the fit: $x_{hit} \geq 11$; $y_{hit} \geq 7$;
- the goodness of the fit (normalized): $\chi^2_x \leq 4$; $\chi^2_y \leq 8$;
- the uncertainty in the deflection (η): $\sigma_\eta \leq 0.04$ (GV/c)$^{-1}$.

These cuts are partly based on the experience gained using the same tracking system in other balloon flights [58] and [59].

The number of points required in the fit is chosen as a trade off between the efficiency of the tracking system and the reliability of the rigidity measurement. A higher number of points in the fit implies a better measurement but with a lower efficiency. The tracking system is orientated relative to the magnet so that the bending plane is x and there are more chambers in x than y, 19 and 12 respectively. Consequently, more hits are required in the fit for x than for y.

The χ^2 is a measure of the goodness of the fit. A high χ^2 could indicate that the particle has scattered during the passage of the tracking system. For the same reasons as for the number of points in the fit, harder cuts are put on χ^2_x than χ^2_y.

The cut on the uncertainty in the deflection does not affect the selection very much because a large uncertainty is normally due to a small number of points used in the fit and those events are already rejected by the cut on number of points required for the fit. However, a large uncertainty could also be due to that the particle passed a region of weak magnetic field.

9.1.2 Additional cuts on the tracking system data

To further reject scattered protons, the tracking system is divided in two parts consisting of the top and the bottom drift chambers, for which two separate fits are done. For the two fits, the χ^2 and σ_η are calculated and cuts are put on these quantities. There is also a cut to reject events with more than one charged track in the tracking volume. This is done by limiting the number of layers with additional hits more than 4 cm away from the fitted track. The additional cuts are:

- $\chi^2_{x,top} \leq 10$, $\chi^2_{y,top} \leq 10$, $\chi^2_{x,bot} \leq 10$ and $\chi^2_{y,bot} \leq 10$;
- $|\sigma_\eta - \sigma_{\eta,top}| \leq 4 \times \sigma_1$;
- $|\sigma_\eta - \sigma_{\eta,bot}| \leq 4 \times \sigma_2$;
- $|\sigma_{\eta,top} - \sigma_{\eta,bot}| \leq 4 \times \sigma_3$;
- there must not be more than 3 DC layers with additional hits.

The values of σ_i are determined from a large proton sample and are: $\sigma_1 = 0.018(GV/c)^{-1}$, $\sigma_2 = 0.018(GV/c)^{-1}$ and $\sigma_3 = 0.036(GV/c)^{-1}$.

With these additional cuts on the tracking data, all scattered protons are rejected as well as events with more than one track in the tracking volume.

9.2 The Aluminium Bar (not pbar!)

The gondola is connect to the balloon via a 17 kg aluminium bar with a 7 kg steel hook in the centre, situated 2.3 m above the RICH. All this material implies that particles passing through the bar have a probability to interact and produce secondary particles. The bar has an I-shape, 1.5 m long, 20 cm high and the width is 16 cm in the centre decreasing to 5 cm at the ends. The shape is indicated in Figure 9.1 and the centre of the bar (x=25 cm, y=0 cm), stands out with an increased flux compared to the uniform background of muons/pions. The muons/pions are selected as non-interacting particles in the calorimeter and their trajectories are extrapolated to the level of the bar. The production and loss of particles in the non-uniform shaped bar cannot be estimated reliably and hence all particles crossing it are rejected. This reduces the geometrical factor of the spectrometer by approximately 10% for rigidities above 1 GV/c.

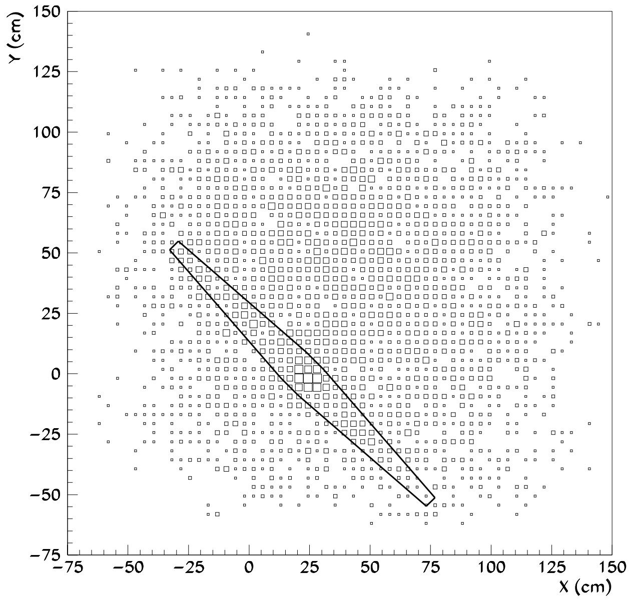

Figure 9.1: *The distribution of negative muons/pions (about 4900 events) at the level of the bar. The area of each square is proportional to the number of events. The shape of the bar is indicated and the large squares at x=25 cm and y=0 cm shows that a larger flux is coming from the centre of the bar where most of the material is located.*

9.3 Time-of-flight System Selection Criteria

The main purpose of the time-of-flight (ToF) measurement is to reject albedo particles. These particles would appear with opposite sign of charge if they were taken as down going instead of up going particles. The dE/dx information given by the scintillators is important for the selection of Z=1 particles. Finally, the hit combination of the two top scintillator paddles is also providing useful information to reject multiple particle events.

The cuts on the dE/dx and hit combination must be made so that multi particle events coming from interactions above the tracking system are rejected. The interactions could take place either in the dome, the RICH or in the top scintillators. Furthermore, there are showers induced in the atmosphere above the payload. On the other hand, antiprotons interacting below the tracking system should be part of the sample and care has to be taken not rejecting them. Therefore no restrictions are put on the bottom scintillators, neither on dE/dx nor on hit combination of the paddles.

9.3.1 Cuts on the scintillator data

In summary the cuts on the scintillator data are:

- ToF > 0 to reject albedo particles;
- dE/dx losses in the top scintillators as expected for protons;
- only one of the two paddles hit in the top scintillator plane.

The albedo rejection is easy to accomplish. The time-of-flight for a $\beta \sim 1$ particle is around 4 ns to be compared with the resolution that is better than 280 ps. This indicates that the chance of taking an albedo particle for being down going is negligible. The albedo rejection is strengthened by the RICH where no Cherenkov light is detected for albedo particles. The RICH is capable of rejecting $(98.1 \pm 0.5)\%$ of the albedo particles.

The dE/dx cut is based on the behaviour of a proton sample selected by the calorimeter. Using the derived β-dependence and resolution (see section 6.3.3), the dE/dX-cut is defined with the upper limit set to the expected peak position for a proton plus 0.8 mip and the lower limit as the peak position minus three times the width of a Gaussian fit of the lower half of the distribution. In this way multi-particle events are rejected.

The hit combination can be used in the following way. If a single particle is traversing the tracking system only one paddle should be hit in the top scintillators. If two paddles are hit it indicates that a second particle was present.

9.4 Calorimeter Selection Criteria

The primary purpose of the calorimeter in the antiproton analysis is to reject electrons which are the main background. The selection criteria are chosen so that more importance is given in not losing too many non-electromagnetic particles than in rejecting all the electrons.

Due to its limited thickness in terms of interaction lengths (less than 0.3 λ_I [53]), the calorimeter is not well suited to identify hadrons by measuring of their energy. Slow particles can instead be identified by sampling the energy loss information in each crossed silicon strip. This permits, for example, selection of non-interacting protons against a background of deuterons for rigidities lower than 3 GV/c. However, for the search of antiprotons at rigidities greater than 1 GV/c, the non-containment in the calorimeter of the particle neither permits to efficiently separate non-interacting antiprotons from negative muons (or pions) nor interacting antiprotons from interacting negative pions. Still the calorimeter plays an important role in the antiproton analysis.

As shown in section 7.3 a clear separation between non-interacting and showering particles can be achieved with the calorimeter for rigidities greater than 1 GV/c. This implies that non-interacting antiprotons can be extracted from the electron background with nearly no contamination and with an efficiency close to 100%. However, the interaction probability in the calorimeter for a 2 GV/c antiproton is about 40%. Due to the low antiproton statistics, it is necessary to chose the calorimeter selection criteria with as high efficiency as possible. Thus it is essential to define selection criteria able to identify hadronic showers induced by interacting antiprotons in an background of electromagnetic showers.

As presented in [32], the longitudinal and transversal segmentation of the calorimeter combined with the measurement of the energy lost by the particles in the silicon detectors permits a high identification power for electromagnetic showers and a high rejection power for hadronic particles.

9.4.1 Double showers in the calorimeter

Some electrons emit a bremsstrahlung photon before entering the calorimeter (e.g. in the RICH or the aluminium cover of the gondola). The electromagnetic shower induced by the photon can be detected in the calorimeter as a second shower. If a second shower is found in the analysis and if it is possible to determine that it is induced by a bremsstrahlung photon, the event is clearly identified as an electron. The detection of the second shower is possible when it is clearly separated from the first one, i.e. the distributions of the strips hit of the two showers do not overlap, and when the energy loss is higher than for a single charged track. The separation of the two showers is normally obtained for kinetic energies lower than 3 GeV. In fact, for these energies the magnetic field can deflect the incoming electron causing it to enter the calorimeter several centimeters away from the bremsstrahlung photon.

The most probable positions, at which a bremsstrahlung photon can be emitted, are the RICH and the aluminium cover of the gondola. The direction of the electron before entering the magnetic field is used to estimate the position of a bremsstrahlung photon in the calorimeter. Note that the emission angle of the photon with respect to the electron is less than about 1 mrad[1]. The event with a second shower is tagged according to if the shower was produced in the RICH or in the aluminium cover. Figure 9.2 shows an event identified with a second shower in the RICH. The second shower is clearly identified.

Some bremsstrahlung photons may instead be produced in the top scintillator or in the tracking system. These photons induce showers in different positions in the calorimeter and, consequently, cannot be identified by the previous method. Because of this possibility, the calorimeter is scanned for a second shower. If a second shower is found, the event is tagged differently from the previous tagging. These double shower events with a single track in the tracking system are, with high probability, electron events. However, also an interacting antiproton may fake a second shower if it loses enough energy away from the fitted track. Thus, in order not losing

---

[1] The bremsstrahlung angle $\theta_{brems} \sim \mathrm{m_e/p_e}$ with m_e and p_e mass and momentum of the electron.

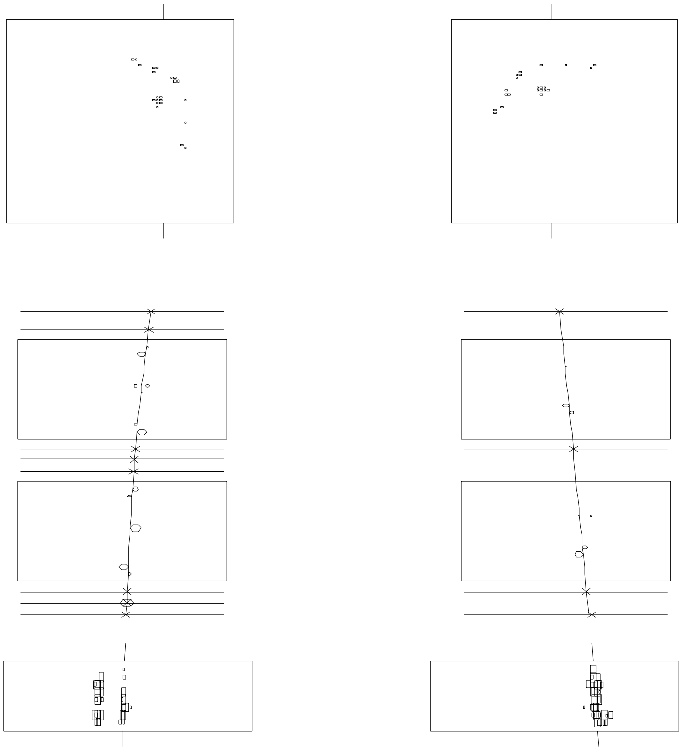

Figure 9.2: *Display of a single 1.3 GV/c electron in the CAPRICE instrument. The electron emits, according to an extrapolation of the track, a bremsstrahlung photon in the RICH. From top to bottom is displayed: the RICH seen from above, the tracking system, and at the bottom the calorimeter. Note that the figure is not to scale, e.g. the calorimeter is significantly thinner than shown in the figure. The calorimeter shows the two electromagnetic showers produced by the electron and by the bremsstrahlung photon, respectively. In the non-bending view (left) the two showers overlap.*

antiprotons, only the events with a bremsstrahlung photon produced in the RICH or the dome are identified as electrons without further analysis.

More than one third of the electrons in the rigidity region 1.2 to 4 GV/c are accompanied by a bremsstrahlung photon reconstructed in the calorimeter.

9.4.2 Shower identification

An electromagnetic shower is identified by imposing cuts on a few parameters based on its shape and energy distribution. These parameters can be classified as:

1. energy-momentum match;
2. longitudinal profile;
3. transversal profile;
4. topological development of the shower;
5. starting point of the shower.

The energy dependence of electromagnetic showers is taken into account by using cuts with a logarithmic dependence on the rigidity. However, not all parameters have a logarithmic dependence and as a consequence there is a slight dependence of the performances of the detector with the energy.

A short description of these parameters and cuts is given below. The description as well as the study of the parameters are based on simulations. Simulations are used because it is not possible to select a pure sample of electrons from the flight data without using the calorimeter and the antiproton sample is limited by statistics. A Monte Carlo simulation reproducing the full instrument including the magnetic field, based on the CERN GEANT/FLUKA-3.21 code [60], is used. The simulation results were compared with the results from beam tests of the calorimeter and a good agreement was found, see [61]. An excellent agreement between this simulation and the experimental data has also been seen in the positron/electron analysis of the flight data, as presented in [32].

All figures shown below are obtained using simulated data. The comparison is done only between electrons and interacting antiprotons. As already pointed out, a clear separation between non-interacting antiprotons and electrons is easily obtained, for example, by a cut on the number of strips hit.

9.4.3 Energy-momentum match

Figure 9.3 shows the total detected energy in the calorimeter divided by the momentum of the particles as function of the rigidity for simulated antiprotons and electrons. For clarity of the figure, the sign of the rigidity of the electrons has been reversed. The energy

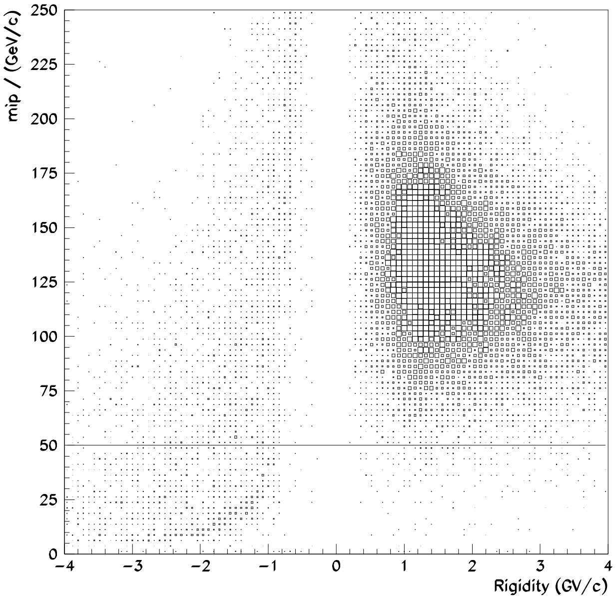

Figure 9.3: *Total detected energy in the calorimeter divided by the momentum of the particles versus the rigidity for antiprotons and electrons. For clarity the electrons have been given positive charge. The solid line at 50 indicates the chosen antiproton cut.*

lost in the silicon strips by electromagnetic showers is proportional to the energy of the electrons. Thus, the total energy losses divided by the energies (momentum) of the particles are distributed around a constant value. This is true at least up to 5 GeV, above this energy the longitudinal leakage (the calorimeter is only 7 X_0) is not negligible and the total energy loss is not anymore proportional to the energy of the electron. In Figure 9.3 this proportionality is clearly seen for electrons.

For interacting antiprotons, the leakage plays an important role (for a full containment of a 2 GeV/c antiproton at least three interaction lengths are needed, more than 80 X_0) and no proportionality with the momentum can be found, as shown in Figure 9.3. The antiproton selection based on this variable, as indicated in the figure, reject more than 99% of the electrons keeping more than 45% of the interacting antiprotons in the rigidity range 1.2-4.0 GV/c.

The dependence on the rigidity of the electrons is also expressed via the energy loss in the silicon strip with maximum detected energy. In the case of electromagnetic showers, this energy is due to secondaries electrons and positrons that cross this strip, each losing energy of the order of 1 mip. Thus the maximum detected energy in mip is of the same order of the number of charged secondaries at the shower maximum ($\sim$ 30 for a shower induced by 2 GeV electron) and so related with the rigidity of the incoming electron. For interacting antiprotons the spread of the maximum energy loss is much larger than for electrons and the detected energy can be of the order of hundreds of mip (e.g. breaking of a silicon nucleus with fragments that lose all their energies in one strip). Consequently, interacting antiprotons are selected when a large value of the maximum detected energy is found in one strip.

9.4.4 Longitudinal profile

The longitudinal profile of an electromagnetic shower is well defined and can be explicitly related to the energy of the incoming particle. The position of the shower maximum is logarithmic dependent on the energy of the electron and for electrons of less than 10 GeV it is well contained in the CAPRICE calorimeter. This position, expressed in terms of the calorimeter plane can be used to identify electromagnetic showers. In fact, an hadronic shower is usually made up by several types of particles: minimum ionizing particles; neutral pions that decays in photons and induce electromagnetic showers; neutrons; and slow particles. This implies a highly non-uniform longitudinal distribution of the shower and a nearly random distribution of the shower maximum in the calorimeter. Thus the two type of shower can be separated accordingly to the longitudinal location of the maximum detected energy.

Figure 9.4 shows another parameter related to the longitudinal profile of the shower: the fraction of the total energy that is detected in the two planes with maximum energy losses for a) antiprotons and b) electrons. This fraction is peaked around 0.45 with small tails for electrons while the distribution is broader for interacting antiprotons. The hatched areas in Figure 9.4 indicate the fraction of interacting antiprotons ($\sim 14\%$) and electrons ($\sim 0.1\%$) surviving a cut based on this variable in the rigidity range 1.2-4.0 GV/c. The cut is logarithmic dependent on the particle rigidity measured in the tracking system.

Also the difference between the detected energy in the x view and in the y view of the calorimeter is used in the antiproton selection. For electrons the two measurements are highly correlated and nearly always the same while for antiprotons the interactions can result in detectable differences between the two sets of silicon detectors (e.g. slow secondary particles that cross only one silicon detector).

9.4.5 Transversal profile

For electromagnetic showers the typical transversal width of the shower is given in terms of the "Molière radius" (R_M) [55] and 95% of the energy of the shower is contained in a cylinder of radius:

$$R(95\%) \ \sim \ 2\,R_M \tag{9.1}$$

For the CAPRICE calorimeter, $2R_M$ corresponds to around 1.38 cm, i.e. 4 strips. This implies that the largest part of the energy lost by the electromagnetic shower will be detected along the track of the incoming electrons. In contrast, for an hadronic shower 95% of the

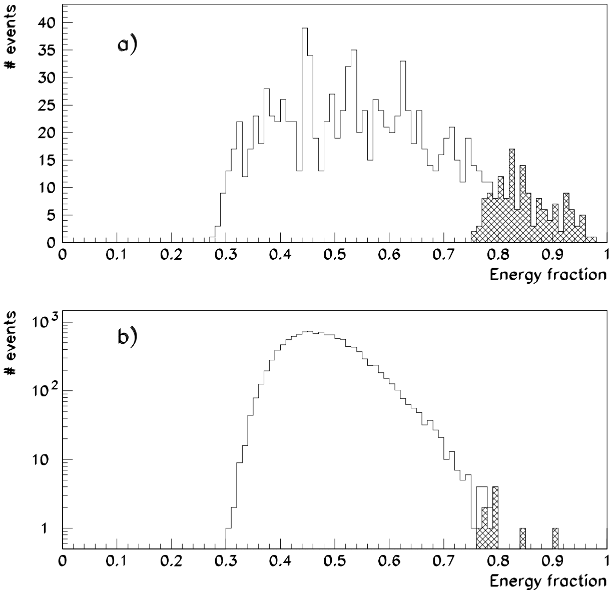

Figure 9.4: *The fraction of total energy detected in the two planes with maximum energy losses for events without tagged second shower. a) antiprotons, b) electrons. Notice the logarithmic scale for electron distribution. The hatched areas are the events surviving an antiproton cut based on this variable.*

energy is contained in a cylinder of one interaction length radius corresponding to nearly 10 cm for this calorimeter. In this antiproton analysis four parameters are used to characterize the transversal profile:

- The fraction of energy lost outside $4R_M$
- The fraction of energy lost inside $1R_M$

These two variables are different, even if correlated, because they use the fact that the transversal profile of the electromagnetic shower is made by two components. First, one central component, narrow (less than $1R_M$ of width) and very collimated along the track, due to the high energy secondaries not affected by the multiple scattering.

Second, a lateral component, more spread along the track, due to the scattered low energy secondaries. The cuts on these variables are chosen logarithmic dependent on the particle rigidity.

- Figure 9.5 shows the distribution of another variable: the fraction of total energy losses detected outside an area defined along the track for a) antiprotons and b) electrons. This area is defined as the cluster [2] of energy closest to the track for the first half and the second half of the calorimeter. The two clusters are obtained merging the detected energies of the first four and of the second four planes of the calorimeter respectively. In this way, differently from the previous two variables, the transversal fluctuations of the electromagnetic shower are minimized. The difference in the two distributions is clearly seen. The hatched areas indicate the events surviving the antiproton cut, based on this variable logarithmic dependent on the particle rigidity. The cut rejects $\sim$ 99.5% of the electrons keeping $\sim$ 26% of the interacting antiprotons in the rigidity range 1.2-4.0 GV/c.
- The transversal profile of electromagnetic showers is highly symmetrical with respect to the tracks of the inducing electrons while the same it is not true for hadronic showers. This asymmetry is used in the antiproton selection requiring that the positions of the center of gravity of the clusters defined for the previous variable have to be several millimeters away from the track.

9.4.6 Topological development of the shower

For the previous variables, the energy distribution of the showers in the calorimeter has been used. However, the fine segmentation of the silicon detectors enables a more detailed analysis of the development of the shower.

The simplest description is based on the number of strips hit in the calorimeter. A cut, logarithmic dependent on the rigidity of the particle, based on this variable permits to separate non-interacting antiprotons, or interacting antiprotons with a low multiplicity, from electrons as shown in Figure 7.5.

The distribution of a more complex variable, that represents the development of the shower, is shown in Figure 9.6. This variable is

---

[2] A cluster is obtained grouping sequential strips hit.

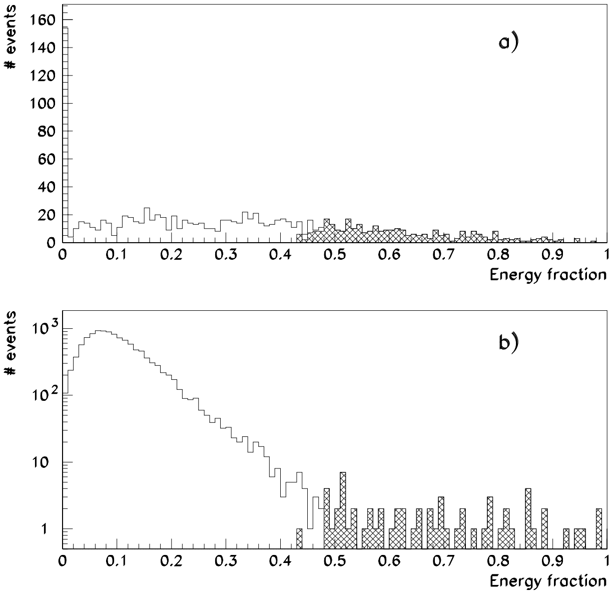

Figure 9.5: *Fraction of the total energy losses in the calorimeter detected outside an area defined along the track for: a) antiprotons, b) electrons. Only events without a second shower are shown. Notice the logarithmic scale for the electron distribution. The hatched areas are the events surviving an antiproton cut based on this variable.*

calculated as:

$$\sum_{j=1}^{2}\sum_{i=1}^{8} n_{hit}(i,j)\cdot i \tag{9.2}$$

with $n_{hit}(i,j)$ as the number of strips hit inside four R_M around the track in the i-th plane (1 for the top plane and 8 for the bottom plane) of the j-th view. In this way, the typical multiplication of secondaries of the electromagnetic shower is enhanced resulting in large values of the variable as seen in Figure 9.6. While for an hadronic shower, the transversal dispersion and the limited number of secondaries usually results in lower values of this variable. The solid lines indicate the cut for antiproton selection based on this variable and a good separation

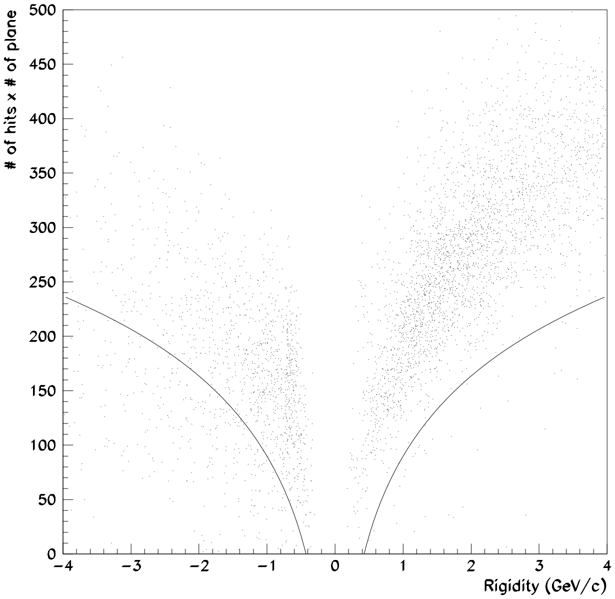

Figure 9.6: *The topological development of the shower. The sum of the number of hits inside 4 R_M around the track multiplied by the corresponding calorimeter plane versus rigidity. Only events identified with a second shower are shown. For clarity the electrons have been given positive charge. The solid line indicates the cut for antiproton selection based on this variable.*

between the two particles is obtained: the cut rejects 99% of the electrons with an efficiency of 36% for interacting antiprotons in the rigidity range 1.2-4.0 GV/c. In the antiproton analysis, this cut is applied only for events identified with a second shower.

A more direct selection of the antiproton showers is obtained looking for annihilation stars. This is performed looking for the interaction point and counting the number and energy of single charged tracks exiting from it.

9.4.7 Starting point of the shower

Another interesting feature of the electromagnetic shower is its starting point. This depends only on the number of radiation lengths crossed by the electron and not on its energy (for electrons with energy greater than 1 GeV). This means that roughly 63% of the electrons start showering after one plane (one X_0) and about 86% after two planes. For high energy hadrons, one interaction length in tungsten is around 27 X_0. Hence, each plane of the CAPRICE calorimeter has nearly the same probability of being the starting point of an hadronic shower. This is not completely true for hadrons (above all antiprotons) at low energies (below few GeV) where the inelastic cross section is strongly momentum dependent. This obliges to define energy dependent cuts even though it would not be necessary for electron or positron selection.

Figure 9.7 shows the distribution of a variable related to the starting point of the shower for a) antiprotons and b) electrons. This variable is calculated as:

$$\sum_{j=1}^{2}\sum_{i=1}^{8}\theta_{ij}\cdot i \tag{9.3}$$

with $\theta_{ij} = 1$ if the i-th plane of the j-th view has a strip along the track (less than 4 mm away) with a detected energy typical of a (anti)proton otherwise $\theta_{ij} = 0$. A non-interacting antiproton or an antiproton interacting after a few planes will result in high values of this variable. For a non-interacting particle with hits in all the planes this variable will have the maximum value of 72. Instead, for an electron or an interacting particle showering in the first planes, these parameters will assume low values. The hatched areas in Figure 9.7 indicate the fraction of interacting antiprotons ($\sim 46\%$) and electrons ($\sim 0.09\%$) surviving the antiproton selection based on this cut in the rigidity range 1.2-4.0 GV/c.

The starting point of the shower is also characterized by the average (total detected energy along the track divided by the number of strips hit) energy loss in the first half of the calorimeter that becomes a pre-shower calorimeter. This variable permits to emphasize the larger fluctuations of the energy losses of the first part of the hadronic shower.

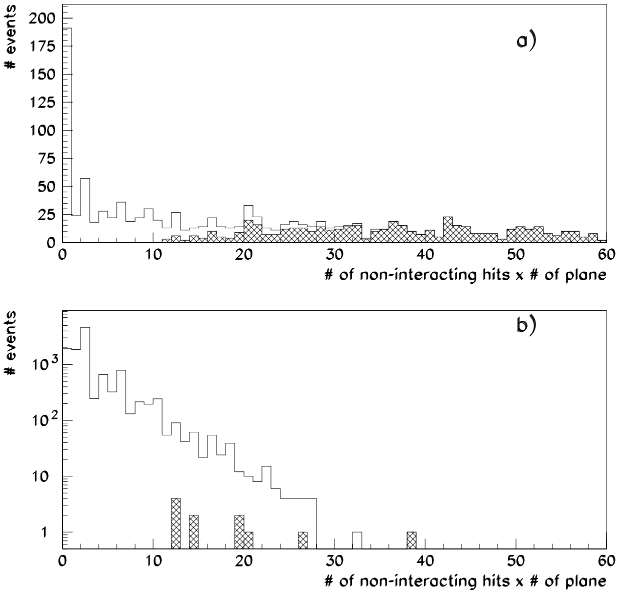

Figure 9.7: *Distribution of a variable related to the starting point of the shower for: a) antiprotons , b) electrons. Events without tagged second shower are shown. The y-axis for the electron distribution is a logarithmic scale. The hatched areas show the events surviving an antiproton selection based on this variable.*

9.4.8 Contamination from e^- in the calorimeter $\overline{\mathrm{p}}$ selection

The calorimeter (anti)proton selection is performed defining antiprotons all the events satisfying at least one of the cuts based on the parameters described above. In Table 9.1 the performance of the calorimeter selection on a simulated electron sample is presented.

As a cross check, the same calorimeter cuts are applied on a sample of 976 electrons from flight data. The electrons are selected in the rigidity range 1.2 to 4 GV/c with the condition of having more than 22 strips hit in the calorimeter and with a Cherenkov angle equal to a $\beta \sim 1$ particle in the RICH. With this condition, only

Rigidity GV/c	e^-	selected as not e^-	Surviving fraction %
1.2-2.8	14063	305	(2.2 ± 0.1)
2.8-4.0	3226	128	(4.0 ± 0.3)
1.2-4.0	17289	433	(2.5 ± 0.1)

Table 9.1: *Simulated electron rejection of the calorimeter selection. The table shows the number of simulated electrons and the number of events selected as not electrons.*

$\beta \sim 1$ particles interacting in the calorimeter are selected. Of these, 39 events survive giving a fraction of 4.0 ± 0.6%. The experimental sample does not only include electrons but also interacting negative pions. A visual inspection shows that of the 39 events at least 12 are interacting pions resulting in a surviving fraction of 2.8 ± 0.5%, in good agreement with the simulated result.

It is worth noticing that, in this rigidity range, the calorimeter cannot separate muons from non interacting antiprotons and cannot, therefore, be used to reject muons and non interacting pions.

9.5 RICH Selection Criteria

As pointed out before, the RICH is the primary instrument for identifying antiprotons in a background of electrons, muons and pions. For the RICH to be able to identify particles, the Cherenkov angle must be correctly determined. Therefore, a set of cuts must be applied on the RICH data.

9.5.1 Basic cuts on the RICH data

The basic cuts on the RICH data are:

- there must to be a good agreement in the impact position between the RICH and tracking, both in x and y direction;
- only one charged particle should have traversed the RICH, i.e. there should be no pile-up pad.

The distribution of the difference in the impact position measured by the RICH and tracking is rigidity dependent, but the variation is small above 1 GV/c. At 1 GV/c the resolution is about 0.19 cm and at 4 GV/c it has decreased to 0.15 cm, as shown in Figure 9.8. As described in section 8.1, the obtained resolution is comparable to the expected value taking into account the pad size and how many pads that are used for the calculation. The cut on the difference in position is set to be less than three times the resolution, typically $<$ 5 mm.

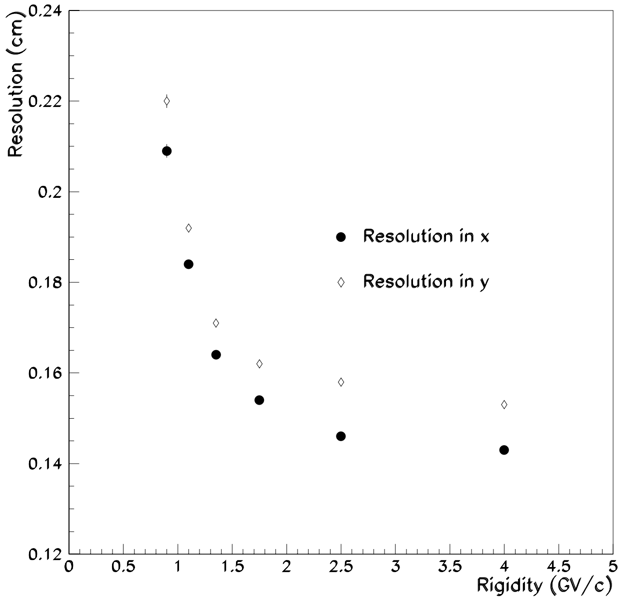

Figure 9.8: *Resolution of the difference in impact position measured by the RICH and tracking, (•) are for the resolution in x and (◊) for the resolution in y.*

A pile-up pad is defined as a pad located outside the ionization area with a signal level above the so called saturation limit of the pre-amplifier, see section 8.1. With this cut, events with more than one particle traversing the RICH are rejected.

These are the basic cuts on the RICH data which must be fulfilled. There are however additional cuts that must be put on the RICH to ensure that the measured Cherenkov angle is correct.

9.5.2 Cuts on the Cherenkov angle

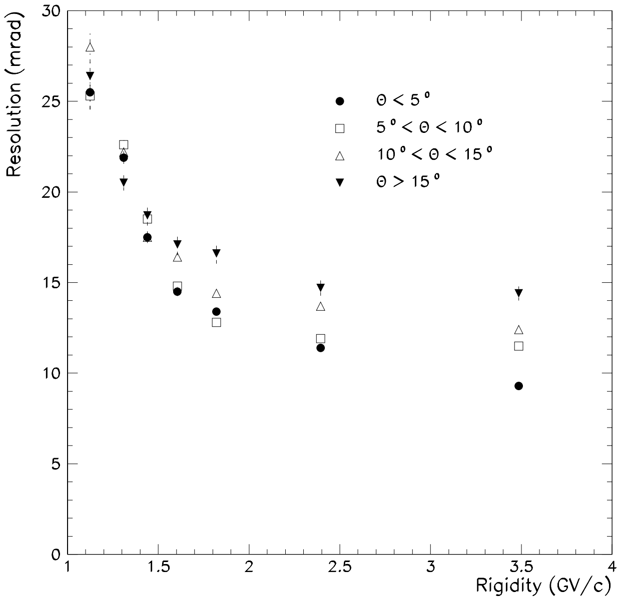

Figure 9.9: *Resolution of the Cherenkov angle for protons versus rigidity for four different ranges of the incidence angle* (θ)*.*

The basic parameter determined by the RICH is the Cherenkov angle (θ_c). The quality of the measured Cherenkov angle depends on the number of pads used in the fit (n_{eff}). If the number of pads is too low, then the Cherenkov angle might not be correct. This is especially important close to the border of the pad plane where the Cherenkov light is not fully contained inside the pad plane. Therefore, a cut on the number of pads used in the fit must be imposed. This cut is chosen as:

- there must be at least eight pads used in the Cherenkov angle calculation:
  $n_{eff} > 8$.

The choice is a a compromise between maximization of the detection efficiency and minimization of the contamination.

For a particle to be identified as an antiproton, two additional requirements must be fulfilled:

- the measured Cherenkov angle must agree within three standard deviations of the resolution from the expected Cherenkov angle for a (anti)proton:
  $|\theta_{c,measured} - \theta^{p}_{c,expected}| < 3 \times \sigma_{\theta_c}$;
- the measured Cherenkov angle must be at least 30 mrad less then the expected Cherenkov angle for a pion:
  $\theta^{\pi}_{c,expected} - \theta_{c,measured} > 30$ mrad, "the 30 mrad cut".

The resolution[3] of the Cherenkov angle is determined from a large proton sample. This sample is divided, with respect to the incidence angle, into four bins and in each bin the resolution is derived as a function of rigidity. Both the incidence angle and rigidity is given by the tracking. The best resolution is found for small incidence angles and high rigidities, see Figure 9.9. The resolution is used for the definition of the antiproton Cherenkov angle cut. The limits of the cut is set to three times the resolution for a given incidence angle and rigidity.

For muons and electrons there is a difference compared to protons because for rigidities above 1 GV/c they are both $\beta \sim 1$ particles. In this case the resolution depends only on incidence angle, see Figure 9.10. For the definition of the cut against muons and electrons, a fixed value is used given by the average resolution, found to be around 10 mrad, and the cut is set to three times this value and hence called the "30 mrad cut".

The reason to introduce this cut is that when the rigidity is higher than 2.8 GV/c the upper limit on the cut on Cherenkov angle for the

---

[3] The resolution is estimated by fitting a Gaussian curve to the distribution of the difference between the measured and expected Cherenkov angle. The expected angle is calculated using the measured value of the rigidity.

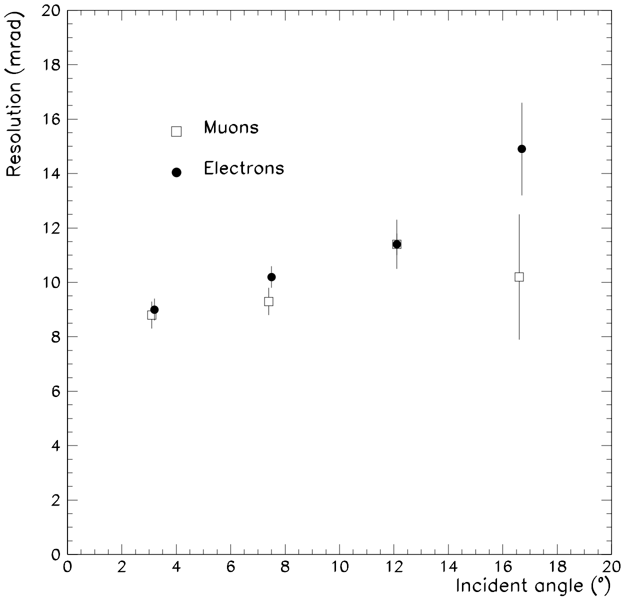

Figure 9.10: *Resolution of the Cherenkov angle versus incidence angle for muons and electrons with a rigidity larger than 1.2 GV/c.*

(anti)protons is getting close to the lower tail of the distribution of the resolution of the $\beta \sim 1$ particles. Therefore, the cut is applied so the measured Cherenkov angle must be separated with more than 30 mrad from the expected Cherenkov angle of a pion. This is illustrated in Figure 9.11 where the expected Cherenkov angle for protons and pions are plotted together with the resolution in the Cherenkov angle for protons and the "30 mrad cut". The reason to compare with pions is that the pion is the heaviest background particle, and hence has a smaller Cherenkov angle than an electron or muon for a given rigidity. This choice therefore strengthens the cut.

The rigidity range where the RICH clearly can identify anti-protons is 1.2-4.0 GV/c and it is divided in two bins. The lower limit at 1.2 GV/c is given by the threshold of the RICH, below this rigidity no Cherenkov light is emitted for a (anti)proton. The division at 2.8 GV/c is given by the overlap between the pion and proton Cherenkov angle distributions. Finally, above 4 GV/c the RICH is not any longer able to separate protons against $\beta \sim 1$ particles (shown in Figure 9.11).

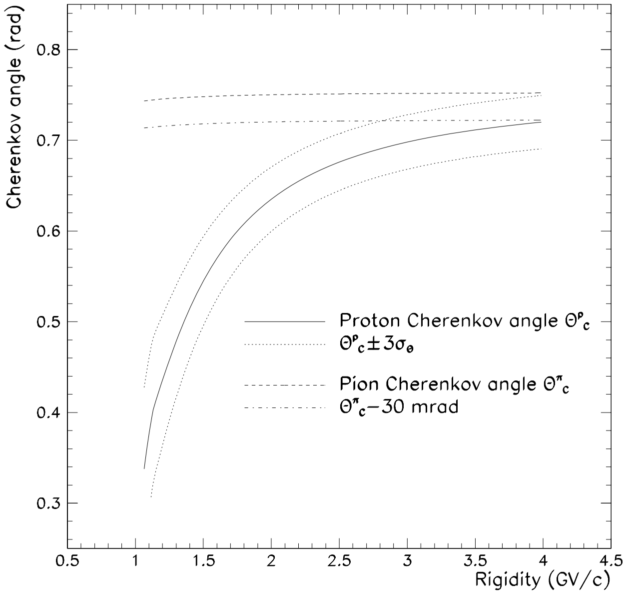

Figure 9.11: *The expected Cherenkov angle for protons (solid line) plotted together with ± three times the resolution for incidence angles between 5 and 10° (dots), showing the definition of the cut put on the Cherenkov angle to identify (anti)protons. The dashed line shows the expected Cherenkov angle for pions together with the ”30 mrad cut”.*

9.5.3 Number of pads used for the Cherenkov angle calculation

The number of pads used for the Cherenkov angle determination is a trade-off with the RICH detection efficiency. To study this protons, electrons and muons are used.

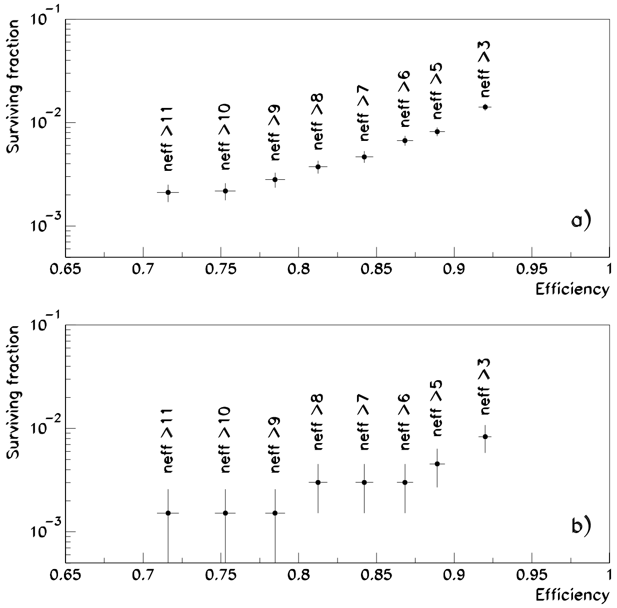

Figure 9.12: *The surviving fraction versus proton selection efficiency of the RICH for different* n_{eff} *cuts. a) muons b) electrons.*

A clean sample of protons is selected from the flight data using the tracking, dE/dx and calorimeter in the rigidity range 1.8 to 2.3 GV/c where the efficiency of the RICH is approximately constant.

A sample of electrons is selected from the flight data using the calorimeter in the rigidity range 1.2-4 GV/c. In this rigidity range the calorimeter is able to select a very pure electron sample with high efficiency.

For the muons, instead, ground data are used. Before the flight long runs were performed at ground collecting more than 400000 events. These events are mainly muons with a small fraction (less than 10%) of protons and a smaller number of electrons and pions. Selecting non interacting particles in the calorimeter with negative curvature using the tracking and dE/dx (anti)proton criteria in the rigidity range 1.2 to 4.0 GV/c, a clean sample of negative muons/pions is obtained.

The use of electrons and muons for this study is justified by two facts:

- in the rigidity range 1.2-4 GV/c the RICH detection efficiency for electrons and muons is rigidity independent;
- electrons and muons are the two main sources of contamination for the antiproton selection.

Figure 9.12 shows the rejection versus detection efficiency for the Cherenkov angle cut for different values of the cut on n_{eff} obtained using: a) protons and electrons; b) protons and muons. From the figure it results that a cut at eight (n_{eff} >8) is a good compromise between rejection factor and selection efficiency. It can be noticed that a good agreement of the rejections is obtained between electrons and muons. This is a clear indication that the behaviour of the RICH, regarding the detection efficiency, was constant from the ground runs to the flight. Furthermore, it indicates that the RICH detection efficiency for muons and electrons is similar.

It is worth noticing that the RICH detection efficiency is position dependent. As already pointed out, close to the border of the pad plane, the Cherenkov light is not fully contained, resulting in a lower number of pads that can be used in the fit. Closer to the centre of the pad plane, the number of pads hit by Cherenkov photons increases and, consequently, the resolution improves. This can be clearly seen in Figure 9.13. Figure 9.13 a) shows the proton Cherenkov angle selection efficiency (●) for a cut of n_{eff} >8 as function of the distance from the RICH borders. Protons are selected in the rigidity range 1.8-2.3 GV/c and the effective area of the pad plane (51.2×51.2 cm^2) is decreased in steps of one pad (0.8 cm) from each side. The detection efficiency reaches a plateau for a central region, defined as 13 pads from the border, i.e. when the effective area is reduced to 30.4×30.4 cm^2. As a matter of fact, two plateaux are identified in the efficiency and both are related to the incidence angle of the particle and to the radius of the Cherenkov ring. For a $\beta \sim 1$ particle at 0° incidence angle, the ring radius is around 5.5 cm. The first plateau is found for borders larger than 6 cm and it corresponds to the full containment of the Cherenkov light for particles with small

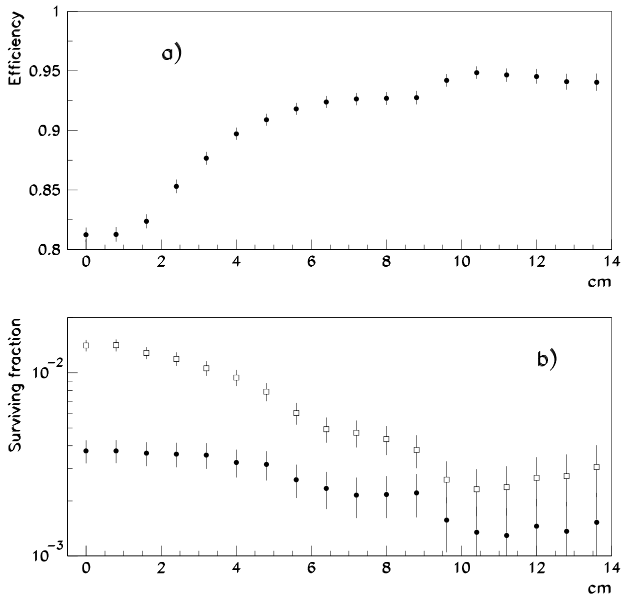

Figure 9.13: *a) The proton Cherenkov angle selection efficiency (●) for a cut of* $n_{eff} > 8$ *as function of the distance from the RICH borders. b) The fraction of muons selected* $\overline{\mathrm{p}}$ *by the RICH as function of the distance from the RICH borders for:* □ $n_{eff} > 3$ *and* ● $n_{eff} > 8$*.*

incidence angles, $< 5°$. The second plateau at 10 cm is found related to particles with incidence angle greater than[4] 10°.

Figure 9.13 b) shows the fraction of muons selected as antiprotons by the RICH as a function of the distance from the RICH borders for two n_{eff} cuts: ● $n_{eff} > 8$; □ $n_{eff} > 3$ (ground muon data). The surviving fraction of the former is smaller than the latter but the difference between the two fractions decreases towards the centre. This is used in the proton flux analysis where the background is not a main problem in contrary to the antiproton analysis. For that analysis, a cut at eight is used only for the border region while a cut

---

[4] 10° is the average of the distribution of the incidence angles in the CAPRICE data.

a three is used for the central region. As already stated, the central region is defined as the effective pad area of 30.4×30.4 cm^2, 10.4 cm away from each border. However, it has to be stressed that in the antiproton analysis the same RICH cuts are used both for the proton and antiproton selection, i.e. $n_{eff} > 8$

9.5.4 Contamination from e^- in the RICH $\overline{\mathrm{p}}$ selection

From the flight data, a clean sample of electrons is selected in the rigidity range 1.2 to 4.0 GV/c with the calorimeter and dE/dx in the scintillators. This sample is used to study the rejection capability of the RICH.

Applying the RICH criteria described in the previous sections on the electron sample, the fraction of surviving electrons is found and presented in Table 9.2 for the two rigidity bins of the antiproton analysis. Defining electrons as events with a non minimum ionizing behaviour in the calorimeter, 1388 electrons are selected between 1.2 and 4 GV/c in the flight data with a small background of interacting pions. An electron contamination from 4.2 ± 2.1 events in the antiproton sample after RICH antiproton selection, but before the calorimeter selection, is estimated.

Rigidity GV/c	Events identified as e^- by the RICH	Events identified as $\overline{p}$ by the RICH	Surviving fraction (%)
1.2-2.8	1052	2	0.19 ± 0.13
2.8-4.0	271	2	0.74 ± 0.52

Table 9.2: *Surviving fraction of electrons in the RICH. The table shows the number of electrons identified as antiprotons by the RICH.*

9.5.5 Contamination from μ^- in the RICH $\overline{\mathrm{p}}$ selection

The muon contamination is harder to estimate directly because it is not possible to select a clean sample (without antiproton contamination) with the calorimeter from flight data. Therefore two methods are used. First it is shown that muons have the same detection efficiency as electrons in the RICH and therefore it is assumed that the muon contamination is equal to the electron contamination. Second, the muon contamination is obtained using the ground data.

A muon contamination is estimated from the number of muons having a Cherenkov angle more than 30 mrad below the expected pion Cherenkov angle. In order not to include any real antiprotons in the sample, this has to be limited to a smaller rigidity bin, 1.2-2 GV/c, and only events with a Cherenkov angle not more than 70 mrad below the expected pion Cherenkov angle are used in the analysis. This defines a region of the Cherenkov angle, $30 < \theta_c^\pi - \theta_c < 70$ mrad, that roughly corresponds to the region in which an antiproton is accepted in the highest rigidity bin. With these criteria, three muons remain out of 260 corresponding to a fraction of $(1.2 \pm 0.7)\%$. This value is in agreement with the fraction found for the second bin in the electron sample, see Table 9.2. Furthermore, performing the same selection on the electrons, that is selecting events with the $30< \theta_c^\pi - \theta_c <70$ mrad cut, six events out of 701 satisfy the condition resulting in a fraction of $(0.9 \pm 0.3)\%$. Also this value is in agreement with the muon estimation and, therefore, it is reasonable to assume that the muon contamination is the same as the electron contamination.

From the ground data a sample of 12 819 events with negative curvature are selected using the tracking, dE/dx and calorimeter (anti)proton criteria in the rigidity range 1.2 to 4.0 GV/c. On these events, the RICH selection is applied and the results are presented in Table 9.3. These values are in good agreement with the values obtained by the electrons from flight data (Table 9.2) and it can safely be assumed that the performance of the RICH is the same during the ground runs as during the flight.

Since the ground muon contamination is a better estimation (larger sample and, consequently, smaller errors) of the muon conta-

Rigidity GV/c	Events identified as μ^- by the RICH	Events identified as $\overline{p}$ by the RICH	Surviving fraction (%)
1.2-2.8	8983	21	0.23 ± 0.05
2.8-4.0	3836	26	0.68 ± 0.13

Table 9.3: *The table shows the number of ground muons selected as antiprotons by the RICH.*

mination, the values of Table 9.3 are used to define the background from the negative muons and pions in the antiproton signal.

9.6 The Antiproton Sample

When applying the combined selection of the RICH, scintillators, tracking system and calorimeter, nine antiprotons are identified. Figure 9.14 shows the Cherenkov angle as a function of rigidity for negative and positive particles. On the negative side the nine antiprotons (squares) are plotted together with the background of negative events remaining after all cuts, except the cut on the Cherenkov angle, have been applied. The background consists mainly of muons and pions, and 2.5% of the electrons that passed the calorimeter selection. As shown in the figure, there is a clear separations between the antiprotons and the background up to 3 GV/c when the Cherenkov angles start to approach each other. The measured Cherenkov angles are well distributed around the expected value.

Of the nine antiprotons, two are found interacting (more than 22 strips hit) in the calorimeter. This is agreement with the simulated expectation of 3.4 ± 1.1 antiprotons interacting on the calorimeter. Note that not all antiproton interactions give a detectable signal in the calorimeter.

9.6.1 Contamination in the antiproton sample

Table 9.4 summarizes the contamination in the antiproton sample as estimated from the electron and muon contamination analysis.

The muon contamination is calculated from Table 9.3 and from the number of events selected during the flight with a minimum ionizing behaviour in the calorimeter.

Rigidity bin at the spectrometer GV/c	Electrons:		Muons:	
	Before RICH and calorimeter selection	Expected number of fake antiprotons	Before RICH and calorimeter selection	Expected number of fake antiprotons
1.2 - 2.0	1098	0.07 ± 0.02	387	0.9 ± 0.2
2.8 - 4.0	290	0.07 ± 0.02	99	0.7 ± 0.1

Table 9.4: *Muon and electron contamination in the antiproton sample.*

The electron contamination is given by the combined calorimeter and RICH selection. The electron rejection power of the calorimeter is studied using simulated data and summarized in Table 9.1. Then, defining electrons as all negative events with a non minimum ionizing behaviour in the calorimeter, 1388 electrons are identified between 1.2 and 4 GV/c in the flight data resulting in an electron contamination in the whole antiproton sample of less than 0.15 electrons.

9.6.2 Conclusions

A negligible electron contamination is found in the antiproton sample. The muon (and pion) contamination is estimated (see Table 9.4) and subtracted from the antiproton signal resulting in the following number of identified antiprotons: 3.1 (+3.1,-1.9) between 1.2 and 2.8 GV/c and 4.3 (+3.4,-2.2) between 2.8 and 4 GV/c. The error on the observed numbers are given by Poissonian statistics, corresponding to a 68% confidence interval.

Applying the same selection criteria on a positive deflection sample, protons are instead selected. In the first bin, between 1.2 and 2.8 GV/c, 124658 protons are selected and between 2.8 and 4 GV/c, 25260 protons are selected.

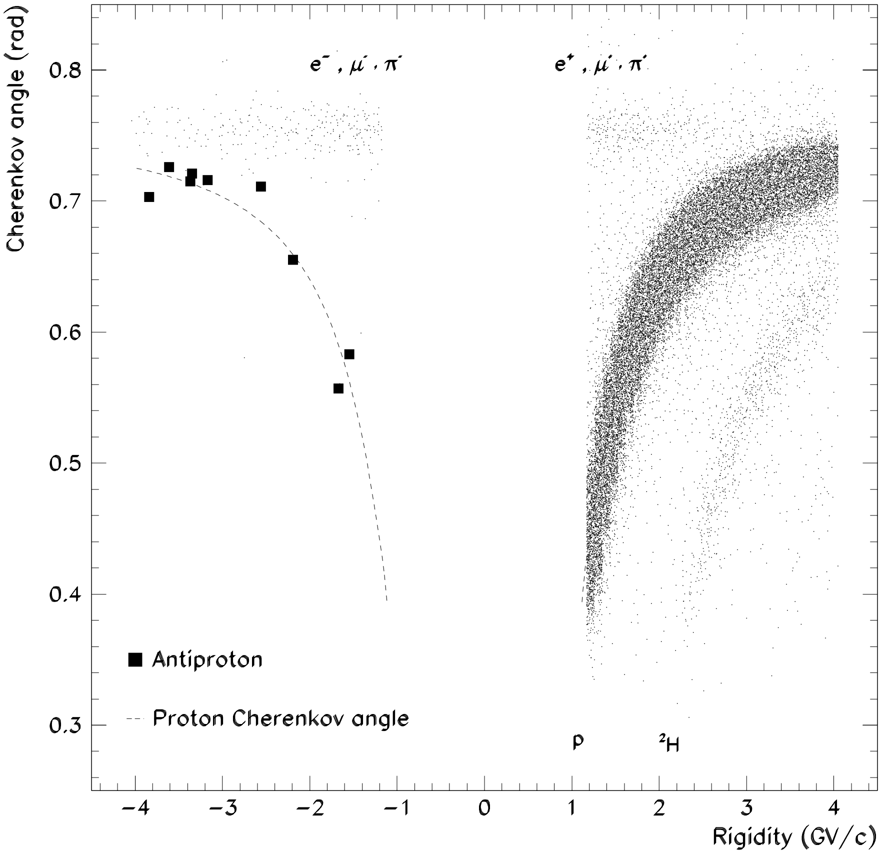

Figure 9.14: *The distribution of the Cherenkov angle as a function of rigidity for negative and positive particles. There are 404 negative and* $\sim$ *160000 positive (*$\sim$ *150000 protons) events selected. The squares show the nine antiprotons.*

Chapter 10

Efficiency of the Antiproton and Proton Selection

It is assumed that protons and antiprotons behave the same in the detectors except for inelastic interactions. Therefore the efficiency for both protons and antiprotons are derived from a proton samples. The only exception is the calorimeter where the antiproton efficiency is estimated from simulations. In general, the different interaction cross sections are taken into account by the corrections applied on the selected number of protons and antiprotons, and not by the efficiencies.

10.1 Efficiency of the Tracking System

The efficiency of the tracking system is defined as the fraction of single track events surviving the request of good track reconstruction in the system. The problem with finding the efficiency is how is a track defined good before the track reconstruction is done. In principle the efficiency of the drift chambers (DC) and multiwire proportional chambers (MWPC) could be checked using samples of particles selected with the other detector. However, it is difficult to find the true efficiencies with this method because of the correlation between the DC and MWPC in the fitting procedure. Instead, a unique capability of the CAPRICE instrument is used to select single charged tracks without involving any of the tracking devices. The feature comes from that both the RICH and calorimeter are imaging devices. The imaging capability of the RICH is useful to reject multiparticle events and the calorimeter is able to reconstruct tracks. In addition of the RICH and calorimeter, the scintillators are also used to select a cleaner sample.

10.1.1 Single track proton selection

The raw data recorded during the flight contain many events with more than one particle traversing the spectrometer at the same time. These events are generated by showers in the atmosphere above the gondola or in the gondola itself. For these events, it is not possible to reconstruct a single track and they should not be a part of the sample. The purpose of the single track proton selection is to remove as many as possible of these multiple particle events. For this selection, a set of cuts are implemented on the scintillators and the RICH.

The cuts on the scintillators data are very similar to what is used for the selection of protons and antiprotons:

- only one paddle hit in the top and bottom scintillator plane;
- remove albedo particles, i.e. ToF ≥ 0.

Still there could be multiple particle events passing these cuts if the particles go through the same paddles.

The RICH is also used in a similar way as for the selection of antiprotons and protons:

- the RICH is hit, i.e. at least one anode wire with a signal significantly above noise;
- only one pad with a saturated signal;
- limited number of pads with signals generated by the ionization, the number of ionization pads: $4 \leq \mathrm{n}_{ionpads} \leq 12$.

When applying the above selection criteria on the raw data, roughly 75% of the events are rejected. What is left are those events with clean hits in the scintillators and with signals in the RICH as expected from a single traversing particle.

However, the tracking system efficiency can be energy dependent. In fact assuming that the scattering process is the main cause of the inefficiency a rigidity dependence is expected. Therefore, it is necessary to define a sample of protons of known energy. This selection is performed using the ToF, the calorimeter and the RICH information.

10.1.2 Selection with ToF and dE/dX

The time-of-flight system can be used independently of the tracking system. In fact, even if some corrections of the pulse height or for the timewalk are not possible without using the track information, the performance of the system only degrades slightly without them and not in a significant way for this application.

The selection of protons is performed using the dE/dx scintillator information. This selection has to include the β-dependence of the dE/dx. In order to derive the β it is however necessary to know the flight path of the particle and this is usually obtained from the tracking fit. Without the track reconstruction a straight track approximation has to be used. The path length of the particle is then assumed to be the distance between the impact positions in the scintillators. These positions are obtained by the intersection of a straight line, connecting the impact points in the RICH and in the calorimeter, with the paddles. The impact point in the RICH is given by the ionization pads and in the calorimeter by the hits in the first silicon plane. Using this distance, the β of the particle is calculated.

The β-dependence is found in the same way as is described in the time-of-flight chapter, i.e. by fitting the peak position of the distribution of the ADC signal. The same method is used for both top and bottom scintillators and a match of the dE/dx in both of them is required for the selection.

The time-of-flight measurement does not only provide the β. By assuming a mass, the rigidity of the particle can be obtained. The rigidity determined in this way is called ToF-rigidity. The resolution in ToF-rigidity is limited by the time resolution of the ToF. The expected resolution has not been explicitly calculated, instead it has been checked against the rigidity from the tracking. It is found that this method can be used up to roughly 3 GV/c. The relative resolution of the ToF-rigidity is shown in Figure 10.1.

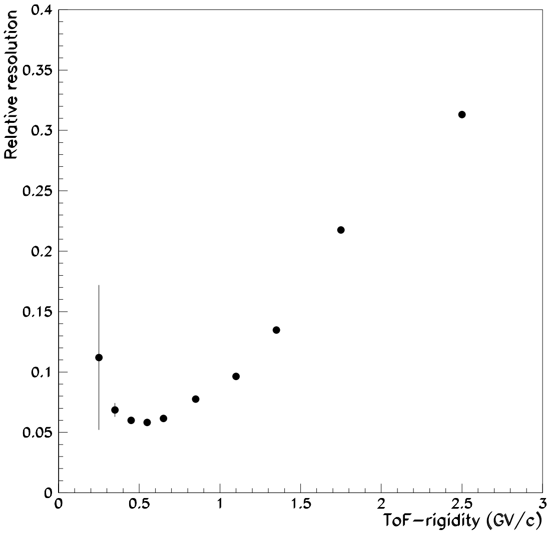

Figure 10.1: *The relative resolution of the ToF-rigidity for protons.*

10.1.3 dE/dx selection of protons below 0.7 GV/c

Protons below 0.7 GV/c are selected requiring a match in the dE/dx. The method works well for rigidities where the energy loss of a proton is different from a minimum ionizing particle. For rigidities higher than 0.7 GV/c, the signal in the scintillators becomes similar to a minimum ionizing particle. This causes a problem since there are events, triggered by showers, with two different particles crossing the scintillator planes: one crossing the top scintillator and another the bottom one. These particles are, to a large fraction, minimum ionizing and they can easily match the dE/dx cuts in both scintillators. On the other hand, the probability that two non minimum ionizing particles cross the scintillators both having approximately the same β is very small.

In conclusion, the dE/dx method works very well for rigidities below 0.7 GV/c. Above that level, protons have to be selected together with another technique.

10.1.4 Selection of protons above 0.7 GV/c

For higher rigidities, it is necessary to define an additional condition to select only single tracks. This can be done requiring that the events are contained in the tracking volume. The containment implies that the positions in each detector should coincide with those given by a track extrapolation done without the tracking devices.

For this purpose, the routine which extrapolates the track is used. The extrapolation routine needs start values and normally they are given as a result of the track fit. These values are: the x and y position and the three direction angles in the bottom MWPC plus the deflection. From these start values, the retrack routine calculates the trajectory of the particle taking the magnetic field into account. Here, the start values are provided by the calorimeter and the ToF. The calorimeter is sampling the energy loss in eight layers (in both x and y). From these positions, a straight line fit of the track is made. The precision is not as good as from the tracking devices due to shorter lever arm and less resolution in each point, but sufficient for this purpose. From this fit, the positions and direction angles in the bottom MWPC are calculated. The deflection is provided by the time-of-flight rigidity with the assumption that the particle is a proton.

When the start values are determined, the prediction of the retrack routine is checked against the prediction by each detector. This is done for the scintillators (in x) and in the RICH (both in x and y). The resolution of this method is compared to using the normal track fitting in Table 10.1.

A particle is regarded as being contained in the tracking volume if the position given by the retrack method agrees with the measured position in all detectors. The agreement should be within three standard deviations.

Detector	Resolution in position (cm)	
	Calorimeter tracking	Regular tracking
Bottom scint. x	2.4	2.4
Top scint. x	4.7	2.6
RICH y	3.8	0.16
RICH x	4.3	0.15

Table 10.1: *Resolution of position matches in the ToF and the RICH using calorimeter tracking and regular tracking.*

10.1.5 Removing deuterons

A dE/dx selection as a function of β still leaves a contamination in the proton sample coming from deuterons of the same β. The deuterons can however be removed using the calorimeter. Even though protons and deuterons have the same β, the deuterons have twice the kinetic energy due to their higher mass ($m_D \simeq 2 \times m_p$). The higher kinetic energy implies that the deuterons lose proportionally less energy than the protons when passing through the same amount of matter and hence decrease their β less. Before reaching the first layer of silicon detectors in the calorimeter, the particles cross 2 cm of plexiglass. Therefore, a proton and a deuteron, which had the same β in the scintillators, will not any longer have the same β when reaching the silicon detectors. The proton will have decreased its β more than the deuteron and so its detected energy in the silicon will be larger. This process is true for all the eight silicon planes making it possible to achieve a proton-deuteron separation up to 0.8 GV/c (when calculating the rigidity from the β).

The detected energy in the first layer of the calorimeter as a function of ToF-rigidity is shown in Figure 10.2 a. In the figure, the two bands coming from protons and deuterons are seen. Figure 10.2 b presents the distribution for protons and deuterons obtained with a simulation. A good agreement is found with the experimental distribution and between the rigidity/momentum positions of the proton Bragg peaks: 0.38 GV/c for the experimental data, compared to 0.36 GeV/c for the simulation. (It should be pointed out that for

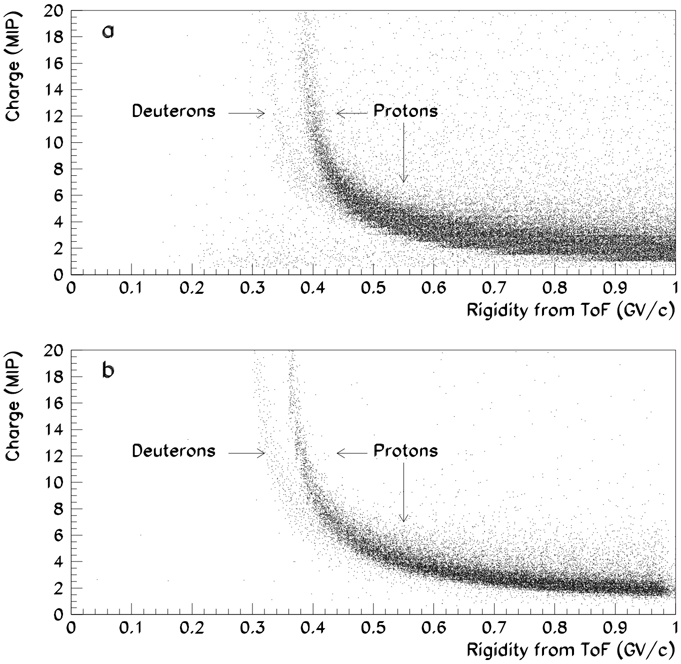

Figure 10.2: *Detected energy in the first layer of the calorimeter as a function of the ToF-rigidity: : a) experimental data; b) simulated data.*

the simulated deuterons the momentum has been divided by two for the comparison). The good agreement, a difference of only 20 MeV/c, which can be due to an uncertainty in the simulated geometry, confirms the validity of the ToF procedure for the rigidity extrapolation.

The RICH is also used to clean the proton sample. Protons with rigidities less than 1 GV/c are below the threshold for Cherenkov light. The selection criteria includes a cut on the number of pads used for the calculation of the Cherenkov angle ($n_{eff} \leq 3.5$). This cut is only used below 0.7 GV/c.

10.1.6 Calculation of the tracking efficiency

The efficiency of the tracking system is determined for the standard tracking cuts, used for both analysis of protons and antiprotons. It is obtained for rigidities from 0.2 GV/c up to 3 GV/c and is presented in Figure 10.3. As expected, the efficiency reaches a plateau[1] for rigidities $\geq$ 1.8 GV/c and it drops significantly for lower rigidities. Above 3 GV/c a different technique is used:

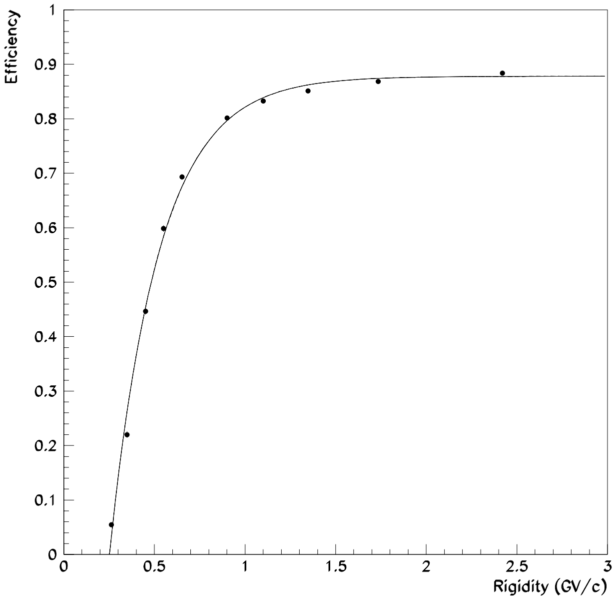

Figure 10.3: *Tracking cuts efficiency for protons as a function of ToF-rigidity. The solid line is a fit to guide the eye.*

1. select a sample of protons with the conditions described in the previous section;

---

[1] A plateau is defined where the efficiency varies with less than 1%

2. require that the track fit routine converge [2], hereinafter called "fit O.K.";
3. apply the rest of the basic tracking cuts.

The resulting efficiency is clearly biased by the fit O.K. condition but it is reasonable to assume that this bias is constant above 1 GV/c. The efficiency between 0.2 and 3 GV/c is compared to the values of Figure 10.3 and a normalization factor is obtained. In this way the tracking efficiency can be estimated up to 20 GV/c (above 20 GV/c it is assumed constant).

10.1.7 Drift chamber efficiency

As a cross check of the technique used in the previous section, the tracking system is separated into its two components: the multiwire proportional chambers and the drift chambers. The efficiency of the drift chamber cuts (the cuts are presented in section 12.3) is obtained using the same method applied for the overall efficiency and a different method employing the usage of the MWPC. Then the two results are compared.

With the MWPC, single charged tracks are selected requiring that the fit routine, when using only the MWPC data, converges. In this way also the rigidity of the particles is obtained. Then, out of the single charged track sample, a proton sample is selected matching the top and bottom dE/dx of the scintillators.

The efficiencies obtained using the two methods are presented in Figure 10.4. The results are in good agreement. A difference of $\leq$ 2% is found, above all at high rigidities ($>$ 1 GV/c). This difference can be due both to a contamination of double track events in the sample from the first method and to a too cleaned sample, regarding the scattering in the tracking volume, for the MWPC method. To further clean the sample used for the first method, it is required that at least one MWPC in the top, one in the middle and one in the bottom x+y stack have a "good time sum"[3]. This enables to reject events where a second particle crosses only the tracking system

---

[2] For the fit to converge, there must be at least four hits in x and three in y.

[3] The time sum is given by the delay line readout of the MWPCs

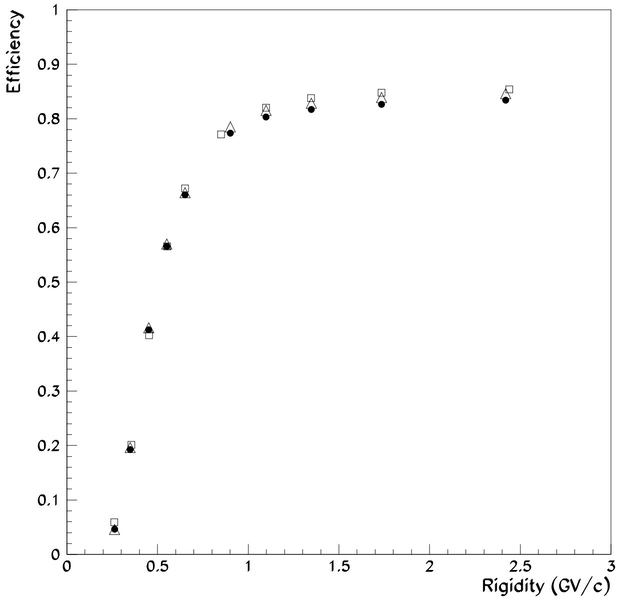

Figure 10.4: *Drift chamber tracking cuts efficiency for: □ protons selected with MWPC method as a function of MWPC fitted rigidity; • protons selected with RICH, calorimeter and ToF as a function of ToF rigidity; △ protons selected with RICH, calorimeter, ToF and good time sums of the MWPC as a function of ToF rigidity.*

volume. The resulting efficiency (△) is presented in Figure 10.4. A good agreement is found with the first method (•) for rigidities lower than 0.8 GV/c while the efficiency has an intermediate value between the first two methods at greater rigidities. This indicates that the sample selected with the condition of fit reconstruction in the MWPC is biased having reduced the number of scattered tracks in the sample. However, it cannot be inferred that the true efficiency is this last one because the condition on the good time sums of the MWPC could also bias the sample. In fact, this requirement is connected with the efficiency of the MWPC and this could be related with the number of MWPC used in the fit and, so, with the tracking cuts.

10.1.8 Conclusion

From the discussion in the previous section, it is clear that it is difficult to estimate how much a sample is biased. Hence, to avoid to use any tracking information for the efficiency, it is decided to use the efficiency obtained with the first method. However, to take care of uncertainties, a systematic error of 1% is assumed for rigidities greater than 0.7 GV/c. The values of the efficiency for the basic tracking cuts are obtained interpolating these experimental efficiencies.

The study of the DC and MWPC systems separately has shown that the drop in the efficiency for protons at low rigidities is mainly due to the drift chambers. The cause of this inefficiency of the drift chambers is a combination of a software problem, the tracking routines are optimized for low deflection particles, and that the large ionization in the drift gas induces noise in the chambers.

10.1.9 Efficiency of the additional tracking criteria

The efficiency is also determined for the additional cuts on the tracking data, i.e. the cuts applied to reject scattered particles (see section 9.1.2). It is derived by applying the additional criteria to an already fitted sample. The ratio between the surviving events and original events is the efficiency. This results in a linear rigidity dependent efficiency:

$$\text{Efficiency} = A - B \cdot R \tag{10.1}$$

where R is the rigidity in GV/c, A and B are fitted parameters and the following values are found: A=0.857±0.004, B=0.009±0.002. For the final numbers, the error matrix is used. The efficiency for the complete tracking criteria is obtained multiplying the efficiency of the additional tracking cuts to the efficiency of the basic tracking cuts, and is shown in Figure 10.6 (dotted line).

10.2 Efficiency of the Time-of-flight System

The efficiency of the time-of-flight system is checked using a proton sample selected with emphasis on minimizing the background of positrons, muons and heavier particles. For the selection the following criteria are used:

- The tracking:
  same cuts as for the antiproton analysis, see section 9.1;
- The RICH:
  the basic cuts as described in the section 9.5.1 and, for rigidities above 1.2 GV/c, a Cherenkov angle as expected for a proton;
- The calorimeter:
  a cut to select non-interacting particles, plus a cut on the mass reconstructed from the rigidity and detected energy, see section 12.1.3.

With the combination of these cuts, the contamination in the proton sample is found to be less than 0.1%.

On this sample the cuts on the top scintillator and ToF, as described in section 9.3.1, are applied. It is found that the cut on ToF>0 has an efficiency close to 100%. The efficiency of the single paddle cut is also close to 100% whereas the cut on the dE/dx is lower. The combined efficiency for these cuts as function of rigidity is shown in Figure 10.5. The decrease in the efficiency with increasing rigidity is due to that a larger fraction of the protons lose energy above the dE/dx cut (increased probability of delta ray production). This effect becomes constant for rigidities higher than 3 GV/c. The errors in the points are dominated by the systematic error coming from a small shift in the gain of the photomultipliers during the flight. The shift is mainly due to the change in the temperature during the flight. The systematic error is estimated from the difference in efficiency between two parts of the flight data, one in the beginning of the flight when the temperature was low and one when the temperature was higher. The error is found constant to 0.38%. This value is used for the data presented in Figure 10.5.

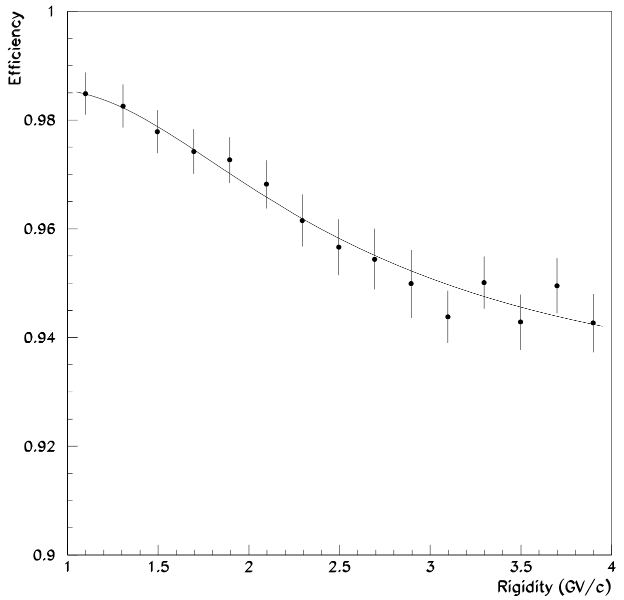

Figure 10.5: *The proton selection efficiency for the top scintillator. The errors include both the statistic and systematic errors.*

A fit to the efficiency (solid line in Figure 10.5) is made using the following function:

$$\text{Efficiency} \;=\; A\,(1 - B\,exp(-C \cdot \beta^{-1.84})) \qquad (10.2)$$

where are A, B, C are fitted parameters. The β-dependence is derived in Chapter 6.
The following values are found: A=0.986±1.71·10^{-3}, B=23.5±4.01, C=5.95±0.166. Note that the fitted parameters are correlated and for the final numbers, the error matrix is used. The fitted function of the efficiency is used for both the antiproton and the proton corrections in the rigidity range 1.2-4.0 GV/c.

10.3 Efficiency of the Calorimeter

With the calorimeter, non-interacting particles are clearly identified as not electrons, while the main ambiguity arises from separation between hadronic interactions and electromagnetic showers. At these energies (1.2 to 4.0 GV/c in rigidity), the inelastic cross section of antiprotons is very different from protons. Hence, the calorimeter selection results in a different efficiency for interacting antiprotons compared to interacting protons. This implies that it is not possible to use, for the calorimeter antiproton efficiency, the experimental calorimeter selection efficiency obtained using a sample of protons. Instead the antiproton efficiency is obtained from a Monte Carlo simulation. For the non-interacting antiprotons and non-interacting protons, the same efficiency is obtained.

The results from simulations show that the detection efficiency for antiprotons with the calorimeter is rigidity dependent and can be expressed by the following function:

$$\text{Efficiency} \;=\; A\,(1 - Bexp(-C \cdot R)) \tag{10.3}$$

where R is the rigidity (GV/c), A, B and C fitted parameters with the following values: A=0.991±6.6·10^{-3}, B=0.42±7.5·10^{-2}, C=0.96±0.15. Note that the fitted parameters are correlated and for the final numbers, the error matrix is used. The dashed line in Figure 10.6 shows the calorimeter antiproton selection efficiency. As a cross-check, results of the simulations for interacting protons are compared with the efficiency of an experimental, interacting[4] proton sample in the range 1.2-4 GV/c and a good agreement is found: (90.3 ± 0.9)% with the simulation compared to (92.2 ± 0.5)% with the experimental data.

The proton calorimeter detection efficiency is obtained from an experimental proton sample selected by RICH, dE/dx and time-of-flight and is found to be (99.21 ± 0.03)% independent of rigidity in this range.

---

[4] All the protons, selected with the RICH, with more than 22 strips hit in the calorimeter are defined as interacting.

10.4 Efficiency of the RICH

In order to get a good estimation of the RICH selection efficiency, a clean proton sample is necessary. When starting from a positive deflection sample, a background of positrons, muons and heavier particles like deuterons and alphas must be removed. This is done by using both dE/dx from scintillators and the calorimeter.

The remaining muon contamination in the sample is presented in Table 12.1 and 12.2. When combining the two selections, less than 5% of the muons survive below 1.0 GV/c increasing to 20% in the bin 1.0-1.5 GV/c. This is not a large problem due to the fact the protons are so much more abundant, there are at least a factor 10^3 more protons than muons. The positrons are rejected with high efficiency by the calorimeter and like for the muons, the proton to positron ratio is of the order 10^3 giving a negligible contamination.

However, the deuteron background is too large to be ignored. From previous experiments, e.g. IMAX [62], the deuteron to proton ratio is measured to be 0.023 ± 0.014 at 2.5 GV/c. The ratio is rigidity dependent but this value is a good indicator on how large the background is. Using a sample without removing the deuterons or knowing the fraction would result in an underestimation of the proton efficiency because the RICH is able to separate deuterons from protons in the rigidity range 1.2 to 4.0 GV/c.

With the combination of the dE/dx cut on the scintillators and calorimeter the deuterons are removed completely up 1.5 GV/c. In the bin 1.5-3.0 GV/c the contamination is still low due to the calorimeter cuts, as shown in Table 12.2. Above 3 GV/c, the calorimeter cut has a low efficiency and does not any longer clean the sample from deuterons. Instead, an indirect method is used to first estimate the deuteron contamination, then subtract the contamination from the proton sample before calculating the efficiency. The estimation is done by using the RICH to identify the deuterons in the range 3.0-4.0 GV/c using the Cherenkov angle. Particles are selected as deuterons if the measured Cherenkov angle is within 30 mrad from the expected angle of a deuteron. However, in order to get the subtraction correct the efficiency of the selection must also be known. This is not possible to do using the deuterons themselves because it is impossible to select a clean sample without the RICH in this rigidity range. Instead, the efficiency is determined by selecting a proton sample in the same β range as the deuterons and calculating the efficiency of these protons for the RICH. The justification for this argument comes from the fact that the RICH is a β-sensitive detector and a 3 GV/c deuteron is expected to behave as a 1.5 GV/c proton. Following this argument, protons are selected in the range 1.5-2.0 GV/c and from this sample the efficiency is determined to be 73.7 ± 0.3%. This value can be used as the deuteron efficiency between 3.0 and 4.0 GV/c. The efficiency is assumed to be constant in the bin. The next step is to use the number of deuterons in the bin 3.0-4.0 GV/c found by the RICH and rescale this number by the efficiency. This value is then subtracted from the proton sample.

The resulting antiproton efficiency is shown in Figure 10.6 (solid line). It is shown that the efficiency is close to zero when the rigidity is 1 GV/c which is the threshold for a proton to produce Cherenkov light. For increasing rigidity, more Cherenkov photons are produced and the efficiency increases. For rigidities between 1.5 and 2.8 GV/c the efficiency is constant about 70% and then starts to decrease. The decrease is due to the "30 mrad cut" (see section 9.5.2).

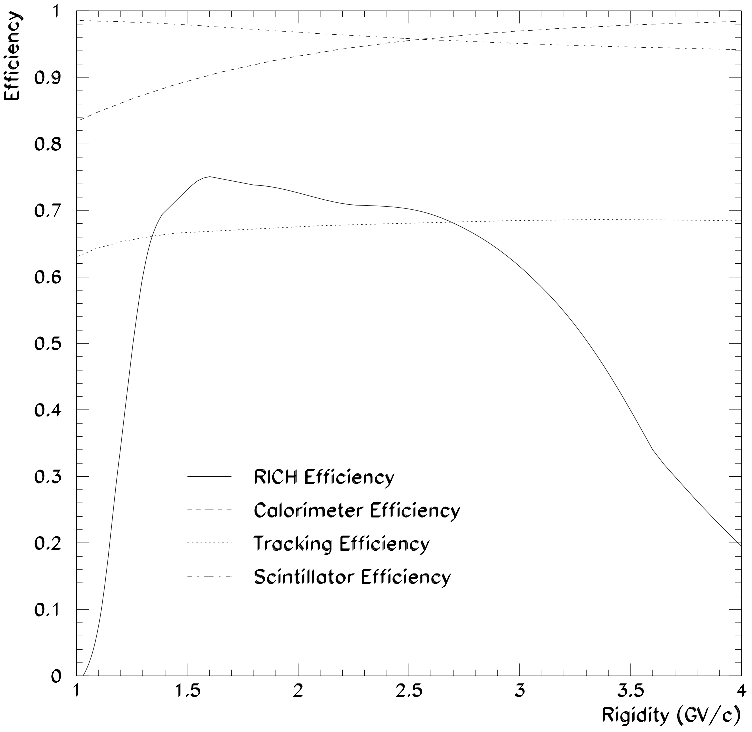

Figure 10.6: *The proton selection efficiency versus rigidity for: the RICH (solid line), the tracking system (dotted line), the calorimeter (dashed line) and the scintillator dE/dx cut (dashed-dotted line).*

Chapter 11

The Antiproton Flux and the Antiproton to Proton Ratio

The calculation of the antiproton flux and the antiproton to proton ratio is done in several steps, starting with the observed number of antiprotons and protons. First, the selection efficiencies are taken into account. Next, is to correct for production and losses in the payload. In this sample, a background coming from particles produced in the atmosphere is present. After this background is subtracted, the correction for losses in atmosphere is applied. Then, finally, the antiproton flux and the ratio at top of atmosphere is determined.

11.1 Selected Numbers of Antiprotons and Protons

The result of the selection of antiprotons, with the estimated background subtracted, and protons is presented in Table 11.1. The errors are given by Poissonian statistics, corresponding to a 68% confidence interval.

Rigidity GV/c	Number of antiprotons	Number of protons
1.2-2.8	$3.9^{+3.2}_{-1.9}$	$(1.247\pm0.003)\cdot10^5$
2.8-4.0	$4.3^{+3.4}_{-2.2}$	$(2.53\pm0.02)\cdot10^4$

Table 11.1: *The number of selected antiprotons, with the estimated background subtracted, and protons.*

11.2 Theoretical Fluxes and Solar Modulation

For the subsequent calculations of the various corrections, it is important to have theoretical predictions of both the primary flux at the top at the atmosphere and the flux of particles produced in the atmosphere. The primary fluxes are used to calculate the centre of each bin for the efficiency determination, and, of course, also for comparison with the final results. The atmospheric fluxes are used for background subtraction. To properly treat the corrections, the solar modulation must be taken into account. It is also used when comparing the resulting fluxes with measurements by other experiment made during different solar activity.

11.2.1 Primary and atmospheric proton fluxes

The flux of cosmic ray particles has been measured by a large number of balloon-borne experiments. These experiments have been carried out with an increasing precision and over an expanding region in energy. They have in common that the measurements are typically done at an atmospheric depth of 3 to 6 g/cm^2. At this depth, the atmospheric component is not negligible and it is important that the correction is done in a proper way. For the correction of the atmospheric protons, a theoretical calculation of Papini et al. [63] is used. That work has also been used for the atmospheric correction by other experiments, e.g. [58], [59] and [64] .

In the paper by Papini et al. [63], a compilation of measurements on the fluxes of protons, alphas and heavier elements, like oxygen and carbon, is presented. These measurements are done with balloon-borne experiments and cover a wide range in energy, from around 10 MeV up to 1000 GeV. At periods of high solar activity the flux of protons below 1 GeV is suppressed with as much as an order of magnitude. The measurements are divided in two categories, one for flights made during periods of low solar activity and one for flights during periods of high activity. For each category, the fluxes (J) are interpolated and fits are done using a minimum number of parameters by an expression like:

$$J(E) = A\,(E + B)^{-\alpha}\,E^{\beta}\;(particles/m^2\,sr\,s\,GeV/n) \qquad (11.1)$$

where E is the kinetic energy in GeV per nucleon and A, B, α and β are the fitted parameters. For the proton flux, the following values are found for minimum solar modulation: A=$1.8{\cdot}10^4$, B=0.92, α=4.0 and β=1.25; and for maximum solar modulation: A=$1.8{\cdot}10^4$, B=1.61, α=3.83 and β=1.0. (Parameters are given without errors in [63].)

For the theoretical calculation of the atmospheric protons, the primary fluxes presented above are used. The processes taken into account are, for relativistic energies, inelastic scattering of the primary protons and spallation of heavier nuclei in the overlying atmosphere. At lower energies, protons are also produced from recoil of target nucleons. In addition, protons are produced by evaporation of target nuclei during interactions of primary cosmic rays at all energies. The fluxes are calculated by solving simultaneously the transport equations for the atmospheric protons together with those for primary protons, secondary neutrons and heavier nuclei.

The resulting atmospheric fluxes are presented at different depths. All fluxes are calculated for both minimum and maximum activity. In the paper by Papini et al. the results are tabulated for 3, 5 and 10 g/cm^2 for energies between 20 MeV and 40 GeV. Figure 11.1 a) shows the atmospheric fluxes during solar minimum activity at 3, 5 and 10 g/cm^2.

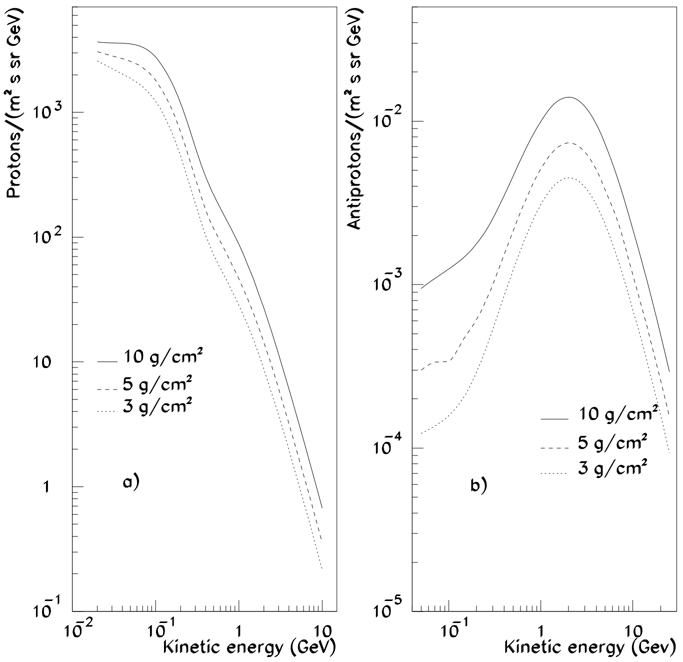

Figure 11.1: *The flux of a) atmospheric protons [63], and b) antiprotons [65] during minimum solar activity. The solid line is at 10 g/cm^2, the dashed line at 5 g/cm^2 and the dotted line at 3 g/cm^2 of residual atmosphere.*

11.2.2 Interstellar and atmospheric antiproton fluxes

For the interstellar antiproton flux the work of Gaisser and Schaeffer [24] is used. Their calculation is done in a general way that it holds both in a disk-halo diffusion model [25] as well as in the standard leaky box model [10]. The calculation includes a new treatment of the processes involved in the production of antiprotons from interactions. Compared to previously published calculations, they have also included the production of antiprotons by nuclei in the interstellar matter. The nucleus component is small but, as they show, not negligible. They have also reexamined the normalization and shape of the primary spectrum and the path-length parameter (λ_{esc}).

The resulting interstellar flux is in better agreement with observations than previous calculations. However, there is a large systematic uncertainty in their calculation. The systematic uncertainty is discussed in section 11.6 where the CAPRICE antiproton flux is compared with their predictions.

When the work of Papini et al. [63] is used for proton corrections, it is a natural choice to use the work of Stephens [65] for the correction of the atmospheric antiprotons because his calculations are based on the same proton fluxes. In [65] Stephens presents a calculation of the antiproton spectrum in the atmosphere from interactions of cosmic rays with the air nuclei. His calculations yield a higher production compared to his previous result [66], especially below 1 GeV, since the Fermi motion of the target nuclei is taken into account. At 200 MeV the production is 3 times higher whereas above 1 GeV the difference is of the order of a few percent. The energy spectrum of antiprotons is determined as a function of the atmospheric depth by taking into account the energy loss processes. In the paper by Stephens [65], the fluxes are tabulated for 3, 5 and 10 g/cm^2 for energies between 50 MeV and 200 GeV for both minimum and maximum activity. Figure 11.1 b) shows the secondary fluxes during solar minimum activity at 3, 5 and 10 g/cm^2.

11.2.3 Solar modulation

When the interstellar cosmic rays enter the solar system they interact with the solar wind. The solar wind is generated by the sun's corona and can be described as a flow of plasma out from the sun. The plasma consists of charged particles, mainly electrons and protons, carrying trapped magnetic fields along with it. The speed of the solar wind at 1 AU is about 700 km/s [67]. But the solar wind does not stop here, in fact it reaches much further out in the solar system and is extended beyond Pluto.

During the interactions, the particles lose energy in a process described with the so-called force-field approximation [68]. In this model of the solar modulation, the energy loss is a combination of convection, diffusion and adiabatic processes. When a particle propagates from the interstellar medium to the Earth's atmosphere, the mean energy loss can be characterized with a single parameter (Φ). This parameter is referred to as the modulation parameter. With this parameter the modulated proton flux ($J_{mod}(E)$) at Earth (1 AU) is given by:

$$J_{mod}(E) = \frac{E^2 + 2m_pc^2E}{(E+\Phi)^2 + 2m_pc^2(E+\Phi)} J(E+\Phi) \tag{11.2}$$

where E is the kinetic energy in MeV, m_p is the mass of a proton and $J(E)$ in the interstellar flux.

The strength of the modulation depends on the activity of the sun which is strongly correlated with the number of neutrons detected at ground level. To study the activity of the sun, cosmic ray neutrons have been monitored for a long time (from IGY[1] and onward) at number of different locations, e.g. the Climax monitor in Colorado, USA. For general information about neutron monitors and Climax, see [69].

From the neutron monitors it is possible to derive the strength of the modulation. As Paradis showed in [70] there is a negative correlation between Φ and the neutron monitor counts. In his calculation, the modulation parameter was derived for seven different balloon flights and compared with the neutron monitor counts for each flight. For these flights, Φ varied from around 480 MeV during low solar activity, to 1180 MeV for a flight done with high solar activity. To fit the Φ parameter to the Climax neutron monitor counts, Paradis used a simple power law:

$$\Phi = A + exp(B + Cx) \tag{11.3}$$

where x is the number of counts (hourly average × 0.005) and Φ in MeV. Paradis found that: A=420±30; B=15±1; and C=(-5.2±0.8)$\cdot 10^{-3}$.

This fit and Climax data are used to estimate the modulation during the CAPRICE flight. Climax counted around 410 000 neutrons/hour during the flight (8-9 of August 1994), taken from [71], giving Φ=500 MeV.

---

[1] The International Geophysical Year (1956/1957).

11.3 Efficiency Corrections

The first corrections to apply is for the selection efficiencies. The selection criteria used for the antiprotons show a rigidity (energy) dependence. Hence, when applying the efficiency it is important to use the correct value for the energy in each bin. Due to the low statistics for antiprotons, it is not possible to split the range in smaller bins over which the efficiency can be assumed to be constant. The proton data, on the other hand, is split in 50 MeV wide bins.

Both for antiprotons and protons, the mean energy ($\overline{E}$) of a bin is derived with a weighting technique using theoretical fluxes J(E) in the following way:

$$\overline{E} = \frac{\int EJ(E)dE}{\int J(E)dE} \tag{11.4}$$

The mean energy of a bin is then used for the efficiency calculation except for the RICH. The efficiency of the RICH has so strong variation with rigidity that the mean efficiency ($\overline{\varepsilon}$) is obtained directly with weighting technique similar to equation 11.4:

$$\overline{\varepsilon} = \frac{\int \varepsilon(E)J(E)dE}{\int J(E)dE} \tag{11.5}$$

For the theoretical flux of antiprotons, the interstellar flux ($J(E)$) given by Gaisser and Schaeffer [24] is used. This flux is modulated with a solar modulation parameter $\Phi = 500$ MeV. For the protons, J(E) is the primary proton flux taken from the Papini et al. paper [63].

The resulting efficiencies for the antiprotons are presented in Table 11.2. For the protons, the number of particles in each 50 MeV bin is counted and the efficiency for that bin is applied. For the tables in the following sections, the proton data is then grouped together and presented for the same bins as the antiprotons. However, the correction in each step is applied on the smaller bins.

The number of protons and antiprotons at the top of the spectrometer[2] is the measured flux corrected for selection efficiencies but

---

[2] The top of the spectrometer is the position below the top scintillator paddle, above the tracking system.

Rigidity GV/c	Efficiency (%)			
	Tracking$_{\bar{p}}$	ToF$_{\bar{p}}$	RICH$_{\bar{p}}$	Calorimeter$_{\bar{p}}$
1.2-2.8	67.6 ± 0.4	96.2 ± 0.2	70.2 ± 1.0	93.9 ± 0.4
2.8-4.0	68.6 ± 0.5	94.0 ± 0.3	45.7 ± 1.0	97.7 ± 0.3

Table 11.2: *The efficiency of the antiproton selection for the two bins.*

not for losses due to interactions in the payload. The results are presented in Table 11.3. Note that these numbers include subtraction of the estimated contamination of muons and pions. There are no errors shown in the table for clarity but the errors are taken care of and included in the final numbers of the flux and ratio. The table also includes the payload corrections (assumed with small errors) and the resulting number at the top of the payload.

Rigidity	Top of the spectrometer		Payload corrections		Top of the payload	
GV/c	$\bar{p}$	p	$\bar{p}$	p	$\bar{p}$	p
1.2-2.8	7.21	272648	1.21	1.09	8.72	295710
2.8-4.0	15.0	82304	1.18	1.10	17.8	90171

Table 11.3: *The number of antiprotons and protons corrected for the selection efficiencies, the correction factors for losses in the payload and the number of antiprotons and protons at the top of the payload. For clarity, errors are not shown in the table.*

11.4 Payload Corrections

When the particles traverse the gondola, from the dome down to the level of spectrometer, they pass through some material. During the passage there is a probability that primary particles are lost in interactions. It is assumed that all antiprotons and protons interacting above the tracking system are rejected by the selection criteria imposed on the data. The number of particles lost are corrected for with multiplicative factors. The interaction probability is calculated using the information of the material (presented in Table 11.4).

Item	Material	Atomic number	Density (g/cm^3)	Thickness	
				(cm)	(g/cm^2)
Dome	Al	26.98	2.7	0.30	0.81
Gondola gas	N_2	14.01	1.25×10^{-3}	100	0.125
RICH cover	C	12.01	2.3	1.00	2.3
Crystal	NaF	21.18	2.7	1.00	2.7
Window	Quartz	21.65	2.3	0.50	1.15
Pad plane	Vetronite	14.7	2.0	0.30	0.60
Pad plane	Stesalite	14.7	2.0	0.15	0.30
Scintillator	Plastic	11.16	1.03	1.02	1.05
Total					9.0

Table 11.4: *Material of the payload above the tracking system.*

For the calculation, the interaction mean free path for protons in air is used scaled for the different materials of the payload. For the scaling the following relation [65] for the inelastic cross section is used:

$$\sigma_{pD} \;=\; 56.7\,(A_D^{1/3} - 0.25)^2\; mb \qquad (11.6)$$

where D is the target nucleus having the atomic number A_D. The parametrization for the interaction mean free path (λ^{int}_{p+Air}) given by Stephens [65] is used:

$$\lambda^{int}_{p+Air} = \frac{83\,(1.0 - 97.0\, exp(-7.8\, E))}{1.0 + 0.027\, log\,(E/200)}\,(g/cm^2)\;, E > 0.7\; GeV \qquad (11.7)$$

$$\lambda^{int}_{p+Air} = 4.38\,(E^{-4.8} + 21.0\, E^{-0.6})\,(g/cm^2)\;, E < 0.7\; GeV \qquad (11.8)$$

where E is the kinetic energy in GeV of the proton.

For antiprotons, the annihilation term is added. The annihilation mean free path is also given by Stephens [65] and written as:

$$\lambda^{anni}_{\overline{p}+Air} = \frac{70.5}{(E^{-0.438} - 0.0476)}\,(g/cm^2) \qquad (11.9)$$

where E is the kinetic energy in GeV of the antiproton.

The calculations are done for the mean energy of each bin looping over all material. From the resulting interaction length (λ_{tot}), the correction factor (F) is given by:

$$F = exp(\lambda_{tot}) \tag{11.10}$$

The resulting correction factors for number of antiprotons and protons are presented in Table 11.3. The next step is to correct for the particles produced in the atmosphere.

11.5 Atmospheric Antiproton and Proton Corrections

The correction for particles produced in the atmosphere is done for the protons using the flux by Papini et al. [63], and for the antiprotons the flux given by Stephens [65]. For the subtraction of secondary particles from the observations, the geometrical factor and live time of the experiment must be known.

11.5.1 Dead time and geometrical factor

The live time (T_{live}) is calculated by multiplying the effective exposure time with the fractional live time. The fractional live time is given by two scalers in the payload. The first scaler counts all the time and the second scaler counts only when the data acquisition system is not busy. The ratio between these two scalers is the fractional live time of the experiment. There is a software cut implemented in the data acquisition program to check if there are signals in tracking chambers: there must be at least a signal in one out of three MWPCs in the top part and one out of three MWPCs in the bottom part of the tracking system. If not, the event is not recorded. The efficiency of this cut is estimated to be over 99.5% from the individual chamber efficiencies. The fractional live time during the flight, taking the software cut into account, is found to be (26.9±0.06)%.

The data taking during the flight went on for approximately 23 hours at float altitude. Due to failure of one drift chamber the period with all the detectors working properly is limited to 17 hours (60520 s). This gives the following live time:

$$T_{live} = 60520 \times 0.269 = 16280 \pm 40 \ (s) \tag{11.11}$$

The geometrical factor is obtained using GEANT [60] to generate and trace particles through the spectrometer. The technique used follows what is suggested in [72]. The main steps in this technique are:

1. Define a large square placed above the payload and generate a flux of particles through it. The flux should be uniform over the whole surface (uniform in x and y position), in ϕ and in $\cos^2\theta$.
2. Trace the particles with GEANT through the spectrometer. In the description of the spectrometer, the geometry of all detectors are taken into account plus the magnetic field. However, no material is put in the description, only vacuum.
3. For particles crossing both top and bottom scintillators (the condition to generate a trigger), the direction and position at the height of the first tracking chamber (MWPC) is saved.
4. The information of the direction, position and rigidity from GEANT is used as input to the routine (used for the normal analysis) that tracks particles through the spectrometer. Events that miss any detector or cross the bar are thrown away and not used for the subsequent calculations.
5. Repeat step 1-4 for different rigidities.
6. The geometrical factor can now be calculated as:

$$\frac{\text{the number of events passing the criterion in 4.}}{\text{the total number of events generated}}$$
$$\times \text{the geometrical factor of the square } (\pi \times \text{ its area})$$

The resulting geometrical factor is presented in Table 11.5 and Figure 11.2. As seen in the figure, the variation is small in the range of the antiproton analysis.

Rigidity GV/c	Geometrical factor (cm^2sr)
1.2-2.8	179.1 ± 2.8
2.8-4.0	177.4 ± 2.8

Table 11.5: *The geometrical factor with the statistical error in the two rigidity bins as determined by the GEANT simulation.*

11.5.2 Atmospheric fluxes

Figure 11.1 shows in a) the flux of (atmospheric) protons, and in b) the flux of antiprotons in the atmosphere at depths of 3, 5 and 10 g/cm^2 during solar minimum activity, from [63] and [65]. To get the atmospheric fluxes during the CAPRICE flight, a simple power law is used to interpolate between 3 and 5 g/cm^2. The average flight altitude for CAPRICE correspond to 3.9 g/cm^2 of residual atmosphere. Futhermore, it is important to scale the proton flux used for the theoretical atmospheric calculations, both for antiprotons and protons. For the scaling, the measured proton flux of this experiment is used. The proton flux and the scaling factor are described in Chapter 12.

Table 11.6 shows the number of secondary antiprotons and protons produced in the atmosphere when taken the live time and the geometrical factor into account.

11.5.3 Atmospheric losses

The last step is to correct for the losses of protons and antiprotons in the atmosphere. This is done using the same cross sections as for the payload corrections. The flight altitude corresponds to a residual atmosphere of 3.9 g/cm^2 of air. The result of this calculation is presented in Table 11.6.

Finally, the number of antiprotons ($N_{\overline{p}}^{TOA}$) and protons (N_p^{TOA}) at the top of the atmosphere is calculated, as presented in Table 11.6.

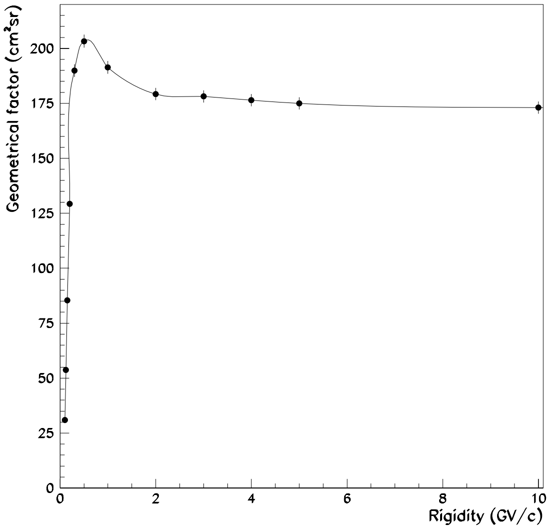

Figure 11.2: *The geometrical factor of the experiment as determined by the GEANT simulation.*

11.6 The Antiproton Flux and Antiproton to Proton Ratio

The antiproton flux at the top of the atmosphere is calculated from

$$\mathrm{Flux(E)} = \frac{1}{T_{live} \times G \times \Delta E} \times N_{\overline{p}}^{TOA}(E) \qquad (11.12)$$

where G is the geometrical factor, T_{live} is the live time, ΔE is the energy bin corrected to the top of the atmosphere, E the kinetic energy and $N_{\overline{p}}^{TOA}$ is the number of antiprotons at the top of the atmosphere. The resulting flux is presented in Table 11.7 and in Figure 11.3.

The dominating part of the errors of the CAPRICE measurement is of statistical nature due to the low number of antiproton events. There is also a systematic error coming from uncertainties in the contamination, efficiencies and secondary corrections. As described in

Rigidity	Atmospheric secondaries		Atmospheric corrections		Top of the atmosphere	
GV/c	$\overline{p}$	p	$\overline{p}$	p	$\overline{p}$	p
1.2-2.0	1.46	8447	1.09	1.04	$7.9^{+9.6}_{-5.9}$	$(2.98\pm0.04)\cdot10^{5}$
2.8-4.0	1.38	1663	1.08	1.04	$17.8^{+9.8}_{-15.1}$	$(9.2\pm0.2)\cdot10^{4}$

Table 11.6: *The first two columns show the estimation of the number of antiprotons and protons produced in atmosphere. Next two columns show the correction factors for losses in the atmosphere. No errors are shown but a 10% error is assigned to the theoretical atmospheric secondaries. Uncertainties on the live time and the geometrical factor are taken into account. The last two columns show the resulting number of antiprotons and protons at the top of the atmosphere.*

Kinetic energy (GeV)	$\overline{p}$-flux $(n/GeV\,m^2\,s\,sr)$	$\overline{p}/p$-ratio
0.6-2.0	1.9 (+2.4, -1.4) $\times10^{-2}$	2.7 (+3.3, -2.0) $\times10^{-5}$
2.0-3.2	5.3 (+4.5, -2.9) $\times10^{-2}$	1.9 (+1.6, -1.06) $\times10^{-4}$

Table 11.7: *The antiproton flux and antiproton to proton ratio.*

Chapter 9, the contaminations are carefully studied. The estimations are done on samples of particles selected by independent detectors, using data from the flight and ground runs before the flight, and not based on theoretical distributions. Futhermore, the efficiencies are equally well studied and, as the measured proton flux shows (see Chapter 12), taken care of in a proper way.

In Figure 11.3, the theoretical calculation by Gaisser and Schaeffer [24] of the interstellar antiproton flux modulated according to the conditions during the CAPRICE flight is shown with solid lines. In their calculation they assume a pure secondary production of antiprotons from of cosmic rays interacting with the interstellar medium. As shown, the CAPRICE measurement agrees well with the theoretical prediction of a pure secondary origin. The limits represents the uncertainties in the calculations. One error source is the uncertainty in the interstellar proton spectrum. To quantify the spectrum errors, they take the hardest spectrum γ=2.65 with the highest measured flux [73] and the softest γ=2.75 with the lowest measured [74]. Another part of the systematic error is coming from the uncertainty of the average path length of the cosmic rays in the galaxy. For the upper curve the path length given by Engelman et al. [75] is used and for the lower curve path length from Tan et al. [76] is used. In both cases, an extra error of 35% is assigned to the path lengths. In addition, an error of 10% is added for the uncertainty in the value of the antiproton production cross section.

It is difficult to draw any definite conclusions from the flux measurement alone. There are large errors on the CAPRICE measurements due to the limited statistics. In order to compare the CAPRICE results with other measurements, the antiproton to proton ratio is calculated. The ratio is less sensitive to the solar modulations than the flux measurement and hence makes it easier to compare different flights. The ratio is calculated as:

$$\mathrm{Ratio(E)} = N_{\overline{p}}^{TOA}(E)/N_{p}^{TOA}(E) \tag{11.13}$$

were E is the kinetic energy. The result is presented in Figure 11.4 and Table 11.7.

In the figure, the CAPRICE measurement (filled circles) is given together with other experiments and with a prediction of the ratio by [24]. This figure should be compared with Figure 1.2 where the experimental situation in 1990 is shown. The data in the figure are given by Golden (open cross) [18], MASS91 (open diamond) [59], IMAX (open squares) [58], BESS (open triangle) [64] and finally Buffington (filled star) [15].

The IMAX experiment used the same magnetic spectrometer as CAPRICE but with a completely different kind of particle identification. In the two lowest bins in energy, the antiprotons are identified with a time-of-flight technique, using two aerogel Cherenkov counters as veto against leptons and mesons. In the highest bin, the Cherenkov counters were used for the identification. The IMAX and CAPRICE experiments are in many respects comparable, but one

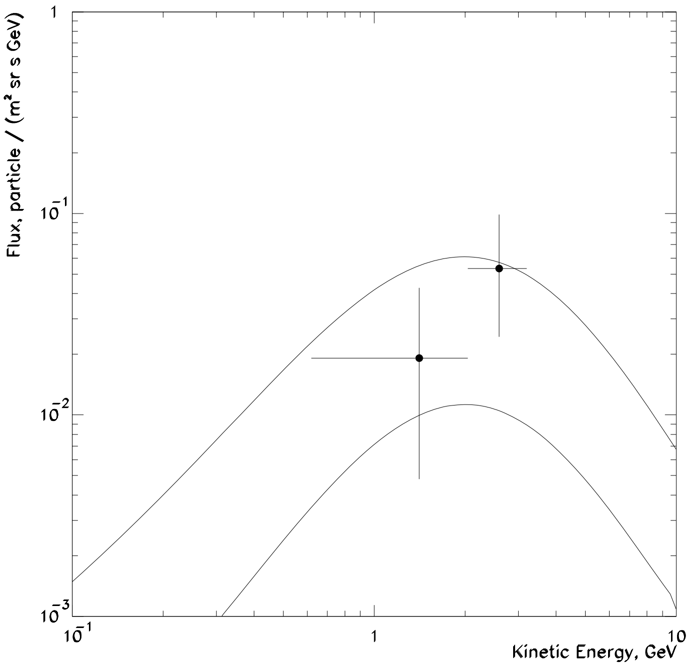

Figure 11.3: *The resulting antiproton flux of CAPRICE. The solid lines are the maximum and minimum* $\overline{\mathrm{p}}$ *fluxes calculated by Gaisser and Schaefer [24].*

important difference is that in CAPRICE there is the possibility to select, from the flight data, with independent detectors, samples to check the contamination in the selection. The two experiments result in the same ratio within the errors. Both favour a pure secondary production of the antiprotons but based on these measurements, exotic sources cannot be ruled out.

If the BESS experiment is included, the argument for only secondary produced antiprotons becomes stronger. The measurements by BESS (the '93 flight) is the first clear identifications of antiprotons done below 0.5 GeV (lower than both IMAX and CAPRICE) with a magnet spectrometer. The BESS spectrometer consists of the large super conducting selonoid, with a geometry factor of 1 sr m^2. It has an ingenious trigger system to reject the large background of protons and alpha particles. The trigger system makes a charge selection on-line to decide if a particular event should be saved on tape or not. Since the flight in 1993, the particle identification capabilities has increased and more flight have been performed but the results are not yet published. The resulting ratio from BESS is in strong contradiction to the Buffington et al. measurement.

For the energies above 4 GeV the situation has still not settled. The reported ratio by MASS91 is significantly lower than the Golden measurement in 1979. (In this figure, the Golden points are combined into one energy bin.) These two measurements differ by about three standard deviations. They are in principle done with the same spectrometer, although the detector system was considerably improved for the MASS91 flight. Compared to the version that flew in 1979, the MASS91 instrument provides better reliability and rejection factor. The higher rejection factor against, for example, hard scattered protons might explain why MASS91 report a lower ratio. With the MASS91 measurement, the argument for a pure secondary production of antiprotons has gained strength. However, further measurements, especially at higher energies, are needed and new experiments are in progress.

11.7 Conclusion and Future Experiments

The CAPRICE antiproton flux measured between 0.62 and 3.19 GeV is consistent with a pure secondary production. There is no compelling evidence for the existence of exotic sources of antiprotons in this energy range. Together with IMAX and BESS, the secondary origin hypothesis becomes stronger, but, again, others sources of antiprotons are not completely ruled out.

Later this year , the CAPRICE97 flight is scheduled. CAPRICE97 is a continuation of CAPRICE and two major changes are made to the payload. First, the MWPCs are replaced with a third drift chamber. This will increase the maximum detectable rigidity from 170 to 250 GV/c. Second, the NaF-RICH is replaced by a gas-RICH detector. The gas-RICH is a modified version of the NaF-RICH with the

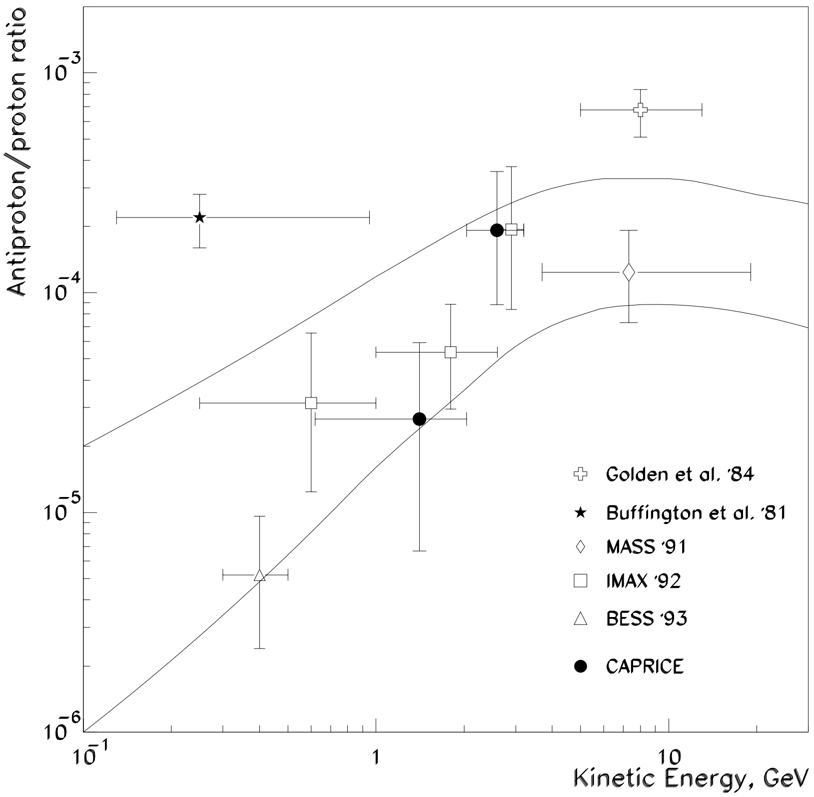

Figure 11.4: *The resulting antiproton to proton ratio. The data in the figure are given by: Golden (open cross) [18], MASS91 (open diamond) [59], IMAX (open squares) [58], BESS (open triangle) [64] and Buffington (filled star) [15]. The curves show a prediction of the antiproton to proton ratio by [24].*

same photosensitive chamber. The NaF radiator is replaced with a C_4F_{10} gas and the Cherenkov light is focused onto the pad plane by a spherical mirror. This will allow identification of antiprotons from 4 to 20 GeV. The lower limit in energy is defined by the cut-off at the launch site (Ft. Sumner) and the upper limit by the flux (for 24 hour flight less than one antiproton is expected above 20 GeV). This will be first time a RICH detector is used for identifying antiprotons in this range.

The PAMELA experiment is a joint project between WiZard and Moscow Engineering Physics Institute. PAMELA is devoted to reach the scientific goal of measuring antiproton and positron spectrum up to more than 100 GeV, and hunting for antinuclei with a sensitivity two orders of magnitude higher than reachable by balloon-borne experiments. The flight is planned for the end of '99 on board of the Russian satellite Resurs-Arktika, build by the VNIIEM institute of Moscow. PAMELA consist of a small permanent magnet; a silicon strip tracking system; an imaging calorimeter; a time-of-flight system and a transition radiation detector.

A competing experiment is the Alpha Magnet Spectrometer (AMS). AMS is planned for a engineering flight on a space shuttle in '98 and the real observation will take place on the International Space Station Alpha, starting year 2001. The main scientific objective is to look for antinuclei with large sensitivity. The particle identification capabilities are yet not defined and at present date it is not clear what kind of observation AMS will be able to do on antiprotons and positrons.

Chapter 12

The Proton Flux

The measurement of the proton flux is important both as a cosmic ray abundance measurement and as a check of the validity of the analysis procedure. The analysis is cross-checked through a comparison with proton fluxes obtained by other balloon experiment and through different, nearly independent, efficiency estimations and proton selections. An agreement between these results implies that the CAPRICE detector performances are well understood and it is a strong indication for the reliability of the CAPRICE analysis.

12.1 Selection of Protons

The main difference between identifying protons and antiprotons in the cosmic rays is their different abundances: antiprotons are very rare whereas protons are the most common particles. The concern is not the contamination in the sample and the goal is to select protons in as large range of rigidity as possible. Compared to the antiproton selection, which is limited to 1.2-4 GV/c, protons can be identified in a much wider range, in fact the selection is essentially limited only by the tracking system. The protons are selected between 0.4 and 100 GV/c. Below 0.4 GV/c the tracking efficiency becomes too low and the upper limit is given by the maximum detectable rigidity. The rigidity range is split in three intervals: 0.4-1.2 GV/c, 1.2-5.0 GV/c and 5.0-100 GV/c. For each interval, different selection criteria are defined so that the contamination is kept as low as possible, still

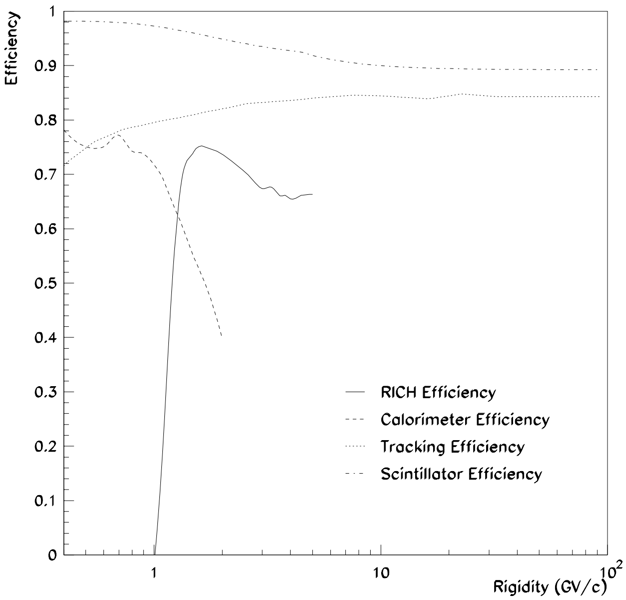

Figure 12.1: *Experimental efficiency of the RICH selection (solid line), of the calorimeter selection (dashed line), of the tracking cuts (dotted line) and of the scintillator dE/dx cuts (dashed-dotted line).*

having as high efficiency as possible.

12.1.1 The tracking system

The basic tracking cuts (see section 9.1.1) are the same as for the antiproton analysis and they are used in the whole rigidity range. Unlike for the antiproton selection, no additional cuts (see section 9.1.2) are put on the data since scattering is not regarded as a problem. The efficiency is the same as obtained in section 10.1. The dotted line in Figure 12.1 shows the tracking efficiency in the range 0.2 to 100 GV/c.

12.1.2 The Time-of-flight system

The time-of-flight system information is used in the same way as for the antiproton selection. The time-of-flight measurement rejects albedo particles, the hit combination of the paddles rejects multiple particle events and the dE/dx scintillator information selects Z=1 particles. The selection criteria (see section 9.3.1) are the same as for the antiproton analysis and used for the full rigidity range.

The main background to protons in the cosmic rays are alpha particles and they are rejected by the dE/dx cut. To check the contamination of this cut, alpha particles are selected with the calorimeter as non interacting particles releasing energy corresponding to charge two in the silicon detectors. To this sample the dE/dx cut is applied and there are nearly no (less than 0.1% survive the cut) Z=2 particles left for all rigidities.

The contamination of muons and deuterons is also determined. It is assumed that muons and positrons behave the same in the scintillators and the contamination for muons is also used for positrons. Muons are selected from a sample of negative deflection events as non interacting particles in the calorimeter. About 30% of the muons survive the proton selection at 1.0 GV/c and the surviving fraction increases with rigidity. Above 2.0 GV/c muons and positrons are more or less indistinguishable from protons in the scintillators.

Deuterons are selected using a combination of time-of-flight and RICH (no detected Cherenkov light). The contamination is found to be lower than the muon contamination due to a larger difference in β, hence giving a larger difference in energy loss in the scintillator. The fraction of muons and deuterons surviving the proton selection are presented in Table 12.1.

The efficiency of the selection criteria is obtained in a similar way as presented in section 10.2 and is fitted by the following relation:

$$\begin{aligned} \alpha &= \beta^{-1.84} \\ \text{Efficiency} &= A\,(1 - B\,e^{-C\cdot\alpha}) \quad R < 5GV/c \qquad (12.1) \\ &= D\,(F\cdot\alpha - 1) \quad R \geq 5GV/c \qquad (12.2) \end{aligned}$$

where R is the rigidity, β is obtained from the rigidity assuming a proton mass and A, B, C, D and F the fitted parameters with

Rigidity GV/c	Surviving fraction (%)	
	Muons	Deuterons
0.4-0.6	5.3 ± 0.9	< 8
0.6-0.8	13.1 ± 1.6	< 1
0.8-1.0	29.5 ± 2.7	< 2
1.0-1.5	52.7 ± 4.6	11.6 ± 1.6

Table 12.1: *Fraction (%) of muons and deuterons that pass the proton dE/dx selection criteria in different rigidity intervals.*

the following values: $A = 0.982 \pm 4 \cdot 10^{-3}$, $B = 73.6 \pm 20.5$, $C = 6.95 \pm 0.27$, $D = 0.221 \pm 4 \cdot 10^{-3}$, $F = 5.04 \pm 0.08$. However the parameters are correlated so the error on the efficiency is obtained using the error matrix. The efficiency is also shown in Figure 12.1 (dashed-dotted line).

In principle, scintillator dE/dx and tracking information are enough to give a reasonable identification power to derive the proton flux. The squares in Figure 12.4 show the proton flux obtained with these selections. However, a non negligible (more than 1%) contamination of deuterons, muons, pions and positrons is still inside the sample resulting in a higher flux than the real proton flux. To decrease this contamination RICH and calorimeter proton selections have been implemented as described in the next sections.

12.1.3 The calorimeter

The calorimeter is used to select protons in a rigidity range where the energetical and topological features of the protons are different from the background. This implies, due to the limited thickness of the calorimeter, an upper limit for the rigidity in the selection with the calorimeter. In fact high energy protons, if they do not interact, appear as minimum ionizing particles in the calorimeter and cannot be separated from other non interacting particles. On the other hand, if they interact, because of not full containment of the hadronic shower a selection against a background of other hadronic interacting particles is extremely difficult. The only clear identification above 100 MV/c is against the positrons.

However, for low rigidities the features of the protons in the calorimeter are quite unique. Below 0.36 GV/c, the protons stop in the plexiglass cover at the top of the calorimeter giving no signal in the silicon detectors while muons, pions and positrons release energy in several strips in the calorimeter. Above this energy, but below 0.7 GV/c, the protons enter the calorimeter but stop inside giving less strips hit than minimum ionizing particles (16 strips) or showering particles.

At higher energies (up to 2.0 GV/c), non minimum ionizing protons can be identified through the energy lost in each silicon strip. Figure 12.2 a) shows the distribution of the mass squared as reconstructed by the calorimeter, for positive particles selected in the rigidity range 0.4 to 2.0 GV/c using the basic tracking and RICH cuts. To reconstruct the mass, events selected as non-interacting proton like particles in the calorimeter are used. Protons selected with the ToF and the dE/dx in the scintillator are used to define upper and lower rigidity dependent limits for the number of hits in the calorimeter. The average energy lost (ΔE) in the calorimeter is defined as the total detected energy in units of mip (see section 7.1.3) divided by the number of hits. The mass squared is calculated from:

$$\left.\begin{array}{rcl} \Delta\mathrm{E} & = & \frac{1}{\beta^2}\,\mathrm{mip} \\ \beta^2 & = & \frac{R^2}{R^2+m^2} \end{array}\right\} m^2 \; = R^2\,(\Delta\mathrm{E}-1) \tag{12.3}$$

For the particles that do not satisfy the condition of non-interacting proton the mass squared is put to zero, and this explains the events at zero in Figure 12.2 a) and b). In Figure 12.2 a) a clear proton signal peaked around 1.0 (GeV/c^2) ^{2} can be noticed. Muons and pions show up with a very low mass squared. The long tail for the high values is due to high energy losses, interacting protons misidentified as non interacting and deuterons.

Selecting deuterons with low contamination (and low efficiency) cuts, based on the ToF, RICH and dE/dx in the scintillators data, the calorimeter identification can be verified. Figure 12.2 b) shows the reconstructed mass squared for these events. Only three events (hatched ones) satisfy the proton condition. The distribution is peaked at 4 (GeV/c^2)^2, compatible with the expected deuteron value because the energy lost used for the mass reconstruction is obtained by an average of the detected energy in several strips. This gives a

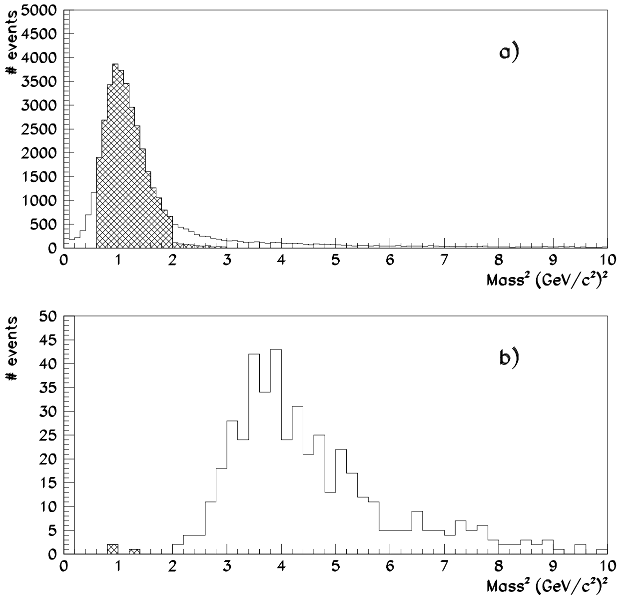

Figure 12.2: *Reconstructed mass squared for: a) positive deflection particles; b) deuterons selected with the ToF, RICH and scintillator dE/dx. The hatched areas show the events selected as protons with a cut based on the mass squared. For the events that do not satisfy the non-interacting condition, the mass square is put to zero. Note that for low energies, a looser cut is used and this explains the small tail in a) for values greater than 2 (GeV/c^2).*

mean value of the energy lost which is higher than the most probable value, which is the definition for mip, resulting in a higher reconstructed mass squared.

As shown in Figure 12.2 a) and b), protons can accurately be separated from deuterons. The hatched areas indicate the events selected as protons using the mass squared. Note that for low energies (when the deuterons do not enter the calorimeter), a looser cut can be used and this explains the small tail in a) for values greater than 2 $(\mathrm{GeV/c^2})^2$.

A calorimeter proton selection based on the mass squared results in a negligible electromagnetic contamination since only non interacting particles are selected. The fraction of muons/pions and deuterons that survive this cut is presented in Table 12.2. The calorimeter proton cuts are used to select sample of protons with low deuteron contamination for the study of the RICH and dE/dx scintillator efficiency up to 3 GV/c. The calorimeter criteria can also be used above 3 GV/c to get a Z=1 sample with a low contamination (less than 0.1%) of alpha particles.

Rigidity GV/c	Surviving fraction (%)	
	Muons	Deuterons
0.4-0.6	1.7 ± 0.4	< 8
0.6-0.8	5.2 ± 1.0	2.3 ± 1.6
0.8-1.0	11.6 ± 1.7	0.5 ± 0.5
1.0-1.2	18.3 ± 2.6	< 0.5
1.2-1.5	36.7 ± 3.6	0.3 ± 0.3
1.5-2.0	51.9 ± 3.6	< 0.2
2.0-3.0	47.9 ± 3.6	4.3 ± 1.3

Table 12.2: *Fraction (%) of muons and deuterons that pass the proton selection criteria of the calorimeter.*

Figure 12.1 shows the efficiency of the calorimeter criteria (dashed line) in the range 0.4-2.0 GV/c. Comparing this efficiency with the RICH selection efficiency (solid line), it is found that the calorimeter selection efficiency becomes lower than the RICH selection efficiency above 1.2 GV/c. Since the muon/pion rejection of the RICH is higher than of the calorimeter, it is preferred to use the calorimeter selection up to 1.2 GV/c and the RICH selection above this rigidity.

12.1.4 The RICH

The RICH selection is applied to the data in a different way for protons than for antiprotons. In principle the same cuts are used but they are combined to achieve a higher efficiency. For the whole rigidity range, from 0.4 to 100 GV/c, the basic cuts (see section 9.5.1) on the RICH are applied. In this way double particle events are rejected with the pile-up cut and scattered events are rejected with the cut on difference in impact position. In a limited rigidity range, 1.2-5.0 GV/c, the RICH is also used to identify protons. The identification is based on the same criteria (see section 9.5.2) as for the antiproton selection with two exceptions:

1. as discussed in section 9.5.3, two n_{eff} cuts are used: n_{eff} >3 for the RICH central region and n_{eff} >8 for the RICH border region;

2. the 30 mrad cut is not applied.

The choice of the rigidity range in which these criteria are used is based on a compromise between efficiency and contamination.

As already discussed in Chapter 10, the proton detection efficiency of the RICH is low at the threshold for protons to produce Cherenkov light because part of the selection criteria is a requirement of the number of pads used for the Cherenkov angle calculation. The number of photons is increasing with rigidity and hence the number of pads avaliable for the Cherenkov angle calculation is also increasing. As a consequence, the efficiency is close to 0% at 1.0 GV/c and increasing up to 75% at 1.5 GV/c. Figure 12.1 (solid line) shows the proton selection efficiency in the rigidity range 1 to 5 GV/c. Between 1.5 GV/c and 2.8 GV/c the efficiency is similar to the one of the antiproton selection (see Figure 10.6), whereas below 1.5 GV/c the lower cut on n_{eff} for the central region results in a higher efficiency for the proton selection.

At 1.2 GV/c, the efficiency becomes higher than 50% while other selection criteria based on calorimeter or scintillator dE/dx information above this energy are not anymore effective against the muon/pion background. The background is estimated to a few per mille of the proton flux. Above 5 GV/c, the Cherenkov angle distribution for deuterons starts to overlap with the proton one and there is no meaning in applying RICH cuts that would decrease the selection efficiency for protons without decreasing the background.

The muon/pion and positron contamination after the RICH proton selection is comparable to what is given in the antiproton chapter for rigidities between 1.2 and 2.8 GV/c. Above this rigidity the muon and positron contamination increase because of overlapping Cherenkov angle distributions. The 30 mrad cut was introduced in the antiproton selection to limit this contamination but for protons the decrease in efficiency would not be compensated by the gain in rejection.

The deuteron contamination is also low, less than 0.1%, in this rigidity bin because protons and deuterons are well separated by the Cherenkov angle. The actual contamination is hard to estimate because it is not possible to select clean sample of deuterons with any other detector.

The efficiency of the RICH criteria is estimated using a proton sample selected with scintillator dE/dx cuts in the whole rigidity range, calorimeter proton selection below 3 GV/c, and RICH evaluation of the deuteron contamination between 3 and 5 GV/c. The RICH efficiency is given by an interpolation of the experimental values between 1.2 and 5 GV/c (Figure 12.1) and by a fit to the measured efficiencies below 1.2 and above 5 GV/c:

$$\text{Efficiency} = A\,(1 - B\,e^{-C\cdot R}) \qquad (12.4)$$

where R is the rigidity in GV/c and A, B, C, D and E the fitted parameters with the following values: $A = 0.869 \pm 8 \cdot 10^{-4}$, $B = 1.55 \pm 0.13$, $C = 4.24 \pm 0.12$. Also in this case to take care of the correlation between the parameters the error on the efficiency is obtained using the error matrix.

12.2 Resulting Proton Flux

In summary, the selection of protons is made in three rigidity intervals: 0.4-1.2 GV/c, 1.2-5.0 GV/c and >5 GV/c. In all three intervals, the same cuts are used on the tracking, scintillator and RICH (only basic cuts) data to select single charged tracks. The calorimeter is only used in the first interval for the selection and the RICH proton selection is only used in the second interval. In this way, the efficiency of the selection is maximized at the same time as the contamination is as low as possible.

The proton flux is determined in a similar way as done for the antiproton flux in Chapter 11. To properly treat the rigidity dependence of the efficiencies, the rigidity range 0.4-4 GV/c has been split in bins of 50 MV/c width. Above 4 GV/c, bins of increasing[1] width are used up to 100 GV/c. For each bin, the number of protons has been counted and normalized with the detector efficiencies.

It is assumed that all protons interacting above the tracking system are rejected by the cuts and the proton sample is corrected for these losses with multiplicative factors as shown in Chapter 11. To extrapolate the number of protons to the top of the payload, the observed number of protons at the spectrometer is divided by the detector efficiencies and multiplied with these factors. From these numbers the atmospheric secondary protons is subtracted. Protons losses in the atmosphere are corrected for by multiplicative factors, as shown in section 11.5.3.

For the corrections of secondary atmospheric protons, the calculation made by Papini et al. [63] is chosen (described in Chapter 11). It is worth noticing that these calculations are obtained with the primary proton fluxes given in the same paper, hereinafter called the "Papini flux". To properly use these secondary calculations, it is necessary to scale the atmospheric secondary fluxes to the atmospheric depth and to the solar modulation during the CAPRICE flight. Both scalings are done by interpolating the theoretical data with a simple power law function. While this is easily done using the data at 3 and 5 g/cm^2 and interpolating to 3.9 g/cm^2, it is more complicated for the solar modulation.

The expression for the proton flux in [63] is a compilation of experimental measurements performed close to solar minimum and maximum activity but, yet, with different solar modulations. Therefore, it is necessary to find the correct solar modulation parameters (Φ) for the atmospheric secondaries at solar minimum and maximum. Only after having found these parameters, the theoretical calculations can be interpolated to the CAPRICE flight. Furthermore, it is necessary to use a primary proton flux for the theoretical

---

[1] An exponential increase has been chosen.

atmospheric calculation as similar as possible to the CAPRICE experimental proton flux. This means that is important to find a normalization factor between the primary CAPRICE proton flux and the Papini flux. This is done using an iterative procedure. The atmospheric protons are obtained using the secondary flux calculated in [63] for solar minimum at a residual atmosphere of 3.9 g/cm^2, normalized to the geometrical factor (G) and live time (T$_{live}$) of the experiment. Then the resulting numbers of proton are corrected for losses in the atmosphere due to interactions giving the number of protons (N_p^{TOA}) at the top of the atmosphere (TOA).

The proton flux is, consequently, given by

$$\mathrm{Flux(E)} = \frac{1}{T_{live} \times G \times \Delta E} \times N_p^{TOA}(E) \tag{12.5}$$

where ΔE are the energy bins corrected to the top of the atmosphere and E the kinetic energy.

The proton flux is then compared with the Papini flux in an energy region where the solar modulation has no effect (above 20 GeV). From this comparison, a normalization factor is found. Thus the calculated secondaries are multiplied by this factor and subtracted from the flux at the top of the payload. This flux is then propagated to the top of the atmosphere. Here the resulting flux is compared once more with the Papini flux. This is done until the normalization factor does not change more than 1% from one iteration to the other. This factor is found to be 0.77.

Next, the Papini flux is compared with the experimental proton flux at energies below 10 GeV. Here the solar modulation has a large effect and has to be taken into account. The solar modulation parameter Φ=500 MV of the CAPRICE flight and the experimental proton flux are used as inputs of a fitting procedure where the fitting functions are the two modulated Papini fluxes (solar minimum and maximum). The parameters to be fitted are the solar modulation parameters Φ_{min} and Φ_{max} of the Papini fluxes.

The last step is to interpolate the secondary protons to the CAPRICE modulation and subtract them from the payload protons. The flux at the TOA is once more obtained and compared with Papini fluxes resulting in new values for Φ. Also this iterative procedure stops when Φ does not change more than 1% from one iteration to the other. The result for Papini modulations are Φ_{min}= 450 MeV and Φ_{max}=990 MV for solar minimum and maximum activity, respectively.

In conclusion, the theoretical atmospheric secondary protons [63] and antiprotons [65] used in this work are interpolated to an atmospheric depth of 3.9 g/cm^2, solar modulated with a Φ=500 MV and multiplied by a factor 0.77.

The dots in Figure 12.3 show the resulting proton flux (CAPRICE proton flux) at the top of the atmosphere. The solid line is the Papini proton flux modulated with Φ=500 MV and multiplied by a factor 0.77. The dotted line is the resulting theoretical atmospheric secondary proton flux. Note that the secondary atmospheric flux is small compared to the primary flux for kinetic energies above a few hundred MeV. The CAPRICE proton flux is fitted be the following parameterization:

$$\mathrm{Flux(E)} \;=\; A\,E^{-\gamma}\;(protons/m^2\,sr\,s\,GeV) \qquad (12.6)$$

where E is the kinetic energy in GeV. A power law fit between 20 and 100 GeV results in a spectral index (γ) of 2.70 ± 0.07 and the constant A is found to be $(1.01 \pm 0.13)\cdot 10^4$, including both statistical and systematic uncertainties. The CAPRICE proton flux is also given in Table 12.3.

Notice that above 2 GeV, a muon/pion contamination of few per mille is present. Above 5 GeV/n there is an unknown deuteron contamination[2], but probably of the order of 1%.

12.3 Evaluation of the Proton Flux

In this section, the CAPRICE proton flux is compared it with two alternative selections and with other experimental results.

Figure 12.4 shows the CAPRICE proton flux (●) and the proton flux (□) resulting from a selection based only on scintillator dE/dx and tracking information in the energy range: a) 0.1-4.0 GeV and b) 4.0-100 GeV. In figure a) it is shown that the final flux is few

---

[2] No experimental results of deuteron to proton ratio are available for energies above 3 GeV/n [62].

Kinetic energy (GeV)		Proton Flux (particles/(m^2 sr s GeV))
0.15 - 0.18	0.17	$(1.05 \pm 0.09) \cdot 10^3$
0.18 - 0.23	0.21	$(1.22 \pm 0.06) \cdot 10^3$
0.23 - 0.28	0.26	$(1.32 \pm 0.05) \cdot 10^3$
0.28 - 0.34	0.31	$(1.39 \pm 0.04) \cdot 10^3$
0.34 - 0.40	0.37	$(1.39 \pm 0.03) \cdot 10^3$
0.40 - 0.47	0.44	$(1.38 \pm 0.03) \cdot 10^3$
0.47 - 0.54	0.51	$(1.34 \pm 0.03) \cdot 10^3$
0.54 - 0.62	0.58	$(1.29 \pm 0.03) \cdot 10^3$
0.62 - 0.70	0.66	$(1.21 \pm 0.03) \cdot 10^3$
0.70 - 0.78	0.74	$(1.12 \pm 0.03) \cdot 10^3$
0.78 - 0.86	0.82	$(1.09 \pm 0.03) \cdot 10^3$
0.86 - 1.30	1.07	$(8.60 \pm 0.18) \cdot 10^2$
1.3 - 1.8	1.5	$(5.95 \pm 0.14) \cdot 10^2$
1.8 - 2.2	2.0	$(4.18 \pm 0.12) \cdot 10^2$
2.2 - 2.7	2.5	$(3.08 \pm 0.07) \cdot 10^2$
2.7 - 3.2	2.9	$(2.29 \pm 0.06) \cdot 10^2$
3.2 - 4.2	3.6	$(1.51 \pm 0.04) \cdot 10^2$
4.2 - 5.5	4.8	$(9.68 \pm 0.18) \cdot 10^1$
5.5 - 7.1	6.2	$(5.55 \pm 0.10) \cdot 10^1$
7.1 - 9.2	8.1	$(3.13 \pm 0.06) \cdot 10^1$
9.2 - 11.8	10.3	$(1.71 \pm 0.04) \cdot 10^1$
11.8 - 15.0	13.2	9.37 ± 0.21
15.0 - 19.1	16.8	4.96 ± 0.12
19.1 - 24.2	21.4	2.67 ± 0.07
24.2 - 30.7	27.1	1.26 ± 0.04
30.7 - 38.9	34.4	$(7.59 \pm 0.27) \cdot 10^{-1}$
38.9 - 49.1	43.5	$(4.22 \pm 0.17) \cdot 10^{-1}$
49.1 - 62.0	54.9	$(2.14 \pm 0.11) \cdot 10^{-1}$
62.0 - 78.2	69.3	$(1.01 \pm 0.06) \cdot 10^{-1}$
78.2 - 99.1	87.5	$(5.57 \pm 0.42) \cdot 10^{-2}$

Table 12.3: *The CAPRICE experimental proton flux at the top of the atmosphere.*

per cent lower than the other flux below 4 GeV. This is due to a contamination from muons/pions and positrons below 1 GeV and deuterons mainly between 0.5 and 4 GeV. Above 5 GeV (figure b)) the two fluxes coincide. Here, the only difference are the basic cuts on the RICH, and the good agreement between the fluxes imply that the efficiency for the RICH cuts is properly treated at high energies.

This test results in a good check of the RICH and calorimeter selection efficiencies that, partially, validates also the work on the antiproton analysis. In fact the proton flux, obtained in the rigidity region 1.2-4.0 GV/c in the analysis for the antiproton to proton ratio agree with this final proton flux.

To also check the standard tracking selection, the tracking system has been separated into its two components: MWPC and drift chambers (DC). The events have been fitted using only the drift chamber system using the following cuts:

- the fit routine must converge;
- the number of points in the fit: $x_{hit} \geq 9$; $y_{hit} \geq 5$;
- the goodness of the fit: $\chi^2_x \leq 8$; $\chi^2_y \leq 8$;
- the uncertainty in the deflection: $\sigma_\eta \leq 0.04$.

Full containment of the track inside the drift chambers is also required. At the top and bottom of the tracking system, the fitted track has to be 4 cm away from the borders of the chambers. Protons are selected in the range 0.4-100 GV/c with the same cuts on the scintillator dE/dx, RICH and calorimeter described in the previous section plus these conditions on the DC system. The detector efficiencies are the same as previously described except for the drift chamber tracking cuts. The drift chamber efficiency has been obtained in a similar way to what is described in section 10.1.7. Single charged tracks have been selected requiring that the fit routine converges when using only the MWPC data. In this way the rigidity of the particles is obtained. Then, out of the single charged track sample, a proton sample is selected matching the top and bottom dE/dx of the ToF scintillators. This sample is used to get the efficiencies of the DC cuts in the rigidity range 0.2-100 GV/c. Because of the containment condition in the drift chambers a new geometrical factor, smaller by ~ 6%, has been calculated and used. The proton flux at the top of the atmosphere has been calculated as described in the previous section.

Figure 12.5 shows the final CAPRICE proton flux (•) and the proton flux (□) obtained as just described. A good agreement is obtained at all energies. The possible difference at high energies could be due to a small decrease in the tracking efficiency at high energies. However, the complete system is more reliable, it has a higher lever arm for small deflections, and so it is assumed that the difference is due to fluctuation of the DC system.

Once more, this is a strong indication, even if the two selections are not completely independent, that the tracking efficiencies and acceptance are properly estimated both in the proton and antiproton selections.

Figure 12.6 shows the CAPRICE proton flux (•) together with the proton fluxes measured by the LEAP [74] (⋆) and in the IMAX [77] (□) balloon-borne experiments. There is a good agreement between the three fluxes for high energies where there is no solar modulation effect. In Table 12.4 the results of a power law fit between 20 and 100 GeV (see equation 12.6) for the three fluxes are presented. The IMAX experiment used the same tracking detectors as CAPRICE. Its proton flux has a lower spectral index than CAPRICE, though inside one standard deviation.

Experiment	Constant A $(protons/m^2\ sr\ s\ GeV)$	Spectral index γ
CAPRICE	$(1.01 \pm 0.13)\cdot 10^4$	2.70 ± 0.07
IMAX	$(8.2 \pm 1.6)\cdot 10^3$	2.6 ± 0.1
LEAP	$(8.7 \pm 0.8)\cdot 10^3$	2.64 ± 0.04

Table 12.4: *Results of a power law fit between 20 and 100 GeV of three balloon flights.*

At low energies, the IMAX flux is lower because of a higher solar modulation. It is more difficult to explain why the LEAP flux is higher than the CAPRICE flux since the solar modulation for the two flights should be the same[3]. If the IMAX flux is modulated to the CAPRICE and LEAP solar modulation the resulting flux is in good agreement with CAPRICE. This check and the initial considerations of this section indicate that the LEAP flux might be overestimated for energies below 5 GeV.

---

[3] LEAP flew in august 1987 and CAPRICE in august 1994 but the CLIMAX neutron monitor counts are similar.

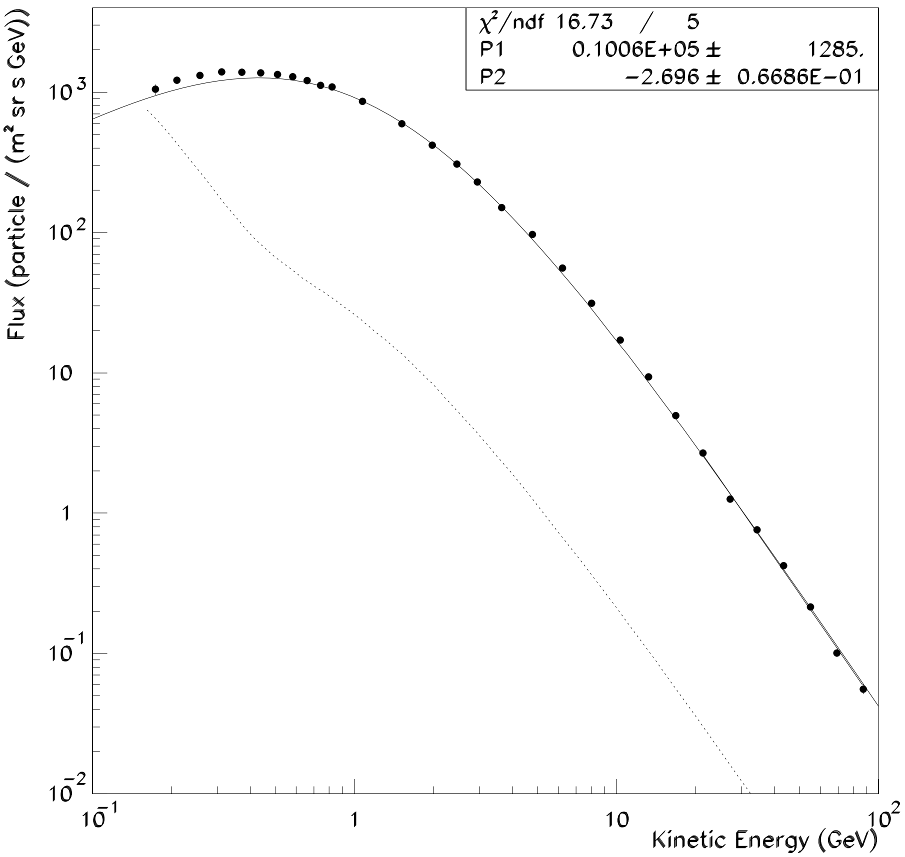

Figure 12.3: *CAPRICE experimental proton flux together with theoretical atmospheric proton flux (dotted line) for this experiment and input proton flux (solid line) for the secondary calculation. Note that the secondary atmospheric flux is small compared to the primary flux for kinetic energies above a few hundred MeV. The experimental data is fitted by a power law function between 20 and 100 GeV.*

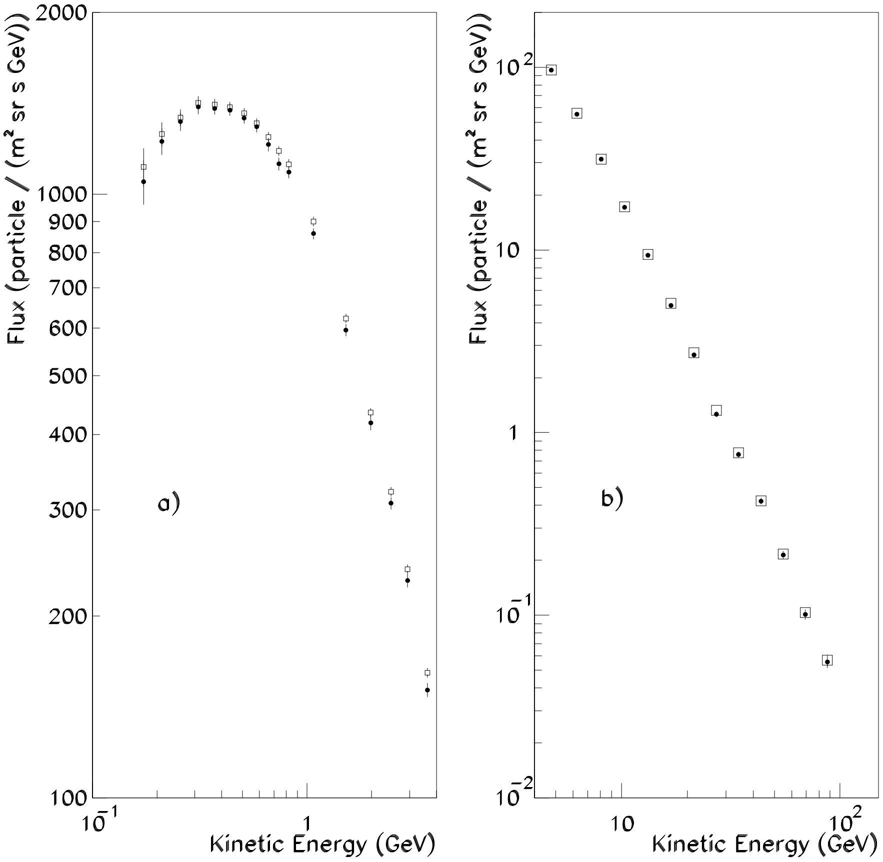

Figure 12.4: *CAPRICE experimental proton flux with (●) complete selection and with (□) only scintillator dE/dx and tracking cuts in: a) 0.1-4.0 GeV; b) 4.0-100 GeV.*

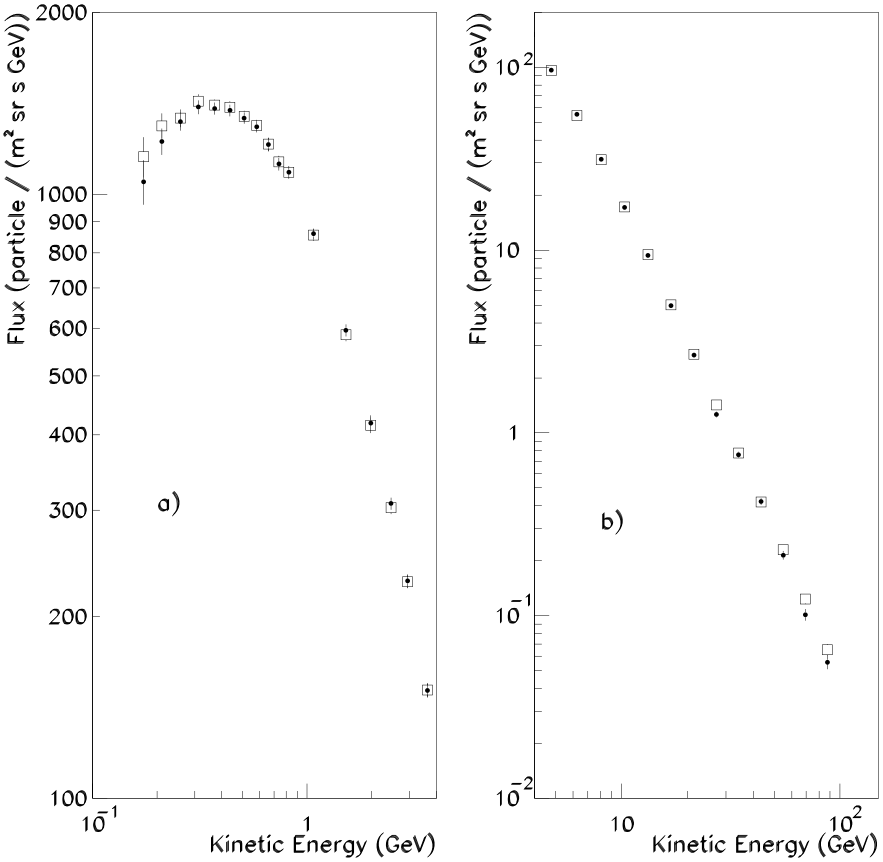

Figure 12.5: *CAPRICE experimental proton flux with tracking selection performed with (●) the complete tracking system and with (□) only the drift chamber system in: a) 0.1-4.0 GeV; b) 4.0-100 GeV.*

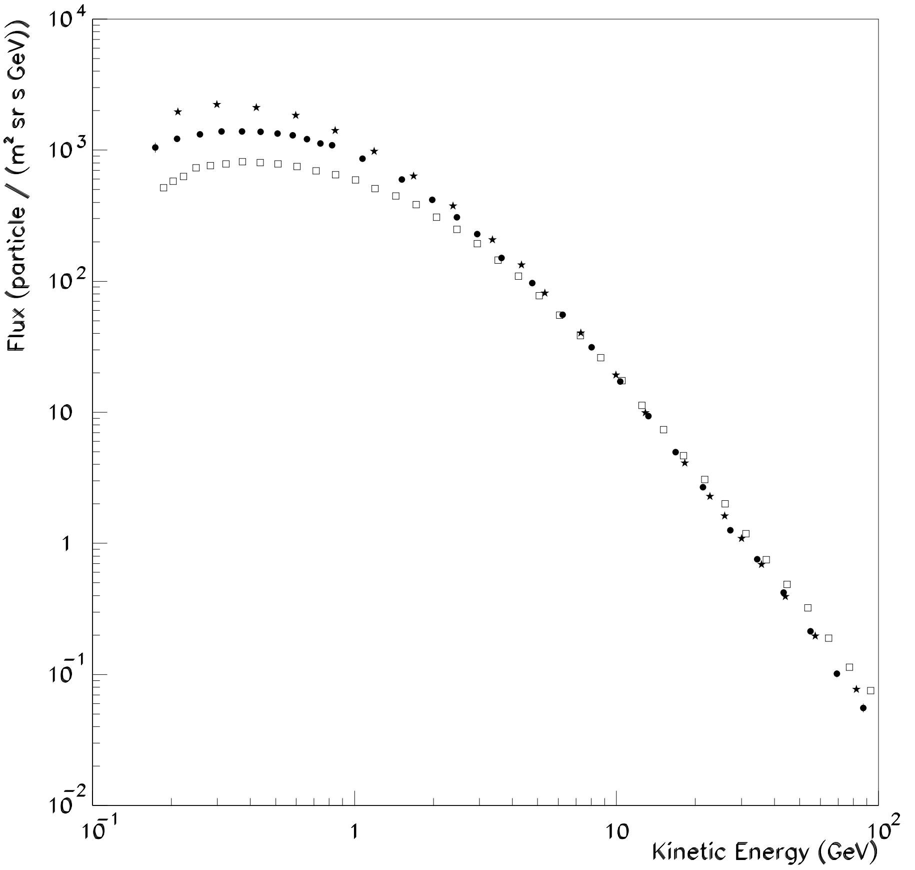

Figure 12.6: *Proton flux: (●) CAPRICE, (⋆) LEAP, (□) IMAX balloon-borne experiments.*

Acknowledgements

Bibliography

[1] Y. Sekido & H. Elliot (Editors), "Early History of Cosmic Ray Studies", D. Reidel publishing company (1985).

[2] T. K. Gaisser, "Cosmic Rays and Particle Physics", Cambridge University Press (1992).

[3] E. Fermi, Phys. Rev. **75** (1949) 1169.

[4] S. Rudaz & F. W. Stecker, Astrophys. Journ. **325** (1988) 16.

[5] P. Kiraly, Nature **293** (1981) 120.

[6] O. Chamberlain et al., Phys. Rev. **100** (1955) 947.

[7] M. I. Fradkin, Sovjet Phys. JETP **2** (1956) 87.

[8] R. L. Golden, et al., Phys. Rev. Lett. **43** (1979) 1196.

[9] E. A. Bogomolov et al., Proc. 16th Int. Cosmic Ray Conf., Kyoto **1** (1979) 330.

[10] C. J. Cesarsky, Ann. Rev. Astron. & Astrophys. **18** (1980) 289.

[11] R. Cowsik & L. Wilson, Proc. 13th Int. Cosmic Ray Conf., Denver **1**, (1973) 500.

[12] P. Peters & N. J. Westergaard, Astrophys. Sp. Sci. **48** (1977) 21.

[13] R. J. Protheroe, Astrophys. Journ. **251** (1981) 387.

[14] S. A. Stephens, Nature **289** (1981) 267.

[15] A. Buffington et al. Astrophys. Journ. **248** (1981) 1179.

[16] M. H. Salamon et al., Astrophys. Journ. **349** (1990) 78.

[17] S. J. Stochaj, "Measurement of Low Energy Antiprotons in the Cosmic Radiation", PhD Thesis, University of Marland (1990).

[18] R. L. Golden et al., Astrophys. Lett. **24** (1984) 75

[19] E. A. Bogomolov et al., Proc. of 10th Int. Cosmic Ray Conf., Moscow **2** (1987) 72.
E. A. Bogomolov et al., Proc. of 11th Int. Cosmic Ray Conf., Adelaide **3** (1990) 288.

[20] W. R. Webber & M. S. Potgieter, Astrophys. Journ. **344** (1989) 779.

[21] A. W. Labrador & R. A. Mewaldt, Proc. 24th Int. Cosmic Ray Conf., Rome **2** (1995) 68.

[22] T. Mitsui et al., "Expected Enhancement of the Primary Antiproton Flux at the Solar Minimum", **UT-ICEPP 96-03** (1996) 22.

[23] S. W. Hawking, Nature **248** (1974) 30.

[24] T. K. Gaisser & R. K. Schaeffer, Astrophys. Journ. **394** (1992) 174.

[25] V. L. Ginzburg et al., "Astrophysics of Cosmic Rays", North-Holland Elsevier (1990).

[26] U. Heinbach & M. Simon, Astrophys. Journ. **441** (1995) 209.

[27] R. L. Golden et al., (the WiZard collaboration) Il Nuovo Cimento **105** (1990) 191.

[28] T. Francke, "A Ring Imaging Cherenkov Counter using a Solid Radiator", PhD Thesis, KTH Stockholm (1991).

[29] P. Carlson et al., Nucl. Instr. and Meth. A **349** (1994) 577.

[30] G. Barbiellini et al. (the WiZard/CAPRICE collaboration), Proc. 24th Int. Cosmic Ray Conf., Rome **3** (1995) 657.

[31] G. Barbiellini et al. (the WiZard/CAPRICE collaboration) Nucl. Instr. and Meth. A **371** (1996) 169.

[32] G. Barbiellini et al. (the WiZard/CAPRICE collaboration), Astron. Astrophys. **309** (1996) L15.

[33] R. L. Golden et al.,"User's guide to the NASA/NMSU Balloon Borne Magnet Facility", NMSU internal report (1990).

[34] R. L. Golden et al., Nucl. Instr. and Meth. **148** (1978) 179.

[35] M. Hof et al. (the IMAX collaboration), Nucl. Instr. and Meth. A **345** (1994) 561.

[36] R. L. Golden et al., Nucl. Instr. and Meth. A **306** (1991) 366.

[37] LeCroy Research Systems, Chestnut Ridge, USA.

[38] M. Bocciolini et al., Nucl. Instr. and Meth. A **370** (1996) 403.

[39] F. Aversa et al., Nucl. Instr. and Meth. A **360** (1995) 17.

[40] I. M. Frank & I. J. Tamm, Dokl. Academie des Sciences de l'URSS **14** (1937) 109.

[41] A. W. Labrador et al. (the IMAX collaboration), Proc. 23th Int. Cosmic Ray Conf., Calgary, **2** (1993) 524.

[42] J. Séguinot & T. Ypsilantis, Nucl. Instr. and Meth. **142** (1977) 377.

[43] W. Adam et al. (the Delph RICH collaboration), Nucl. Instr. and Meth. A **343** (1994) 68.

[44] J. Buckley et al., Nucl. Instr. and Meth. A **323** (1992) 380.

[45] M. Hempstead et al., Nucl. Instr. and Meth. A **306** (1991) 207.

[46] http://plains.uwyo.edu/ metal/invar.html.

[47] D. F. Anderson, Phys. Lett. B **118** (1980) 230.

[48] Analog Devices, Norwood, USA.

[49] National Semiconducters, USA.

[50] E. de Beuville et al., Nucl. Instr. and Meth. A **288** (1990) 157.

[51] E. Chesi et al., CERN PS202 Internal Note (1988).

[52] A. Tornes & N. Weber, “A Data Acquisition System for the CAPRICE Solid Radiator RICH Detector”, Diploma Thesis, LiTH Linköping (1992).

[53] Particle Properties Data Booklet (1996).

[54] L. Landau, J. Phys. (USSR) **8** (1944) 201.

[55] C. W. Fabjan, “Calorimetry in high-energy physics” CERN-EP **54** (1985).

[56] A. Johansson, “Reconstructing Cherenkov Angles in CAPRICE”, Diploma Thesis, Umeå University (1994).

[57] T. Ullrich et al., Nucl. Instr. and Meth. A **371** (1996) 243.

[58] J. W. Mitchell et al. (the IMAX collaboration), Phys. Rev. Lett. **76** (1996) 3057.

[59] M. Hof et al. (the WiZard/MASS collaboration), Astrophys. Journ. **467** (1996) L33.

[60] GEANT Program Library, CERN, Brun et al. (1994).

[61] M. Bocciolini et al., Nucl. Instr. and Meth. A **333** (1993) 560.

[62] O. Reimer et al. (the IMAX collaboration), Proc. 24th Int. Cosmic Ray Conf., Rome **2** (1995) 614.

[63] P. Papini et al., Il Nuovo Cimento **19** (1996) 367.

[64] A. Moiseev et al. (the BESS collaboration) Astrophys. Journ. **474** (1997) 479.

[65] S. A. Stephens, submitted to Astropart. Phys. (1996).

[66] S. A. Stephens, Proc. 17th Int. Cosmic Ray Conf., Paris **4** (1981) 282.

[67] M. Zeilik, “Astronomy, the evolving universe”, John Wiley & Sons, Inc. (1991).

[68] L. J. Gleeson & W. I. Axford, Astrophys. Journ. **154** (1968) 1011.

[69] http://astro.uchicago.edu/home/web/pyle/neutron.html

[70] P. Paradis, “Solar Modulation of Hydrogen and Helium Cosmic Ray Nuclei above 400 Mev/nucleon, from 1976 to 1993”, PhD Thesis, New Mexico State University (1995).

[71] file://odysseus.uchicago.edu/NeutronMonitor/
Data courtesy University of Chicago, supported by “National Science Foundation Grant ATM-9420790”.

[72] J. D. Sullivan, Nucl. Instr. and Meth. **95** (1971) 5.

[73] W. R. Webber et al., Proc. 20th Int. Cosmic Ray Conf., Moscow **1** (1987) 325.

[74] E. S. Seo et al., Nucl. Tracks. Radiat. Meas. **20** (1992) 431.

[75] J. J. Engelman et al., Astron. Astrophys. **223** (1990) 96.

[76] L. C. Tan & L. K. Ng, J. Phys. G **9** (1983) 227.

[77] W. Menn, private communication.

Papers to which the author of this thesis is either author or co-author are: [29, 30, 31, 32] and [52]. The following works by this author are not included in this thesis:

P. Carlson, T. Francke, M. Suffert and N. Weber
“A RICH Counter for Identifying Antiprotons and Light Isotopes in the Cosmic Radiation”
Nucl. Instr. and Meth. A **343** (1994) 198

P. Carlson, T. Francke, M. Suffert and N. Weber
"A RICH Counter for Antimatter and Isotope Identification in the Cosmic Radiation"
Proc. 23th Int. Cosmic Ray Conf., Calgary, **2** (1993) 504.

P. Carlson, T. Francke, M. Suffert and N. Weber
"A RICH Counter for Antimatter and Isotope Identification in the Cosmic Radiation"
IEEE Transaction on Nuclear Science, 41 (1994) 1321.

P. Carlson, T. Francke, M. Suffert and N. Weber
"CAPRICE"
Nouvelles de Saturne 1993-1994, Lab nat. Saturne, Paris, France, Juillet 1994.

"$\overline{p}$ and e^+ Identification Capabilities of CAPRICE"
G. Barbiellini et al. (the WiZard/CAPRICE collaboration), Proc. 24th Int. Cosmic Ray Conf., Rome **3** (1995) 80.

"The WiZard/CAPRICE Silicon-tungsten Calorimeter"
G. Barbiellini et al. (the WiZard/CAPRICE collaboration), Proc. 24th Int. Cosmic Ray Conf., Rome **3** (1995) 661.

"The Magnet Spectrometer PAMELA for the Study of Cosmic Antimatter in Space"
G. Barbiellini et al. (the WiZard/CAPRICE collaboration), Proc. 24th Int. Cosmic Ray Conf., Rome **3** (1995) 591.

P. Carlson, T. Francke, M. Suffert and N. Weber
"Long Narrow CsI(Tl) Rods as Calorimeter Elements"
Nucl. Instr. and Meth. A **376** (1996) 271.

List of Figures

List of Tables